

Rational Design and Development of Purely Peptidic Amphiphiles for Gene Delivery

Inauguraldissertation

Zur

Erlangung der Würde eines Doktors der Philosophie

Vorgelegt der

Philosophisch-Naturwissenschaftlichen Fakultät

der Universität Basel

von

Shabnam Tarvirdipour

Basel, 2022

Originaldokument gespeichert auf dem Dokumentenserver der Universität Basel

edoc.unibas.ch



This work is licensed under a [Creative Commons Attribution-NonCommercial-ShareAlike 3.0 Unported License](https://creativecommons.org/licenses/by-nc-sa/3.0/).

Genehmigt von der Philosophisch-Naturwissenschaftlichen Fakultät

auf Antrag von

Prof. Dr. Cornelia G. Palivan (Universität Basel)

Prof. Dr. Yaakov (Kobi) Benenson (Eidgenössische Technische Hochschule Zürich)

Prof. Dr. Wolfgang Meier (Universität Basel)

Prof. Dr. Sandrine Gerber (École Polytechnique Fédérale de Lausanne)

Basel, 22.06.2021.

Prof. Dr. Marcel Mayor

Dekan

Summary

Gene therapy depends on viral and non-viral delivery systems to ferry nucleic acids into target cells^{1,2}. In recent years, gene insertion and interference therapies have made a ground breaking impact in the treatment of rare inherited diseases, neurological disorders, cardiac diseases, and cancer³. Several disadvantages associated with viral vectors, such as high toxicity and immunogenicity, limitation in size of transgenic DNA, and high manufacturing cost have triggered the rapid expansion of non-viral delivery systems including peptide-based vectors⁴. The advantages of peptides are not only their biocompatibility and biodegradability, but sheer limitless possible combinations and modifications of amino acid residues that are able to promote the assembly of modular, multiplexed delivery systems⁵. With the advantages of peptides in mind, we looked into the potential of peptide-based nanoassemblies in developing a non-viral gene delivery system. The thesis is structured to successively address (i) the design and development of purely amphiphilic peptides self-assembling into multicompartment micelles (MCMs), (ii) the efficient DNA cargo entrapment up to 100 nucleotides in length into self-assembled peptide MCMs and the delivery thereof, and (iii) targeting of oligonucleotides to the nucleus via a nuclear localization signal (NLS) integrated in the peptide-based carrier. The challenge was to rationally design the peptides and identify the proper conditions in which the DNA entrapment does not interfere with multicompartment micellar self-assembly. In addition, to fulfil the prerequisites of a successful gene delivery system that overcomes cellular barriers, we incorporated biologically active amino acids in our peptide sequences. A systematic characterization of the physicochemical features of the peptidic nanostructures was carried out to gain insight into the mechanism underlying self-assembly and to shed light on ways to tune these features for prospective biomedical applications. Taking into account our findings on how the size/type of genetic payload together with the peptide amphiphile's charge and length impact the self-assembly process, we successfully established a non-toxic, purely peptidic delivery system that serves as a cornerstone for developing oligonucleotide therapy platforms.

Table of Contents

List of Figures	iii
List of Tables	vii
Abbreviations.....	i
1 Introduction.....	4
1.1 Principle of Amphiphile Self-Assembly.....	4
1.1.1 Self-assembly of Amphiphilic Peptides.....	5
1.1.2 Gramicidin	6
1.2 Peptide-based Supramolecular Nanoassemblies.....	7
1.2.1 Micelles.....	9
1.2.2 Vesicles.....	9
1.2.3 Nanofibers.....	10
1.2.4 Nanotubes	10
1.3 Stimuli Responsive Peptides.....	11
1.3.1 Thermo-responsive Peptides.....	12
1.4 Gene Therapy.....	12
1.4.1 Non-viral Gene Delivery.....	14
1.4.2 Peptide-based Nanoassemblies for Gene Delivery.....	14
1.4.3 Membrane Active Peptides.....	15
1.4.3.1 Tumor-targeting Peptides.....	16
1.4.3.2 Cell-penetrating Peptides.....	17
1.4.3.3 Nuclear Localization Signal.....	18
1.4.3.4 Fusogenic peptides.....	18
1.5 Peptide Synthesis	19
1.5.1 Solid Phase Peptide Synthesis	20
2 Aim of the Thesis.....	22
3 Self-Assembled Peptide Multicompartment Micelles Entrapping and Delivering DNA up to 100 Nucleotides in Length.....	24
3.1 Abstract.....	25
3.2 Introduction.....	26
3.3 Results and Discussion	28
3.3.1 Design, Synthesis and Purification of Peptide Amphiphiles	28
3.3.2 DNA.....	31
3.3.3 Self-assembly of Peptide Nanoparticles	31
3.3.3.1 Solvent Effect on Self-assembly.....	32
3.3.4 Characterization of Peptide Nanoparticles.....	33
3.3.4.1 Morphology.....	33
3.3.4.2 MCM-NP Size	37
3.3.4.3 Surface Charge.....	40
3.3.5 Quantification of DNA Entrapment into Nanoparticles	41
3.3.5.1 FCS method	41
3.3.5.2 NTA method	44
3.3.6 Stability of Peptide Nanoparticles	45
3.3.7 Thermo-responsiveness of Peptide Nanoparticles.....	47
3.3.8 Effect of Peptide Nanoparticles on Cell Proliferation	49
3.3.9 Cell Uptake of Peptide Nanoparticles.....	51

3.4	Conclusion	58
4	Self-Assembled Peptide Nanoparticles Targeting DNA to the Nucleus	60
4.1	Abstract	61
4.2	Introduction	62
4.3	Results and Discussion	64
4.3.1	Design, Synthesis and Self-Assembly of Peptide Amphiphiles	64
4.3.2	Characterization of NLS-MCMs	67
4.3.2.1	Morphology	67
4.3.2.2	Size	68
4.3.2.3	Surface charge	69
4.3.3	Quantification of DNA Entrapment into Nanoparticles	70
4.3.4	Thermo-responsiveness of NLS-MCMs	71
4.3.5	Nuclear Translocation of NLS-MCMs	72
4.3.6	Effect of NLS-MCMs on Cell Proliferation	78
4.3.7	Cell Uptake of NLS-MCMs	80
4.3.8	Ultrastructural Localization of NLS-MCMs in Cells	81
4.3.9	Statistical Analysis of Nuclear Localization of NLS-MCMs	83
4.4	Conclusion	86
5	NLS-MCMs for the delivery of antisense oligonucleotides directed against Bcl-2	87
5.1.1	Morphology of ASO-loaded MCMs	89
5.1.2	Size of ASO-loaded MCMs	90
5.1.3	Charge of ASO-loaded MCMs	91
5.1.4	Cellular uptake of ASO-loaded MCMs	93
5.1.5	Bcl-2 Downregulation by ASO-loaded MCMs	94
6	General Conclusion and Outlook	101
7	Material and Methods	105
7.1	Materials	105
7.1.1	Peptide Synthesis and Purification	106
7.2	Methods	108
7.2.1	Self-assembly of Peptide Nanoparticles	108
7.2.2	Dynamic Light Scattering	109
7.2.3	Zeta-potential	109
7.2.4	Transmission Electron Microscopy	109
7.2.5	Cryogenic Electron Microscopy	109
7.2.6	Nanoparticle Tracking Analysis	110
7.2.7	Fluorescence Correlation Spectroscopy	110
7.2.8	SPR	112
7.2.9	Thermo-responsiveness of Peptide Nanoparticles	112
7.2.10	Cell Culture	113
7.2.11	MTS Cell Viability Assay	113
7.2.12	Cellular Uptake of Peptide Nanoparticles	114
7.2.13	Protein Extraction	114
7.2.14	Evaluation of Bcl-2 Protein Expression by Western Blotting	115
7.2.15	Ultrastructural Analysis of Peptide Nanoparticles in Cells	115
7.2.16	Statistical Analysis of Localized MCMs under live cell conditions	116
	References	118

List of Figures

Figure 1.1: Supramolecular nanoassemblies based on amphiphilic peptides.	8
Figure 1.2: Summary of gene delivery methods.	13
Figure 1.3: Schematic illustration of (A) Tumor-targeting principles of nanocarriers (reproduced with modification from ref. ¹⁰⁵ published by Frontiers), B) CPPs intracellular pathways (reproduced with modification from ref. ¹⁰⁶ published by Elsevier), (C) Active nucleus translocation of nanocarriers (reproduced with modification from ref. ¹⁰⁷ published by American Chemical Society), (D) FP and CPP-mediated delivery (reproduced with modification from ref. ¹⁰⁸ published by Elsevier).	16
Figure 1.4: General scheme of SPPS.	20
Figure 3.1: The amphiphilic peptides (HR)3gT and H3gT comprise a hydrophilic (green) and hydrophobic (purple) domain.	28
Figure 3.2: MALDI-TOF mass spectrum for (A) H3gT and (B) (HR)3gT peptides.	30
Figure 3.3: 5% MetaPhor agarose gel showing single-stranded and double-stranded 22nt and 100nt DNA fragments. Ds DNA was obtained by annealing complementary oligonucleotides: 10mM sense and antisense oligonucleotides in Tris-HCl/1mM EDTA, pH 8 supplemented with 50 mM NaCl were heated to 95°C and gradually cooled down to 10°C over 50min... ..	31
Figure 3.4: Self-assembly process of (HR)3gT with 22nt ssDNA dissolved at 20%, 35%, and 50% final ethanol concentrations. Scale bars = 200nm.	32
Figure 3.5: Ultrastructural morphology of peptide nanoparticles. (A) Overview TEM micrograph of (HR)3gT MCM-NPs, scale bar = 500 nm. (B) Schematic representation and high magnification image of self-assembled multi-compartment micelle nanoparticles in the absence of DNA, scale bar = 100 nm. (C) TEM micrographs of (HR)3gT and H3gT MCM-NPs. Scale bars = 200 nm.	34
Figure 3.6: TEM micrographs of (HR)3gT and H3gT MCM-NPs in the presence of 22 nt ssDNA (upper panels) and 22 bp dsDNA (lower panels). Scale bars = 200 nm.	35
Figure 3.7: TEM micrographs of (HR)3gT and H3gT MCM-NPs in the presence of 100 nt ssDNA (upper panels) and 100 bp dsDNA (lower panels). Scale bars = 200 nm.	36
Figure 3.8: DLS of (HR)3gT MCM-NPs. (A) 22 nt ssDNA-loaded (HR)3gT compared to H3gT MCM-NPs, (B) 22 bp dsDNA-, (C) 100 nt ssDNA- and (D)100 bp dsDNA-loaded (HR)3gT MCM-NPs.	37
Figure 3.9: Normalized FCS autocorrelation curves showing incorporation of (A) Atto550-labeled 22 nt ssDNA in (HR)3gT MCM-NPs (light green), (B) Atto550-labeled 22 bp dsDNA in (HR)3gT MCM-NPs (light blue), (C) Atto550-labeled 100 nt ssDNA in (HR)3gT MCM-NPs (orange), (D) Atto550-labeled 100 bp dsDNA in (HR)3gT MCM-NPs (pink). Atto550 free dye is shown in red in all panels.	42
Figure 3.10: Stability of (HR)3gT MCM-NPs at 4°C. From top to bottom: (A) D_H by DLS over 150 days, (B) Corresponding TEM after 150 days for (HR)3gT MCM-NPs, 22 nt ssDNA-loaded (HR)3gT MCM-NPs, 22 bp dsDNA-loaded (HR)3gT MCM-NPs, 100 nt ssDNA-loaded (HR)3gT MCM-NPs, and 100 bp dsDNA-loaded (HR)3gT MCM-NPs. Scale bars = 200 nm.	46
Figure 3.11: TEM micrographs of (HR)3gT MCM-NPs with different DNA loads after (A) 5 h incubation, and (B) 24 h incubation at 37°C. Scale bars = 200 nm.	48

Figure 3.12: TEM micrograph of (A) H3gT NPs, and (B) 22nt ssDNA-loaded H3gT NPs after 5h incubation at 37°C. Scale bars=200nm.	49
Figure 3.13: HeLa cell viability (MTS assays). Cells treated for 24 h with (HR)3gT MCM-NPs (pink), 22 nt ssDNA-loaded (HR)3gT MCM-NPs (green), 22 bp dsDNA-loaded H3gT MCM-NPs (blue), 100 nt ssDNA-loaded (HR)3gT MCM-NPs (orange), 100 bp dsDNA-loaded (HR)3gT MCM-NPs (purple). Cell viability was normalized to untreated HeLa cells (negative control, 100% viability). All data presented as the mean \pm SD (n = 3).	50
Figure 3.14: CLSM merged images (GFP and Atto550) of H2B-GFP expressing HeLa cells treated with free Atto550-labeled DNAs. Images are recorded under the same conditions as in Figure 3.15. Scale bars = 20 μ m.	52
Figure 3.15: CLSM merged images (GFP and Atto550) of H2B-GFP expressing HeLa cells treated with Atto550-22nt ssDNA-loaded H3gT (<i>left</i>) and (HR)3gT MCM-NPs (<i>right</i>) for 24h. Scale bars = 20 μ m.	53
Figure 3.16: CLSM merged images (GFP and Atto550) of H2B-GFP expressing HeLa cells treated with Atto550-22nt ssDNA-loaded H3gT and (HR)3gT MCM NPs for 48h. Scale bars = 20 μ m.	54
Figure 3.17: CLSM merged images (GFP and Atto550) of H2B-GFP expressing HeLa cells treated with Atto550-22bp and 100nt/bp ss/dsDNA-loaded (HR)3gT NPs after 24h. Imaging conditions were as in Fig. 3.16. Scale bars = 20 μ m.	55
Figure 3.18: Time course of Atto550-100bp dsDNA-loaded (HR)3gT MCM NP uptake. Scale bars = 20 μ m.	56
Figure 3.19: (A) TEM images of 100bp dsDNA-loaded (HR)3gT MCM-NPs after 1h (<i>left</i>) and 2h (<i>right</i>) incubation at 37°C. Scale bars = 200nm. (B) CLSM merged images (GFP and Atto550) of H2B-GFP expressing HeLa cells treated with 100bp dsDNA-loaded (HR)3gT MCM NPs for 1h (<i>left</i>) and 2h (<i>right</i>). Scale bars = 40 μ m.	57
Figure 4.1: Amino acid sequence of the amphiphilic NLS-peptide ((KR)2(HR)2gT) and its precursor (HR)3gT.	65
Figure 4.2: MALDI-TOF mass spectrum of NLS-peptide.	66
Figure 4.3: Sequential self-assembly process of NLS-peptide in the presence of short ssDNA. .	67
Figure 4.4: Morphology of 22nt ssDNA-loaded NLS-MCMs. (A) TEM, (B) Cryo-EM. Scale bars 100nm.	67
Figure 4.5: TEM image of DNA-free NLS-MCMs, Scale bar = 200nm.	68
Figure 4.6: Hydrodynamic diameter of 22nt ssDNA-loaded NLS-MCMs. (A) DLS, (B) NTA. .	68
Figure 4.7: DLS of DNA-free NLS-MCMs.	69
Figure 4.8: Zeta potential of NLS-MCMs with (red) or without 22nt ssDNA (blue).	69
Figure 4.9: Normalised FCS autocorrelation curves of Atto550-labeled 22nt ssDNA-loaded NLS-MCMs (red) and Atto550-labeled 22nt ssDNA (green). Dotted lines represent experimental auto correlation curves and solid lines are fitted curves.	70
Figure 4.10: TEM and DLS of (A) NLS-MCMs without DNA, (B) 22nt ssDNA-loaded NLS-MCMs after 24, 48 and 60 h incubation at 37°C. Scale bars = 200 nm.	72
Figure 4.11: Selective nuclear transport of NLS-MCMs facilitated by Kaps.(I) and nuclear localization (II) of NLS-MCMs (created with BioRender.com).	73
Figure 4.12: SPR sensograms resolve the binding interactions of Kap α •Kap β •NLS-MCMs, Kap α •Kap β 1•nonNLS-MCMs, and standalone Kap α •Kap β 1 to Nup214 and Nup62. (A) Langmuir isotherms using two-component fit, (B) Langmuir isotherm fits (solid lines) yielding the maximal response signal (Rmax; circles). NLS-MCM binding response measured	

by SPR elicited the highest FG Nup-binding response (blue). NonNLS-MCMs (green) do not bind to the Nup 214 while they demonstrate binding to Nup 62, still lower than NLS-MCMs. Standalone Kap α :Kap β 1 binding is shown in red.	75
Figure 4.13: Langmuir isotherm fits (solid lines) for Kap α •Kap β 1•NLS-MCMs elicit the highest FG Nup-binding response compared to free NLS-peptide as measured by SPR.	77
Figure 4.14: Effect of DNA-free and 22nt ssDNA-loaded NLS-MCMs on cell proliferation at a peptide concentration of 1500 μ g/ml compared to lipofectamine complex with corresponding 22nt ssDNA concentration after 24 h of exposure.	78
Figure 4.15 A) Effect of DNA-free and 22nt ssDNA-loaded NLS-MCMs on MCF-7 cell proliferation at different peptide concentrations after 24 h of exposure. Comparison at 1500 μ g/ml peptide concentration to lipofectamine complex with corresponding 22nt ssDNA concentration. B) lipofectamine-mediated transfection of scrambled oligonucleotides and G339-GAP ASO after 48 h of exposure.	79
Figure 4.16: CLSM merged images of H2B-GFP expressing HeLa cells recorded after 5 h and 24 h incubation with DNA-loaded nonNLS-MCMs and NLS-MCMs. Scale bars, 20 μ m.	80
Figure 4.17: Ultrastructural localization of DNA-loaded NLS-MCMs and nonNLS-MCMs in cells. (A, a-d), Electron micrographs reveal NLS-MCMs accumulation at the nuclear envelope, associated with NPCs, and inside the nucleus. (B) Particles assembled from nonNLS-peptide are occasionally detected near the nuclear envelope. (C) Untreated HeLa-GFP cells. Scale bars, 1 μ m.	82
Figure 4.18: Nuclear accumulation of peptide nanoparticles. Imaris 3D reconstructions from multiple confocal sections of HeLa-GFP cells treated for 10h with (A) DNA-loaded nonNLS-MCMs, and (B) DNA-loaded NLS-MCMs. MCMs are represented by red dots and the nuclear boundaries as green ‘surfaces’, based upon the fluorescence of the corresponding dyes. Displayed spots are at a distance below 0.1 μ m to the nuclear membrane and are considered to be inside the nucleus. Dots are displayed in a center point mode.	83
Figure 4.19: Statistical evaluation of NLS- compared to nonNLS-MCMs localized inside the nucleus and at the nuclear membrane at different time-points by Imaris. Bars represent number of MCMs per nucleus. <i>Top</i> , MCMs detected within a distance of \pm 0.1 μ m to the nuclear membrane were considered on the membrane. <i>Bottom</i> , MCMs at a distance below – 0.1 μ m to the nuclear membrane were considered inside the nucleus. The differences for each time-point were statistically significant between NLS- and nonNLS-MCMs ($p < 0.01$) on both graphs. Error bars represent standard error of the mean (SEM). The number of analyzed nuclei for 5, 10, 36 and 48 h timepoints were 38, 44, 78, 98 and 41, 41, 78, 116 for nonNLS- and NLS-MCMs, respectively.	85
Figure 5.1: TEM micrographs of (A) NLS-MCMs and (B) NonNLS-MCMs loaded with different oligonucleotides. Scale bars = 100 nm.	90
Figure 5.2: DLS measurements revealing the hydrodynamic diameter of (A) NLS-MCMs and (B) NonNLS-MCMs loaded with different oligonucleotides.	91
Figure 5.3: Zeta potential of (A) NLS-MCMs and (B) NonNLS-MCMs loaded with G3139-GAP or G3139.	92
Figure 5.4: CLSM merged images of A549, THP-1stimulated with PMA and MCF-7 cells recorded after 24 h incubation with G3139-GAP- and G3139-loaded NLS- and nonNLS-MCMs. Scale bars, 50 μ m.	94
Figure 5.5: Validation of antibody against (A) Bcl-2, and (B) GAPDH in untreated THP-1, PMA-stimulated THP-1, MCF-7, and A549 cell extracts. For immunoblotting, equal amounts of	

total protein cell extract were loaded in each lane of an anykD precast protein gel and separated by SDS-PAGE. 95

Figure 5.6: Linear relationship between sample concentration and band intensity in Western blot probed with (A, B) antibodies against GAPDH, and (C, D) antibodies detecting Bcl-2..... 96

Figure 5.7: Western blot analysis of Bcl-2 proteins in 10µg of MCF-7 cell lysates (A)NLS and nonNLS MCMs, (B) lipofectamine (positive control). Relative Bcl-2 protein expression to GAPDH upon treatment with (C)NLS and nonNLS MCMs, (D) lipofectamine. 97

Figure 5.8: Therapeutic effects of NLS-MCMs delivering G3139-GAP ASO. A) Western blot analysis of BCL-2 proteins in 6µg of MCF-7 total cell extract after 48 h. GAPDH was used as loading control. B) Quantitative densitometry of the immunoblots; nonNLS-MCM-treated (light grey bars), NLS-MCM-treated (dark grey bars), untreated (black bar). C) BCL-2 expression levels in cells transfected with G3139-GAP relative to scrambled oligo delivered with NLS- or nonNLS MCMs. Data are mean ± s.d. of the relative intensity of the bands from three independent assays (not significant (ns) $p > 0.05$, ** $p < 0.01$ and *** $p < 0.001$). 98

Figure 5.9 Therapeutic effects of cells transfected with lipofectamine/G3139-GAP complex. A) Western blot analysis of BCL-2 proteins in 6µg of MCF-7 total cell extract after 48 h. GAPDH was used as loading control. B) Quantitative densitometry of the immunoblots. Lipofectamine-treated (light grey bars), NLS-MCM-treated (dark grey bars), untreated (black bar). C) BCL-2 expression levels in cells transfected with G3139-GAP relative to scrambled oligo delivered with NLS-MCMs or lipofectamine complexes. Data are mean±s.d. of the relative intensity of the bands from three independent assays..... 99

List of Tables

Table 3.1 Characterization of (HR)3gT and H3gT MCM-NPs, suspended in water, at pH 7.....	39
Table 3.2 Surface charge of (HR)3gT and H3gT MCM-NPs, suspended in water, at pH 7.	40
Table 3.3 Quantification of DNA loading in to (HR)3gT MCM-NPs by FCS.....	43
Table 3.4 Nanoparticle tracking analysis of DNA-free and DNA-loaded (HR)3gT MCM-NPs.	44
Table 4.1 Maximal SPR response signals and equilibrium dissociation constants of nanoparticles/ karyopherin complexes to Nups.....	75
Table 4.2 Maximal SPR response signals and equilibrium dissociation constants of free peptide/ karyopherin complexes to Nups.....	77
Table 5.1 Characterization of NLS- and nonNLS-MCMs loaded with different oligonucleotides, suspended in water, at pH 7.	92
Table 7.1 Sequence of oligonucleotides.	106

Acknowledgments

I would like to express my sincere gratitude to my supervisors, Prof. Cornelia G. Palivan and Prof. Kobi Benenson for providing guidance and valuable feedback throughout this project. Our meetings and conversations were indispensable in inspiring me to think more profoundly and to establish a comprehensive and objective critique. They provided me with the freedom of doing what I had confidence in and encouraged me to strive hard and aim high. I consider myself exceptionally fortunate for having them as my supervisors since they were very supportive and understanding of my personal and family challenges.

I cordially thank Prof. Sandrine Gerber for her kind cooperation as my external referee and Prof. Catherine Housecroft for chairing my defense. A special thank goes to the Swiss Nanoscience Institute (SNI) for the financial support.

I owe Dr. Cora-Ann Schoenenberger a major thank you, who has professionally and personally had my back and put up with my stresses and concerns during the last four years. She was actively and effectively involved in my learning process, guided me through the complex path of research, and taught me how to improve my academic writing. Most importantly, she deeply cared not only about my academic progress but also my well-being.

I would like to thank Dr. Michal Skowicki for kindly helping with this research project during the last very intense academic year.

Special thanks must also go to a number of individuals, Dr. Ioana Craciun, Dr. Serena Rigo, Dr. Bartolomeo Angelici, Riccardo Wehr, Dalila Rocco, Dr. Christoph Stelzer, Dr. Jiten Doshi, Claire Meyer, Dr. Andrea Belluati, Luisa Zartner, Dr. Margaux Dastor, Philip Müller-Thümen, Anthony Abraham Ovie, Vasileios Cheras, Dr. Christina Zelmer, Davy Daubian, Danut Necula, Sven Kasper and to all current and former colleagues from Palivan, Benenson and Meier groups for having them around, discussing scientific and non-scientific topics, and sharing so many moments together. Particularly to Dr. Myrto Kyropoulou for her big heart and cognitive empathy and good knowledge of Iran that created deep and enjoyable conversations, and fulfilling friendship throughout these years and to Stefano Di Leone for his sense of humor and being cool that often turned the tight spots to an amusing topic. I also thank Gabriele Persy for the time she kindly took for my never-ending requests of TEM analysis.

I cannot forget to thank my family for all the unconditional support and all the sacrifices they have made for my education. I simply could not have done this without you.

Last but not least, I cannot thank you enough, my dear Fatemeh and Shahin. You have always been there for me no matter what, have always made me feel confident in my abilities, and have always seen the best in me. Your great faith in me made me a better person and in my life, every single step toward success is because you loved me. Without you, I definitely would have never pursued my dreams and have never ended up in Switzerland.

Abbreviations

2D	Two-dimensional
3D	Three-dimensional
AA	Amino acid
ACN	Acetonitrile
ASO	Antisense oligonucleotide
BSA	Bovine serum albumin
Boc	Butyloxycarbonyl
CLSM	Confocal laser scanning microscopy
CMC	Critical micellar concentration
CPM	Counts per molecule
CPP	CPP Cell-penetrating peptide
Cryo-TEM	Cryo-transmission electron microscopy
D _H	Hydrodynamic diameter
DCM	Dichloromethane
DIC	N,N'-diisopropylcarbodiimide
DLS	Dynamic light scattering
DMF	Dimethylformamide
DNA	Deoxyribonucleic acid
dsDNA	Double stranded DNA
EDTA	Ethylenediaminetetraacetic acid
Eq	Equation
FCS	Fluorescence correlation spectroscopy
FDA	Food and drug administration

FG Nups	Phenylalanine–glycine nucleoporins
Fmoc	Fluorenylmethyloxycarbonyl
gA	Gramicidin-derived sequence
gT	Truncated gA
HEPES	4-(2-Hydroxyethyl)-1-piperazineethanesulfonic acid
HF	Hydrogen fluoride
Kap α	Karyopherin α
Kap β	Karyopherin β
K _D	Equilibrium dissociation constant
MALDI-TOF-MS	Matrix-assisted laser desorption/ionization-time of flight-mass spectroscopy
MCM	Multicompartment micelle
MCM-NP	MCM nanoparticle
mRNA	Messenger RNA
MTS	[3-(4,5-dimethylthiazol-2-yl)-5-(3-carboxymethoxyphenyl)-2-(4-sulfophenyl)-2H-tetrazolium, inner salt]
MWCO	Molecular weight cut-off
NLS	Nuclear localization signals
NP	Nanoparticles
NPC	Nuclear pore complexes
nVGDS	Non-viral gene delivery systems
nt	Nucleotide
NTA	Nanoparticle tracking analysis
PBS	Phosphate buffered saline
PDI	Polydispersity index
pDNA	plasmid DNA
PNF	Peptide-based nanofiber

PNT	Peptide nanotube
RanGTP	Ran guanosine triphosphate
R_{\max}	Maximal SPR binding responses
RP-HPLC	reversed phase high performance liquid chromatography
SEM	Standard error of the mean
siRNA	Small interfering RNA
SPPS	Solid phase peptide synthesis
SPR	Surface plasmon resonance
ssDNA	Single stranded DNA
τ_D	Diffusion time
TEM	Transmission electron microscopy
TFA	Trifluoroacetic acid
TRIS	Tris(hydroxymethyl)aminomethane

Amino acids

H	Histidine
Ile	Isoleucine
K	Lysine
L	Leucine
R	Arginine
W	Tryptophan

1 Introduction

This chapter¹ first provides a general overview of the principal of amphiphile self-assembly with a special focus on amphiphilic peptides. Then, the concept is expanded to how, like letters forming different words, the immense variety of amino acid combinations into distinct sequences allows for tailoring molecules for specific structures and functions. Special emphasis is placed on the importance of developing nanoscale supramolecular structures from pure peptides. The chapter then accentuates combining advantageous properties offered by peptides with the concept of self-assembly to design a nanosized peptide-based carrier with improved properties and functionality for gene delivery. Finally, a brief introduction to solid phase synthesis of peptides used in this thesis as building blocks for supramolecular nanostructures is presented.

1.1 Principle of Amphiphile Self-Assembly

Amphiphiles are natural or synthetic molecules comprising hydrophilic and hydrophobic blocks that can self-assemble into a variety of structures including micelles, vesicles, nanofibers and nanotubes. The thermodynamic incompatibility between the hydrophilic and hydrophobic blocks causes the formation of ordered morphologies with novel structural features at nanoscale⁶.

Amphiphile assembly is driven by weak forces such as hydrogen bonds, steric effects, and hydrophobic and electrostatic interactions. Although these noncovalent interactions govern the self-assembly process, their overall effect is sufficient to stably hold the amphiphilic molecules together⁷. From a thermodynamic point of view, highly ordered self-assembled structures have

¹ Parts of this chapter have been modified and adapted from the following publications:

S. Tarvirdipour, Xinan Huang, Voichita Mihali, C. A. Schoenenberger, C. G. Palivan. (2020), "Peptide-based nanoassemblies in gene therapy and diagnosis: paving the way for clinical application", *Molecules*, 25(15), 3482. <https://doi.org/10.3390/molecules25153482>

S. Tarvirdipour, M. Skowicki, C. A. Schoenenberger, C. G. Palivan. (2021), in preparation

lower entropy compared to their free components in the surrounding. In other words, a minimum energy configuration at equilibrium is prerequisite to develop self-assembled structures ^{8,9}. Notably, the structural variety of self-assemblies results from the inherent molecular curvature of the building blocks which in turn, originates from the size difference between the hydrophilic and hydrophobic blocks ¹⁰. Thus, by specifically tailoring the chemical composition, a wide range of macromolecular nanostructures with different shapes and functionalities can be generated.

Self-assembly is a prominent phenomenon in nature that inspired scientists to exploit corresponding processes in the creation of advanced biomaterials with tunable properties. Amphiphile self-assembly has been widely used to mimic biological systems and obtain highly specific cellular functions ^{11,12}. This has led to extensive applications of amphiphile self-assembly in material science, drug and gene delivery ¹³. In particular, amino acids as the natural building blocks of peptides and proteins with self-assembling properties are widely exploited to produce novel functional biomaterials ¹⁴.

1.1.1 Self-assembly of Amphiphilic Peptides

Peptide self-assembly has emerged as a promising research field in nanomedicine due to the many advantages associated with multifunctional well-defined peptide-based nanoassemblies ¹⁵⁻¹⁸. Common amphiphilic peptides yielding supramolecular assemblies for biomedical applications include linear, ionic complementary, long-chain alkylated and lipo-peptides ¹⁹. To accomplish certain functions in biological systems, the side chain properties of amino acids including hydrophilicity, hydrophobicity, charge, and polarity play a key role ²⁰. In addition, a family of membrane active peptides are inherently capable of conferring targeting or membrane translocating properties upon different bioactive cargoes ^{21,22}.

The main driving force for the self-assembly are non-covalent interactions including hydrophobic and ionic interactions, van der Waals forces, hydrogen bonds, and π - π stacking²³. For example, π - π stacking contributes to the self-assembly of peptides mainly via aromatic residues, whereas hydrogen bonding has a key role in the formation and stabilization of secondary structures²⁴. Lateral connections between peptides with stable β -strand conformations induce extended β -sheet structures that were recognized as basis for nanofiber and nanotube formation. In the β -sheets, the peptides are ordered such that the hydrophobic side-chains point in one direction and the polar side-chains in the other²⁵. Peptides with α -helical structure resulting from hydrogen bonding between the carbonyl group of one amino acid and the amino group 4 residues further down the peptide, are governing micelle and vesicle assembly, as the side chains of the amino acids stick outward from the α -helix and thus, are free to interact²⁶.

Self-assembly of peptides into supramolecular structures takes place when adequate non-covalent interactions between peptide chains occur. Several other factors including concentration, buffer composition (pH, ionic strength), and temperature also influence the self-assembly process²⁴. Significant progress has been made in the field of self-assembly and a large variety of peptide-based supramolecular structures with customized properties have been reported^{20,27}. The ease of “bottom-up” fabrication through rational design of amino acid sequences offers infinite smart nanoscale architectures with sizes ranging from few to hundreds of nanometers²⁸.

1.1.2 Gramicidin

Gramicidin, also called gramicidin D is a channel-forming antibiotic obtained from the soil bacterium *Bacillus brevis* that functions as an ionophore. It consists of 15 L- and D-amino acids [HCO-L-Val₁-Gly₂-L-Ala₃-D-Leu₄-L-Ala₅-D-Val₆-L-Val₇-D-Val₈-L-Trp₉-D-Leu₁₀-L-Trp₁₁-D-Leu₁₂-L-Trp₁₃-D-Leu₁₄-L-Trp₁₅-NHCH₂CH₂OH]. Gramicidin is a heterogeneous mixture of gramicidin

A, B and C, that interchanges the tryptophan at position 11 with either phenylalanine or tyrosine. Isomers with isoleucine in position one also exist ²⁹.

In the membrane, this polypeptide forms small pores that allow transport of monovalent cations but exclude anions ³⁰. Ion channel formation occurs via a unique tertiary β -helix structure, causing two gramicidin molecules to dimerize and span a cellular lipid bilayer ³¹. The hydrophobic alternating D, L configuration plays an important role in helix formation and shields the peptide's backbone from its surrounding. Various types of dimerization exist including double helical dimers, single-stranded helical dimers, in parallel and antiparallel, as well as in left- and right-handed orientations ³².

Gramicidin A (gA) which constitutes about 80% of gramicidin, is the most frequently occurring isomer. It can assemble and form stabilized inter- and intra-molecular structures via π - π stacking of the tryptophan-rich domains ³³. A truncated gramicidin (gT) derived from gA, comprising only the L-tryptophan-D-leucine repeating units ($[-_LW-_{DL}]_n-W-NH_2$) was extensively studied by our group as an effective hydrophobic part in amphiphilic peptides that drives the self-assembly of various structures such as micelles, reverse micelles and multicompartement micelles ³⁴⁻³⁷. The hydrophobic $_LW-_{DL}$ repetitive units are responsible for distinct phi and psi angles of the peptide backbone and hide the backbone inside a β -helical secondary structure ³⁸.

1.2 Peptide-based Supramolecular Nanoassemblies

Recent developments in nanoscience provide unique and new opportunities for developing complex, hierarchical nanostructures through merging simple amphiphile assembly with the advanced concept of supramolecular self-assembly ⁶. Consistent with this notion, peptides have several advantages that make them highly attractive building blocks for tailoring nanoassemblies to biomedical applications ^{21,39,40}. Besides biocompatibility and biodegradability, the sheer

limitless combinations and modifications of amino acid residues are an immense asset when it comes to the assembly of modular, multiplexed delivery systems. Moreover, functions that nature encoded in peptides such as their ability to target molecular recognition sites can be emulated repeatedly in nanoassemblies⁵. Compared to individual peptides, peptide self-assemblies offer several unique features, like multivalent binding, dynamic control of cargo interactions, responsiveness to environmental and cellular cues, and long circulation times *in vivo*⁴¹. Various peptide-based supramolecular architectures such as micelles, vesicles, nanofibers, or nanotubes can be generated via a rational design of the molecular building blocks (**Figure 1.1**)²⁶. As polar and nonpolar regions coexist in amphiphilic peptides, self-assembly can be readily accomplished through microphase separation^{23,42}. Moreover, the hydrophilic-hydrophobic balance, commonly indicated as hydrophilic weight fraction, f_w (wt %: $100MW_{\text{hydrophilic}}/MW_{\text{total}}$) plays a key role in driving self-assembly towards various supramolecular structures and morphologies^{43,44}. Therefore, a specific morphology can be predicted by fine-tuning the weight fractions of the hydrophilic and hydrophobic domains^{45,46}.

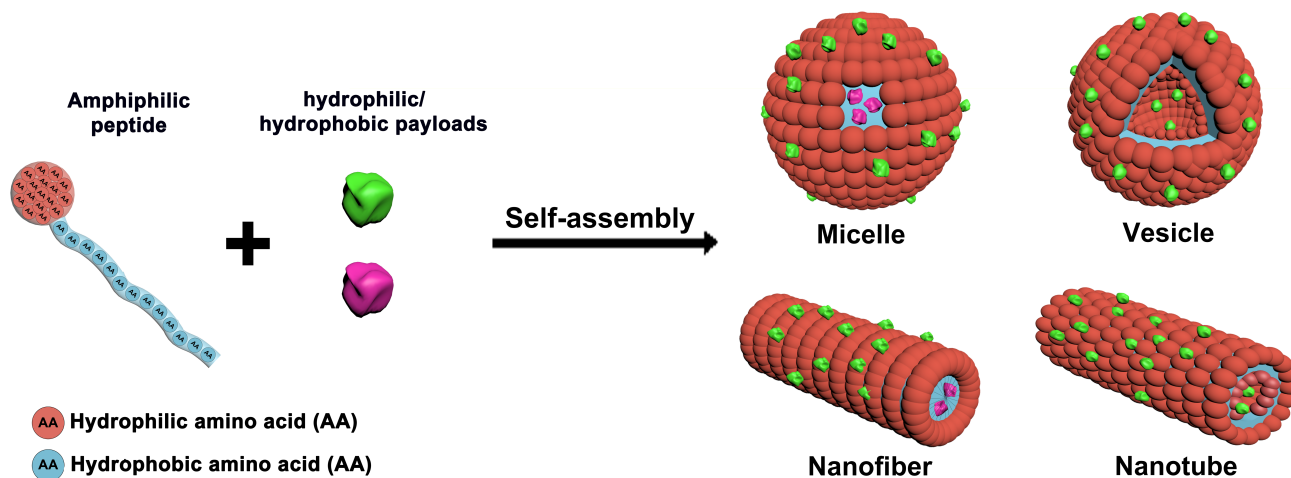


Figure 1.1: Supramolecular nanoassemblies based on amphiphilic peptides.

1.2.1 Micelles

Peptide-based micelles, probably the most prominent self-assembly nanostructures in biomedicine, are closed monolayers consisting of a hydrophobic inner core surrounded by a hydrophilic outer shell (**Figure 1.1**). The spontaneous formation of these well-ordered supramolecular spherical structures with narrow size distribution occurs above a critical micellar concentration (CMC) and can be governed by temperature^{37,47,48}. Direct dissolution and solvent switch are the two most common methods for micelle preparation⁴⁹.

1.2.2 Vesicles

Peptide vesicles are spherical, bilayer-delimited hollow assemblies made from one or more types of amphiphilic molecules (**Figure 1.1**)⁵⁰. Hydrophilic domains are exposed to the inner and outer aqueous environments, whereas hydrophobic residues pack together between hydrophilic interfaces⁵¹. Accordingly, vesicles are capable of encapsulating hydrophilic molecules in the aqueous interior and hydrophobic molecules in the hydrophobic parts of the bilayer⁵². The vesicle size can be tuned by adjusting the composition and chain length of the building blocks^{53,54}.

Self-assembly of pure amphiphilic peptides⁵⁵ and diblock copolypeptides^{56,57} resulted in vesicle formation in aqueous solution. The hydrophobicity of the peptide's tail largely determines whether the peptides assemble into vesicles or nanotubes (see below). Furthermore, surfactant-like peptides with a hydrophilic head domain that consisted of aspartic acid residues, and a hydrophobic tail made of 4–10 glycine residues were shown to self-assemble into vesicles of about 30–50 nm in diameter^{33,58}.

Due to the intrinsic chemical and biological properties of peptides, peptide-based nanovesicles offer several advantages over liposomes such as better membrane fluidity, targeting, biocompatibility and stability^{59–61}.

1.2.3 Nanofibers

Nanofibers are cylindrical structures with a length up to microns and a width typically between 5 to 20 nm (**Figure 1.1**). The high surface to volume ratio provides nanofibers with a large capacity for loading various bioactive molecules including nucleic acids ^{62,63}. Amyloid peptides, ionic self-complementary peptides, collagen-like triple helical peptides, and amphiphilic peptides are able to self-assemble into nanofibers ⁶⁴.

Secondary structure and side-chain interactions are widely perceived to play a crucial role in the self-assembly of nanofibers. While adapting the hydrophobic-hydrophilic balance accordingly, amino acid sequences can be tailored to promote nanofiber formation ⁶⁵. For example, nanofiber self-assembly based on short amphiphilic peptides primarily relies on highly hydrophobic amino acids (Ile or I) and their propensity for β -sheet structuring ⁶⁶. By adopting a β -sheet secondary structure, these peptides elongate into ordered nanofibers ⁶⁷. Besides sheet formation, the collapse of hydrophobic alkyl chains also promotes nanofiber assembly ⁶⁸. Accordingly, amphiphilic peptide nanofibers (PNFs) for gene delivery are composed of three main domains: (1) a hydrophobic tail, predominantly an alkyl chain, (2) a β -sheet forming peptide sequence capable of intermolecular hydrogen bonding, and (3) a hydrophilic head composed of basic amino acids that are positively charged under physiological conditions ⁶⁹. Provided the hydrophilic head is located at the exterior of the nanofibers, bioactive molecules can be entrapped within the network as the self-assembly process occurs ⁶⁵. Thus, PNF self-assembly and functionality greatly depend on all three peptide domains ⁷⁰.

1.2.4 Nanotubes

Peptide nanotubes (PNTs) are three-dimensional, highly organized systems that maintain a well-defined hollow cylindrical shape by molecular interactions of the amphiphilic building

blocks (**Figure 1.1**) ⁷¹. PNTs provide numerous possibilities for smart and/or repetitive functionalization, for example at the head group of the peptide amphiphiles, and thus these versatile structures are candidates for a broad range of applications ⁷². Considering that the hydrophobic tails predominantly composed of the alkyl chains orient towards the core and the amino acid residues to the outer surfaces, the functional groups appear on the outer surfaces of PNTs ⁷³. However, PNTs represent relatively a new concept in nanomedicine and therefore only few examples have been reported so far ⁷⁴.

PNT formation is mainly governed by the peptide sequence and the ensuing intermolecular hydrogen bonds between amino acid residues ⁷³. PNT formation from amphiphilic peptide-derived monomers naturally progresses according to well-established phase diagrams for nanotube assemblies ⁷⁵. Notably, the solution pH and hydrophobicity of peptide monomers are the prominent factors in determining PNT formation and dimensions ^{68,76}.

1.3 Stimuli Responsive Peptides

Stimuli-responsive peptides for biomedical application have gained broad attention due to their propensity of imparting desirable bioactive properties while being biocompatible and biodegradable ⁷⁷. Peptides multi-stimuli responsiveness that triggers conformational changes, can be rationally designed by choosing appropriate amino acid sequences and peptide secondary structural domains ⁷⁸. Non-covalent interactions between amino acids side chains lead to the formation of highly ordered structures such as α -helices, β -sheets, and β -turns. These non-covalent interactions are sensitive to slight environmental changes causing the transformation of the secondary conformation and subsequent changes in peptide structure, bioactivity and functionality ^{79,80}. Therefore, stimuli-responsive peptides are easily customized by introduction of a functional moiety responding to a desirable stimulus. Stimuli-responsive peptides can respond to specific

stimuli including pH, temperature, redox-potential, light, enzymes and change their chemical or physical properties ^{77,78}.

1.3.1 Thermo-responsive Peptides

Temperature has been extensively explored as stimulus to trigger structural changes in peptides ^{81,82}. The conformational change in response to different temperatures varies with the molecular weight of the peptide, the solvent composition and salt concentration ³⁸. Temperature-dependent control over the construction or destruction of self-assembly structures is of particular interest in the triggered release of the encapsulated payloads ³⁸. In addition, slight changes in temperature can result in unfolding of the higher-order structure of peptides with remarkable effects on their solubility which results in inadequate functioning ^{78,83}. This property of both natural and synthetic peptides has been exploited in a wide variety of structures including fibrous hydrogels, micelles, cross-linked micelles and vesicles to achieve a sustainable payload release at physiological temperature ^{79,84,85}.

1.4 Gene Therapy

Gene-based therapy where genetic material is transferred into specific cells is a form of advanced molecular medicine that avoids pharmaceutical compounds and thus eliminates their adverse side effects ⁸⁶. Recent molecular technology approaches allow the precise manipulation of the human genome either by genome editing, gene expression or gene silencing ^{87,88}. Gene therapy is of particular significance in the treatment of inherited diseases, neurological disorders and cancer ³. Maximizing the potential benefits of gene therapy requires efficient and sustained therapeutic gene expression in the target cells, low toxicity, and a high safety profile ⁸⁹. In other words, achieving a successful therapeutic response primarily depends on the efficiency of the vectors used to deliver genetic payloads. The development of appropriate transfection vectors

which are effective, specific, long-term, nontoxic (safe), easy to use, and inexpensive poses a major challenge. Various approaches have been explored to improve the delivery of genetic material to target cells (**Figure 1.2**). For the most part, viral and non-viral delivery systems are used to introduce exogenous nucleic acids into target cells. Besides, several physical methods utilizing different administration routes were developed to facilitate genetic material transfer. Non-viral vectors are based on lipids, polymers, peptides or combinations thereof. Currently, many modifications leading to the generation of the hybrid vectors are being explored in order to optimize the transfection efficiency of non-viral vectors.

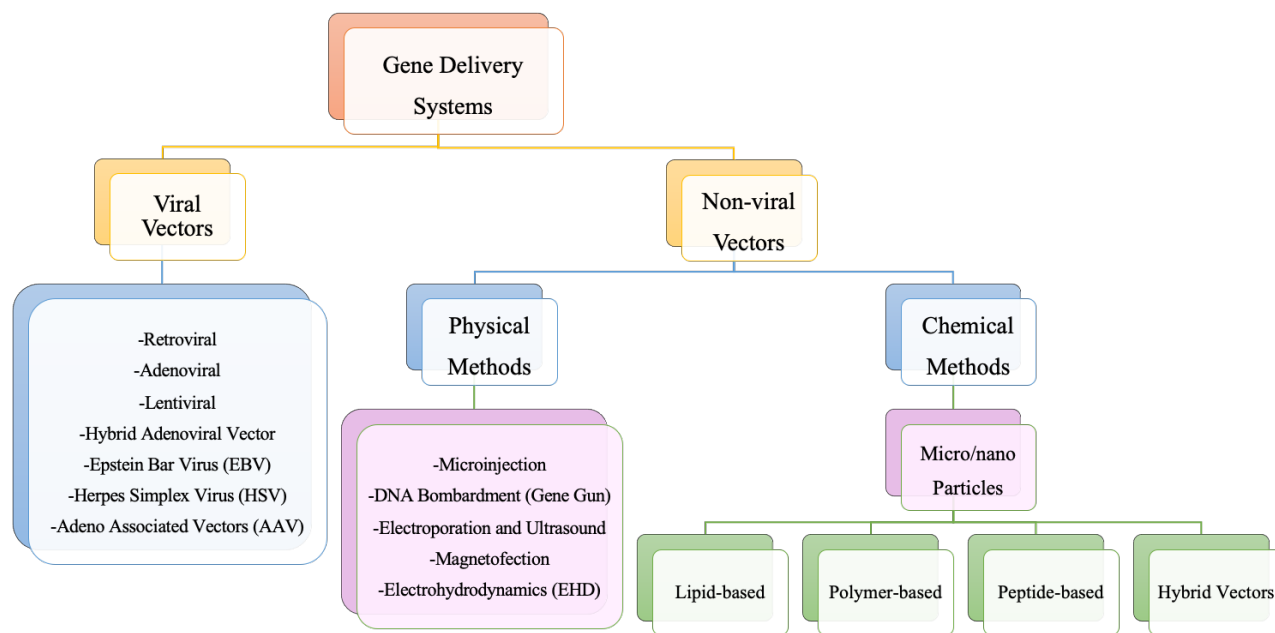


Figure 1.2: Summary of gene delivery methods.

Non-viral gene delivery systems (nVGDS) have several advantages over viral delivery including lower immunogenicity and toxicity, better cell specificity, extensive design flexibility with the option of large-scale production at comparatively low cost⁸⁹. While a few viral-based gene therapy products have been approved by regulatory agencies, an impressive increase in non-

viral products entering various stages of clinical trials has occurred since 2010. Currently, at least 40 nanoparticle-based gene therapy-oriented systems are applied in clinics ⁹⁰.

1.4.1 Non-viral Gene Delivery

The drawbacks associated with a viral strategy such as high immunogenicity, mutagenicity, limitation in size of transgenic DNA, low availability of suitable vectors, and high development and manufacturing cost, led to a boost of non-viral systems ⁹⁰⁻⁹². Subsequently, strategies based on the encapsulation/entrapment of DNA within nanometer size systems (micelles, vesicles, nanofibers, nanotubes and nanoparticles) moved into the limelight ^{5,90}. So far, several types of nanoparticles have been studied for DNA delivery, for example quantum dots, carbon nanotubes, gold nanoparticles, silica nanoparticles, and polymer-, lipid- or peptide-based nanoparticles ⁹³. While remarkable progress has been made in the field of non-viral delivery systems, fundamental limitations concerning the ability of vectors to safely and precisely introduce genetic material into cells remain. Peptide-based vectors hold promise to overcome these limitations due to their exceptional properties such as the propensity for cellular targeting and promoting membrane fusion. This has led to an extensive exploration of peptide-based vectors compared to other non-viral gene delivery systems ⁹⁴.

1.4.2 Peptide-based Nanoassemblies for Gene Delivery

Peptides as non-viral gene delivery vectors are particularly attractive as they offer nearly limitless design options, higher biocompatibility and biodegradability, high binding affinities and increased cellular penetration ⁹⁵. Playing an important role as modulators of many cellular functions ⁹⁶, peptides are exploited for successful gene delivery ^{21,22}. For example, there is increasing evidence for the incorporation of peptides as recognition/targeting moieties and gene delivery modules in a broad range of biomedical applications ⁹⁷. However, studies involving the

self-assembly of supramolecular nanoparticles from pure peptides for DNA delivery delivery are rare ^{98,99}. To the best of our knowledge, parameters conducive to the entrapment and delivery of DNA molecules have so far not been systematically investigated for pure peptide nanoassemblies.

Well-defined pure peptide-based nanoassemblies for gene delivery consist of three basic components, (i) hydrophobic amino acids governing the self-assembly process through intermolecular noncovalent interactions and the subsequent formation of secondary structures, and, (ii) hydrophilic amino acid residues to stabilize the specific structure in a biological environment, and (iii) positively charged amino acid residues to interact electrostatically with negatively charged DNA. Various cationic peptides comprising different combinations of lysine, arginine and histidine residues have been exploited for nucleic acid condensation ¹⁰⁰. Another attractive feature of peptide assemblies for gene delivery is that multiple functions can be integrated into an individual peptide chain, such as a DNA-condensing domain and a receptor-targeting domain. The design flexibility and potency of peptides make them potent tools for mediating intracellular DNA delivery. Membrane active peptides for cell-specific targeting, promoting endosomal escape or nuclear translocation open a new era in the field of non-viral gene delivery.

1.4.3 Membrane Active Peptides

The incorporation of membrane-active peptides, i.e. peptides that exert their biological activities by interacting with the cellular membranes, into gene delivery systems has been found to enhance the translocation of therapeutic nucleic acids into target cells ^{101,102}. The degree of enhancement depends on the characteristics of both, delivery system and membrane-active peptide ¹⁰³. A targeting peptide has to serve at least two major functions: (i) targeting to specific cell types and (ii) promoting intracellular delivery ¹⁰⁴. In nanomaterials engineering, a large variety of

membrane-active peptides including tumor-targeting-, cell-penetrating-, nuclear localization signal- (NLS) and fusogenic peptides have shown great promise in developing accurate and highly targeted delivery systems (**Figure 1.3**)^{105–108}.

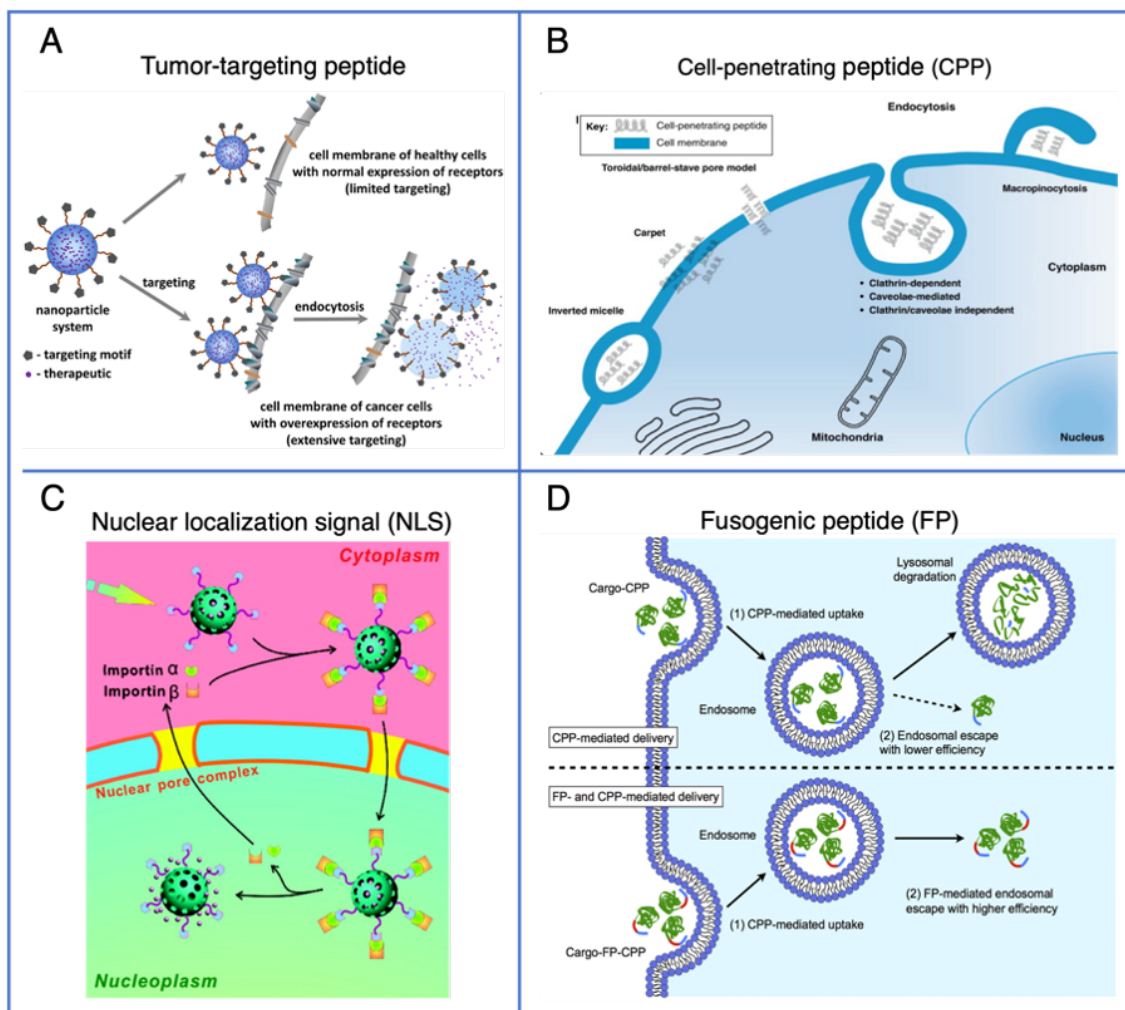


Figure 1.3: Schematic illustration of (A) Tumor-targeting principles of nanocarriers (reproduced with modification from ref. ¹⁰⁵ published by Frontiers), B) CPPs intracellular pathways (reproduced with modification from ref. ¹⁰⁶ published by Elsevier), (C) Active nucleus translocation of nanocarriers (reproduced with modification from ref. ¹⁰⁷ published by American Chemical Society), (D) FP and CPP-mediated delivery (reproduced with modification from ref. ¹⁰⁸ published by Elsevier).

1.4.3.1 Tumor-targeting Peptides

Despite great advances in the development of cancer nanotherapeutics over the past few years, there is still a pressing need for efficient methods to overcome the drawbacks of currently

available intracellular delivery mechanisms ¹⁰⁹. The aberrant proliferation of tumor cells and the up-regulation of their molecular markers result in high levels of specific receptors in the tumor and its microenvironment ¹¹⁰. Selective targeting of these tumor-specific markers promises the accurate targeting of dysregulated signaling pathways (**Figure 1.3A**) ¹¹¹. Although the use of antibodies to target tumors has become highly successful both in tumor diagnosis and therapy, some deficiencies associated with antibodies such as inadequate pharmacokinetics and tissue accessibility as well as impaired interactions with the immune system hamper their clinical application. Compared to antibodies and other tumor-targeting ligands, peptides offer better cell/tissue penetration and improved pharmacokinetics by chemical modifications besides exhibiting high affinity and targeting specificity, low immunogenicity and high stability ¹¹².

1.4.3.2 Cell-penetrating Peptides

The cell-penetrating capacity of specific peptides provides the opportunity for therapeutic molecules to pass through the cell membrane which leads to an enhanced intracellular distribution and thus, a larger therapeutic window (**Figure 1.3B**) ¹¹³. Cell-penetrating peptides (CPPs) have been successfully used for intracellular delivery of a wide variety of cargos including nucleic acids and imaging agents ^{114,115}. Genetic materials can be conjugated to CPPs either by non-covalent complex formation or by covalent bonds ¹¹⁶. Penetration of nucleic acids across the cell membranes paves the way for efficient gene therapy which is a key step in gene delivery ¹¹⁷. Therefore, the translocation properties of CPPs give rise to development of new, potent imaging tools and non-viral vectors for cell transfection ^{118–121}. CPPs either correspond to parts of naturally occurring proteins or are entirely synthetic ¹²². Moreover, CPPs can be classified as cationic, amphipathic, and hydrophobic according to their physical-chemical properties which relate to the type of cell-membrane interactions and uptake mechanisms ¹²³.

1.4.3.3 Nuclear Localization Signal

Over the past years, researchers have realized that one of the major impediments to effective non-viral gene delivery is nucleocytoplasmic transport^{124,125}. For the majority of nucleic acids, once they penetrate across the plasma membrane, they must translocate into the nucleus where they can be either transcribed into the messenger RNA (mRNA)^{126,127} or interfere with transcription and RNA processing. Short peptide motifs called nuclear localization signal (NLS) are able to deliver foreign macromolecules into the nucleus¹²⁸. Active transport of macromolecules to the nucleus is mediated by NLS interactions with importin receptors (karyopherins) at the nuclear pore complexes (NPCs) (**Figure 1.3C**)¹²⁹. To initiate active importin-mediated nuclear transfer, a complex of karyopherin- β and karyopherin- α with bound to NLS-cargo interacts with specific proteins of the nuclear pore complex¹³⁰.

Considering the fact that the nuclear membrane is a major barrier restricting transgene expression for most non-viral vectors, gene therapy is the obvious application field for these versatile peptides¹³¹. The significance of incorporating NLS peptides into non-viral delivery systems to favor release of genetic materials into the nucleus is illustrated by expanding case studies^{124,132}. For gene delivery purposes, positively charged NLS peptides can either electrostatically interact with negatively charged DNA or covalently couple to the condensing agent of the non-viral vector or to the phosphate backbone of the DNA¹³¹.

1.4.3.4 Fusogenic peptides

One of the popular strategies to promote endosomal escape and enhance gene delivery efficiency is functionalizing the non-viral vectors with fusogenic peptides. Fusogenic peptides are a class of short peptides with the potential to cause membrane destabilization and thereby support the delivery of genetic material to the cytosol and/or nucleus¹²⁰. Fusogenic peptides with

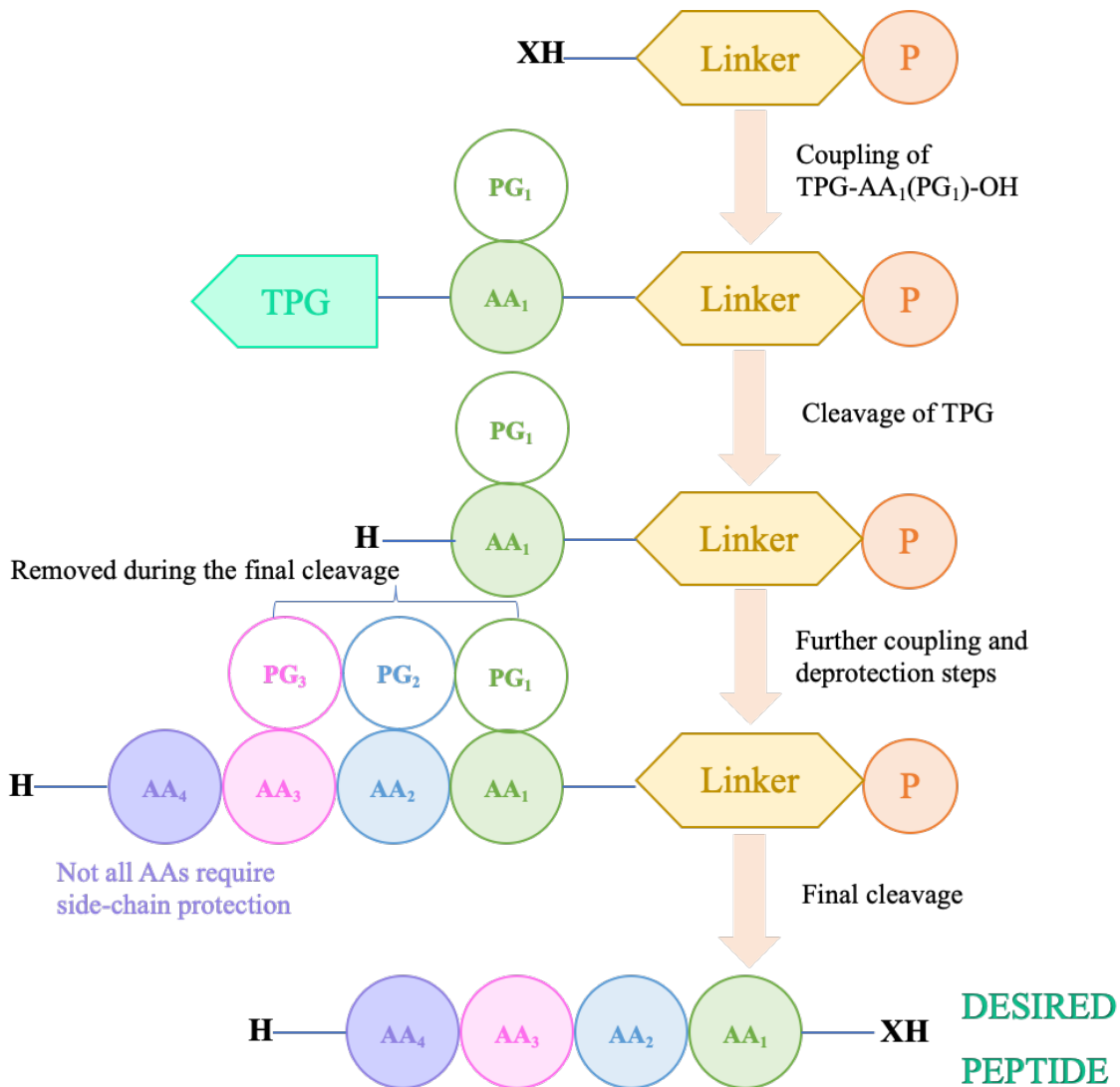
hydrophilic and hydrophobic domains are able to form helical structures at endosomal pH which allow for direct interactions with the endosomal membrane. The resulting conformational changes first induce pore formation in the membrane, ending in the disruption of the endosomal compartment which allow the vectors to escape the endolysosomal network and release their cargos (**Figure 1.3D**). This process presents a remarkable approach to overcome gene delivery barriers, i.e. the endosome, in order to facilitate DNA delivery to the site of action, namely the nucleus¹¹⁷. However, before integrating fusogenic peptides into gene delivery systems, the cellular uptake mechanism should be considered. Since the fusogenic activity of these peptides is due to a pH-dependent conformational change, non-acidic endocytosis pathways such as caveolae-mediated endocytosis and macropinocytosis will withstand their membrane lytic activity¹³³. Fusogenic peptides are either derived from the transduction domains of proteins that interact with cell membranes such as HA2, INF7, or melittin peptides or are synthetic amphipathic peptides shown to traverse membranes, for example GALA, KALA, RALA, and JTS-1^{101,133}.

1.5 Peptide Synthesis

The covalent connection of 2 amino acids (AAs) through an amide bond where the α -carboxyl group of one AA forms a bond with the α -amino group of the adjacent AA, also referred to as peptide bond, leads to peptide formation¹³⁴. Peptide synthesis for research and development purposes is predominantly based on the successive coupling of AAs according to a defined sequence on a solid state. Solid phase peptide synthesis (SPPS) reported in 1963 by B. Merrifield was a major breakthrough in peptide chemistry and became increasingly prevalent in commercial applications^{135,136}.

1.5.1 Solid Phase Peptide Synthesis

Solid phase peptide synthesis (SPPS) is the stepwise linking of a defined AA chain that is covalently attached to the functional beads of an insoluble resin beads, the so-called solid phase (Figure 1.4). The elongation of the peptide up to a maximum length of ~50 AA is followed by cleavage of the final peptide from the resin¹³⁷. The major advantage of SPPS is that intermediate by-products can easily be removed by washing and filtration steps¹³⁸.



X=O, NH PG=protecting group P=polymer support TPG=temporary protecting group

Figure 1.4: General scheme of SPPS.

The Boc-strategy was the first SPPS method that protected the individual AA with a Boc-protective group. To couple the next amino acid, first the N-terminal amine has to be deprotected with trifluoroacetic acid (TFA) followed by several neutralization and washing steps, and then, in the presence of a suitable activator, the amide bond between the two AAs is formed. After repeating the deprotection and coupling cycles until the desired peptide sequence is generated, the final cleavage from the resin is performed with highly toxic hydrogen fluoride (HF). The crude peptide in the cleavage cocktail is then filtered from the resin, precipitated in organic solvent and collected by centrifugation ¹³⁹. Fifteen years later, the Boc-strategy was replaced with the less dangerous Fmoc-strategy for the protection of amino acids which since then became the most common SPPS strategy ¹⁴⁰.

2 Aim of the Thesis

Promising results in basic and clinical research over the past decade have led to substantial financial investments in developing oligonucleotide therapeutics. Although viral vectors were established as promising gene delivery platforms, safety concerns associated with these systems called for novel approaches with the potential to overcome this hurdle. In the past few years, non-viral vectors became widely used tools for safe and effective delivery of genetic materials. However, the inherent complexity of non-viral vector behavior in biological systems, which is mainly related to their physical and chemical properties, impede their advancement. The physicochemical properties of vectors can profoundly influence their cellular delivery, organ distribution and ultimate transfection efficiency. Clearly, these are strong incentives for scrutinizing the development of a well-characterized, safe and efficient non-viral delivery system. Among non-viral vectors, peptides have received increasing attention due to their propensity to overcome biological barriers through cell specific interactions, in addition to their biocompatibility and biodegradability.

For the above-mentioned reasons, the aim of this thesis was to elaborate on criteria and features associated with the design and synthesis of amphiphilic peptides as building blocks of self-assembling nanoparticles for gene delivery applications. Peptide amphiphiles offer a wealth of options for developing self-assembled nanostructures with high level of precision and vast diversity in biochemical (specificity, intrinsic bioactivity, biodegradability) and physical (small size, conformation) properties. While there are numerous peptides incorporated as functional motifs into non-viral gene delivery systems^{4,5,101}, the number of purely peptidic nanoassemblies for nucleic acid delivery reported, is limited¹⁴¹. So far, the only purely peptidic nanoassemblies studied *in vivo* are peptiplexes¹⁴².

The urgent need for a versatile non-viral delivery system with advanced physicochemical properties that allows for the efficient incorporation of DNA other than single-stranded short antisense oligonucleotides (ASO) motivated us to develop a purely peptidic DNA delivery system. The first goal was to assess the capability of rationally designed peptide amphiphiles for efficient entrapment of oligonucleotides larger than the average ASO while being able to self-assemble. Knowing that the success of non-viral gene delivery systems to a large extent is limited by multiple extracellular and cellular barriers, our focus was on developing peptidic DNA carriers without cytotoxic effects which are readily taken up by cells. The nuclear envelope as one of the major cellular barriers that non-viral vectors have to overcome, directed our attention to targeting peptidic DNA nanocarriers to the nucleus with the objective to improve transfection efficiency. To reach these specifications in our peptide designs, we aimed to combine desired functions with the physicochemical principles of self-assembly. By the systematic characterization of peptidic vectors and subsequent cell studies we wanted to gain a deeper understanding of their self-assembling behavior, genetic payload entrapment and intracellular localization. With this thesis, we seek to provide first cues for the successful application of our purely peptidic nanoassemblies in gene therapy and vaccination.

3 Self-Assembled Peptide Multicompartment Micelles

Entrapping and Delivering DNA up to 100 Nucleotides in Length²

Supramolecular self-assembly is a ubiquitous process which offers “bottom-up” fabrication of a wide variety of complex structures with remarkable simplicity instead of involving multi-step long chemical reactions¹⁴³. By selecting appropriate building blocks prone to self-assembly and integrating desired functionalities, well-defined supramolecular structures can be readily obtained^{144–147,56}. While there are many non-viral nanosystems that are able to deliver plasmid DNA (pDNA) based on conjugation or complex formation of the pDNA with lipids^{148,149}, polymers^{150,151}, and peptides^{18,152–154}, there are very few examples based on the directed self-assembly of supramolecular nanostructures. Peptides as non-viral gene delivery vectors are particularly attractive as they offer nearly limitless design options, higher biocompatibility and biodegradability, high binding affinities and increased cell penetration⁹⁵. However, studies involving the self-assembly of supramolecular nanoparticles from pure peptides as a gene delivery vector are rare^{98,99} and to best of our knowledge, parameters conducive to the entrapment and delivery of DNA molecules have so far not been systematically investigated.

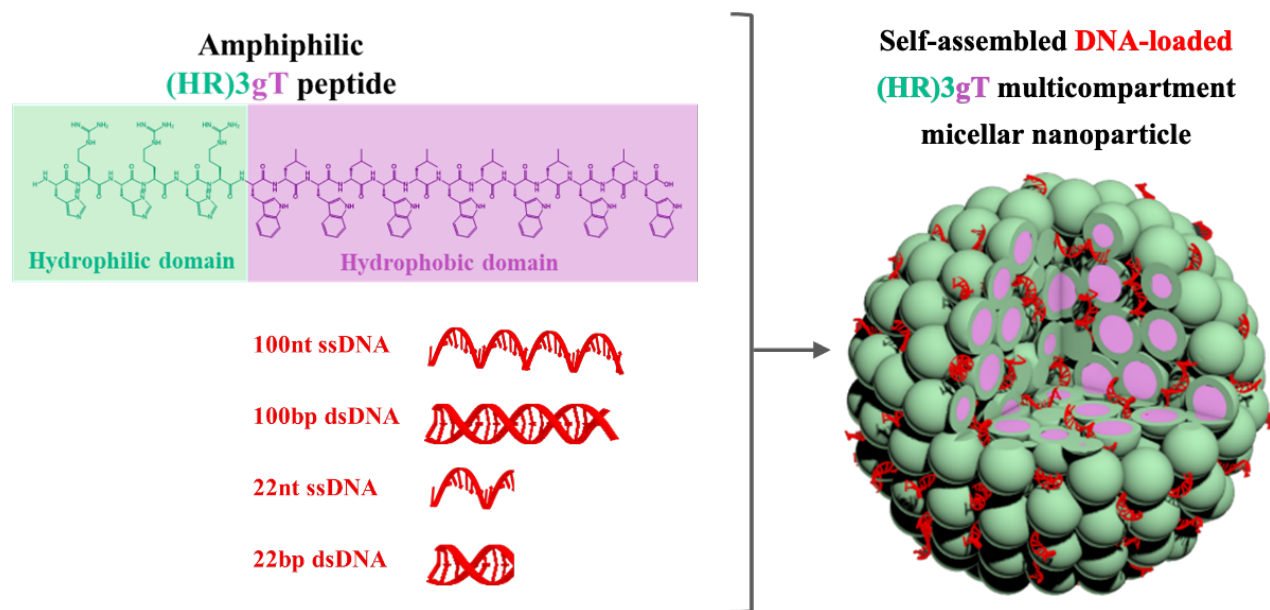
Antisense oligonucleotides (ASOs), i.e. synthetic, single-strand oligodeoxynucleotides that can alter RNA processing and thereby reduce, restore, or modify protein expression represent an outstanding therapeutic platform. To take advantage of the vector properties offered by peptides,

² The results of this chapter have been reprinted and modified from the following publication:

S. Tarvirdipour, C. A. Schoenenberger, K. Benenson, C. G. Palivan. (2020), “A self-assembling amphiphilic peptide nanoparticle for the efficient entrapment of DNA cargoes up to 100 nucleotides in length”, *Soft Matter*, 16(6), 1678-1691.

<https://doi.org/10.1039/C9SM01990A>

and at the same time, start closing the gap in cargo size between ASOs and pDNA, we intended to establish a purely peptidic, self-assembling delivery system that lends itself to the incorporation of single- and double-stranded DNA segments that are larger than the average ASO. In this chapter, we investigated the relationship between the DNA size/type and the self-assembly of peptide nanoparticles and the physicochemical properties of the resulting structures.



3.1 Abstract

To overcome the low efficiency and cytotoxicity associated with most non-viral DNA delivery systems, we developed a purely peptidic self-assembling system that is able to entrap single- and double-stranded DNA of up to 100 nucleotides in length. We rationally designed a peptide, (HR)3gT, which comprises a hydrophilic domain prone to undergo electrostatic interactions with DNA cargo, and a hydrophobic domain at a ratio that promotes self-assembly into multi-compartment micellar nanoparticles (MCM-NPs). Self-assembled (HR)3gT MCM-NP sizes range between 100 to 180 nm which is conducive to a rapid and efficient uptake by cells.

(HR)3gT MCM-NPs had no adverse effects on HeLa cell viability. In addition, they exhibit long-term structural stability at 4 °C, but at 37 °C, the multi-micellar organization disassembles overtime, reflecting thermo-responsiveness. The comparison of (HR)3gT to a shorter, less charged H3gT peptide indicates that the additional arginine residues result in the incorporation of longer DNA segments, an improved DNA entrapment efficiency and an increase in cellular uptake. Our unique non-viral system for DNA delivery sets the stage for developing amphiphilic peptide nanoparticles as candidates for future systemic gene delivery.

3.2 Introduction

Due to numerous disadvantages associated with viral strategies ², non-viral delivery systems emerged as a new breakthrough and have entered various stages of clinical trials since 2010 ⁹⁰⁻⁹². The advantages of non-viral DNA delivery systems include lower immunogenicity, biosafety risk and toxicity, better cell specificity, and ease of large-scale production at low cost. Moreover, they can be synthesized and chemically modified to exhibit physicochemical properties that are tailored to the target disease. Nevertheless, there are major hurdles associated with these systems including inadequate pharmacokinetic properties and clinical efficacy (off-target effects) ^{155,156}. Peptides as non-viral gene delivery vectors are particularly attractive as they might overcome these hurdles apart from the aforementioned advantages ⁹⁵.

A large number of non-viral gene-therapy systems focus on the delivery of antisense oligonucleotides (ASOs) ¹⁵⁷⁻¹⁶⁰. These 20 to 40 nucleotide single-stranded DNAs (ssDNAs) can be designed to mediate target RNA degradation, modify RNA splicing, or block the translation of a specific mRNA ¹⁶¹. Nevertheless, pro-inflammatory effects, inadequate pharmacokinetic properties, off-target effects, and preclinical toxicological challenges are often associated with these systems and represent hurdles that impede their clinical application. Off-target effects are

particularly critical but may be reduced by increasing the length of the ASOs and thus the specificity¹⁶². Despite a number of non-viral systems that deliver ASOs, the ability to entrap DNA sequences larger than 50 nucleotides in length, either single- or double-stranded, has not been systematically explored so far. Evidently, a better understanding of the physico-chemical interactions between the DNA and the carrier would facilitate advancing non-viral ASO delivery systems with regard to incorporation of longer DNA segments. For self-assembling peptide delivery systems, it is vital to systematically assess if and how the type of DNA (ss/ds) and increasing its size will affect the self-assembly of the peptidic nanoparticle.

Here, we report a novel amphiphilic peptide, henceforth called (HR)3gT, that is designed to self-assemble into multi-compartment micellar nanoparticles (MCM-NPs). Compared to H3gT, a previously published amphiphilic peptide that forms MCM-NPs³⁷, we significantly modified the design by adding charged amino acid residues to allow for more electrostatic interactions between peptide and DNA. Specifically, we designed (HR)3gT to include a combination of arginine and histidine residues which was found to boost the cell penetration ability of nanoparticles (NPs) and thus, improve transfection efficacy¹⁶³. Numerous studies document the merits of the superior cell penetrating ability of positively charged arginines compared to lysine^{133,164}. Alongside with the extension of the hydrophilic domain, the hydrophobicity of the peptide was increased to sustain its ability to self-assemble into micelles.

The impact of the modifications incorporated in the design of (HR)3gT was systematically analysed via testing self-assembly in the absence and presence of single- and double-stranded DNA (ssDNA/dsDNA) of 22 and 100 nucleotides in length. Specifically, we examined how the altered physicochemical properties affected the loading efficiency of a 22-nucleotide ssDNA segment. By dissecting the relationship between the type and length of the DNA segment and the

multi-compartment nanoparticle formation, we demonstrate that (HR)3gT NPs can accommodate longer DNA payloads. While emphasizing the importance of the physicochemical properties of peptide nanoparticles in generating a safe and efficient DNA-delivery system, our results pave the way to incorporate protein-coding sequences in peptide assemblies for an efficient gene-based therapy.

3.3 Results and Discussion

3.3.1 Design, Synthesis and Purification of Peptide Amphiphiles

To systematically explore the molecular parameters associated with producing a purely peptidic DNA-delivery system, we designed a 19 amino acid amphiphilic peptide henceforth termed (HR)3gT (**Figure 3.1**). The core of the peptide is based on the 10 amino acid amphiphilic H3gT peptide which has previously been shown to self-assemble into multicompartment micellar nanoparticles (MCM-NPs) when employing the solvent exchange method³⁷.

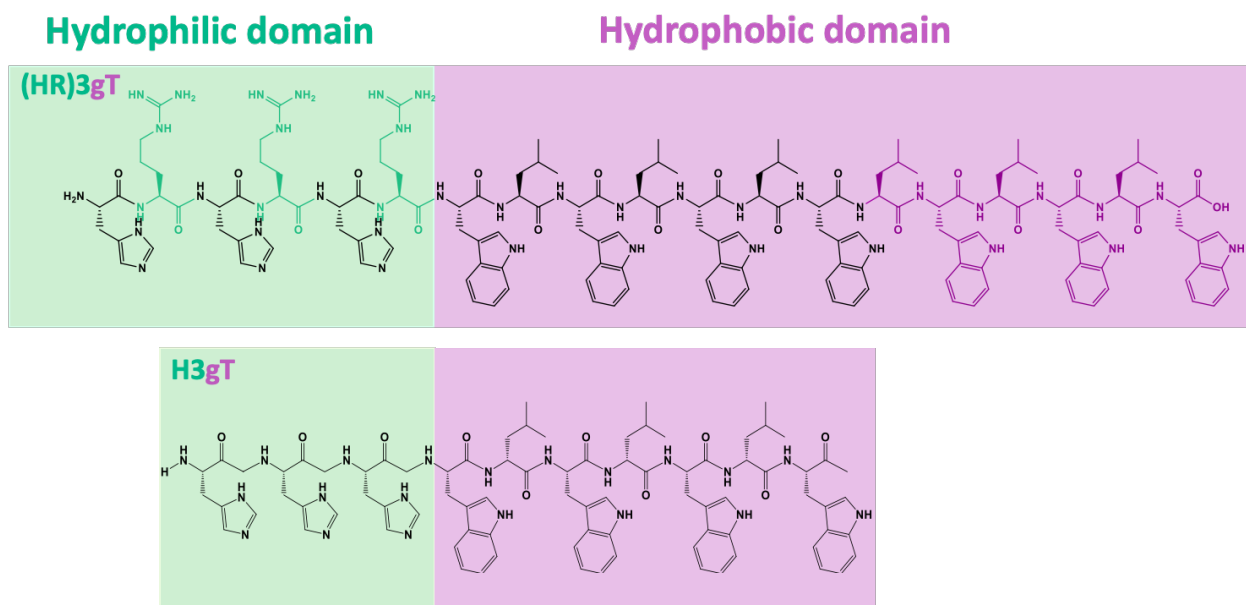
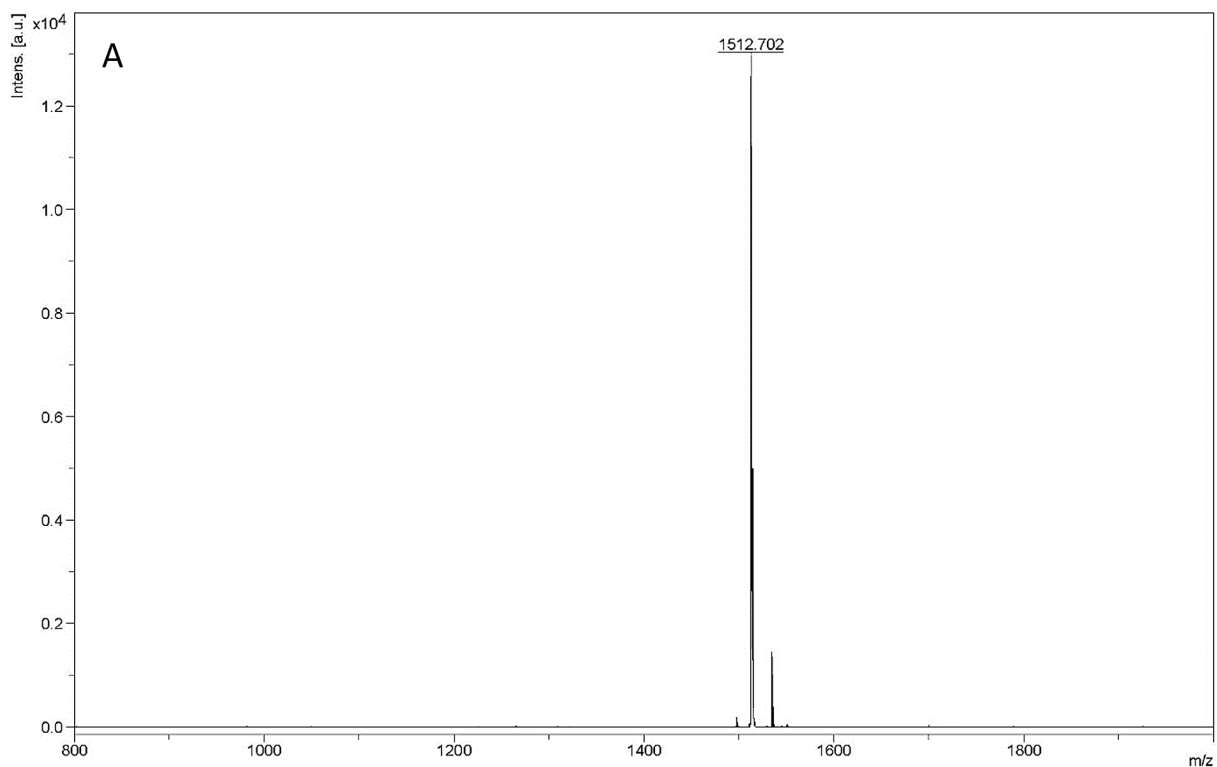


Figure 3.1: The amphiphilic peptides (HR)3gT and H3gT comprise a hydrophilic (green) and hydrophobic (purple) domain.

To accommodate the negative charge of DNA segments during self-assembly, the positive charge of the hydrophilic domain was increased by adding an arginine residue after each histidine. The extension of the hydrophilic domain was compensated by increasing the hydrophobic domain of H3gT from three to six repetitive L-tryptophan-D-leucine [LW-DL] motifs in (HR)3gT (**Figure 3.1**), as the ratio of hydrophilic to hydrophobic domain is a critical determinant for the assembly of micelles^{165,166}. The newly designed (HR)3gT peptide and the 10 amino acid H3gT (for comparison) were synthesized using standard Fmoc-based solid phase peptide synthesis and purified by RP-HPLC. MALDI-TOF mass spectrometry confirmed the expected molecular mass of 2878 g mol⁻¹ for purified (HR)3gT and 1512.7 g mol⁻¹ for purified H3gT (**Figure 3.2**).



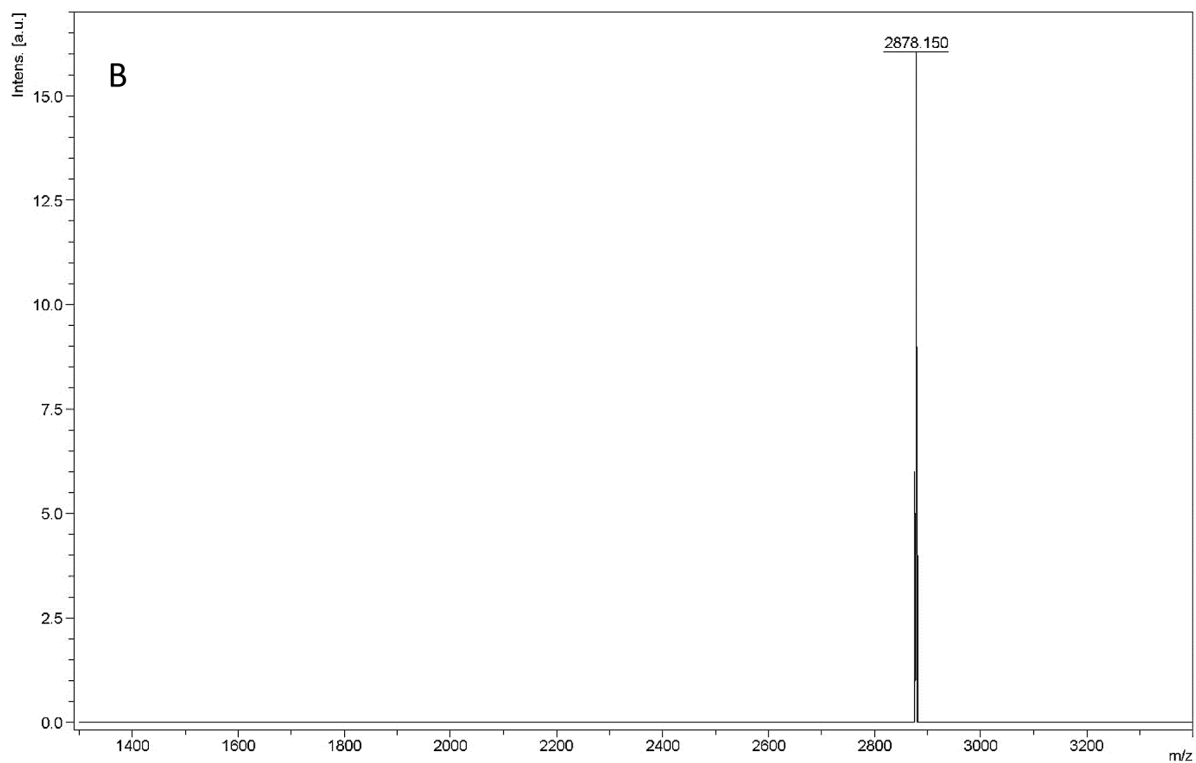


Figure 3.2: MALDI-TOF mass spectrum for (A) H3gT and (B) (HR)3gT peptides.

3.3.2 DNA

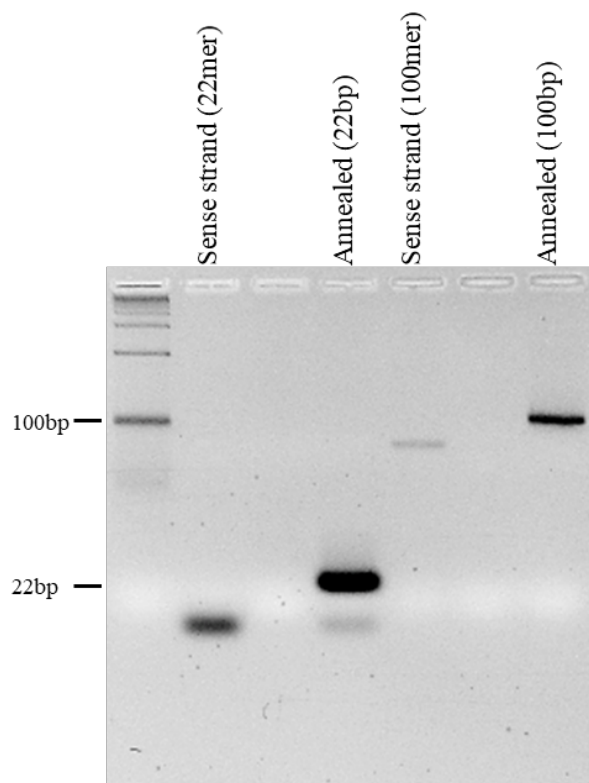


Figure 3.3: 5% MetaPhor agarose gel showing single-stranded and double-stranded 22nt and 100nt DNA fragments. Ds DNA was obtained by annealing complementary oligonucleotides: 10mM sense and antisense oligonucleotides in Tris-HCl/1mM EDTA, pH 8 supplemented with 50 mM NaCl were heated to 95°C and gradually cooled down to 10°C over 50min.

3.3.3 Self-assembly of Peptide Nanoparticles

Previous studies from our group have shown that the micelle and MCM self-assembly process is a function of temperature and solvent composition.³⁵ They demonstrated that there is an equilibrium between individual peptides, micelles and MCMs, and once the MCMs are formed, they exhibit high mechanical stability and preserve their shape and dimensions. To investigate the solvent conditions on the ability of (HR)3gT to form nanoparticles, we tested the self-assembly of the peptide at different ethanol concentrations. Notably, the weight ratio between hydrophilic and

hydrophobic domains in (HR)3gT was designed to be similar to that of H3gT, the latter being prone to micelle formation.

3.3.3.1 Solvent Effect on Self-assembly

To choose the solvent concentration which is conducive to MCM formation in the presence of DNA by solvent exchange method ³⁶, (HR)3gT and 22 nt ssDNA were dissolved at different final ethanol concentrations (20, 35 and 50wt%) and dialysed against milli-Q water at 4 °C. Once solvent exchange was completed, samples were examined by transmission electron microscopy (TEM) (Figure 3.4).

Solvent effect on self-assembly of (HR)3gT peptide and 22nt ssDNA

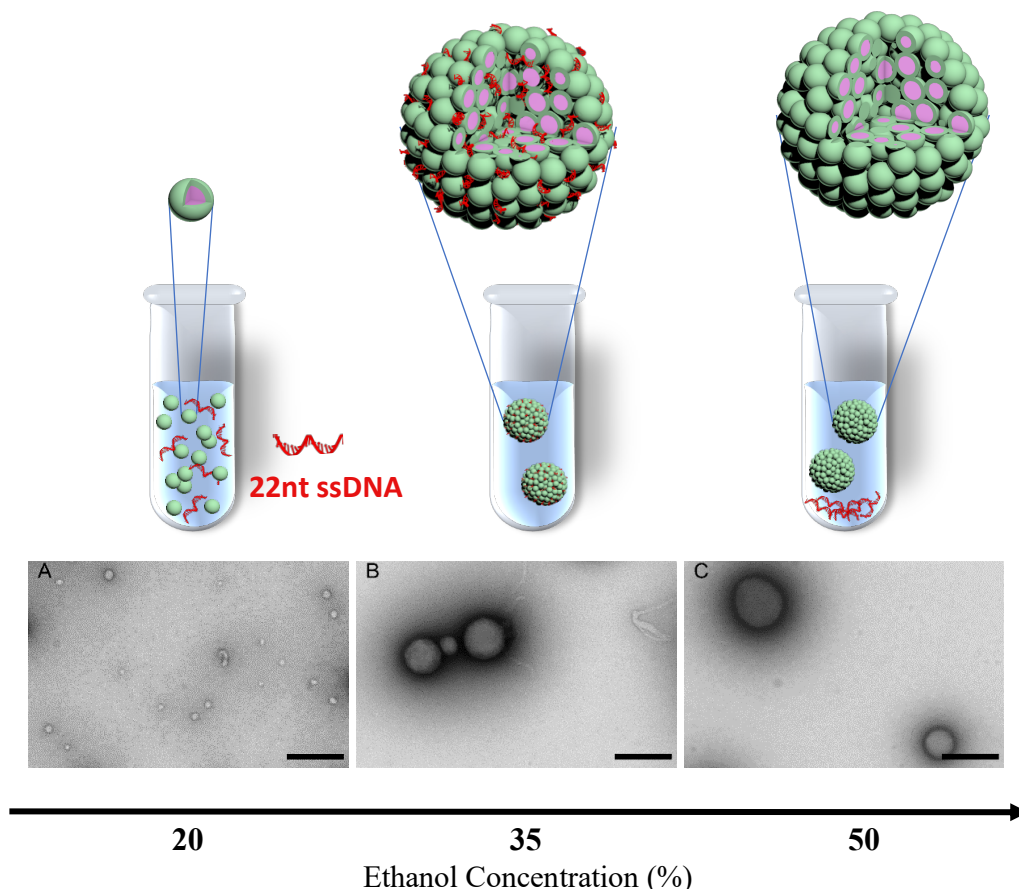


Figure 3.4: Self-assembly process of (HR)3gT with 22nt ssDNA dissolved at 20%, 35%, and 50% final ethanol concentrations. Scale bars = 200nm.

Formation of MCM-NPs was observed at final concentrations of 35% and 50% ethanol, while at 20% ethanol, predominantly individual micelles and smaller MCM-NPs were detected, with few contaminants of un-assembled peptide. However, at 50% ethanol concentration, the 22 nt single stranded DNA precipitated rather than being entrapped into the MCM-NPs as revealed by fluorescently labeled DNA at the bottom of the dialysis tube. Hence, 35% ethanol was chosen as a final solvent concentration to produce self-assembled MCM-NPs and allow DNA incorporation into them.

3.3.4 Characterization of Peptide Nanoparticles

3.3.4.1 Morphology

The ultrastructure of nanoparticles (NPs) resulting from (HR)3gT self-assembly by solvent exchange at 35 wt% ethanol was examined by TEM. An overview micrograph in the absence of DNA revealed round particles ranging in size in the tens of nanometers (**Figure 3.5A**). At higher magnification, TEM indicated a multicompartment organization of the NPs corresponding to the schematic drawing of multi-compartment micellar nanoparticles (MCM-NPs) (**Figure 3.5B**). A comparison of (HR)3gT and H3gT NPs showed that both peptides self-assembled into NPs with a similar multicompartment micellar morphology (**Figure 3.5 C**). Intriguingly, (HR)3gT MCM-NPs appeared smaller than H3gT MCM-NPs in negatively stained specimens.

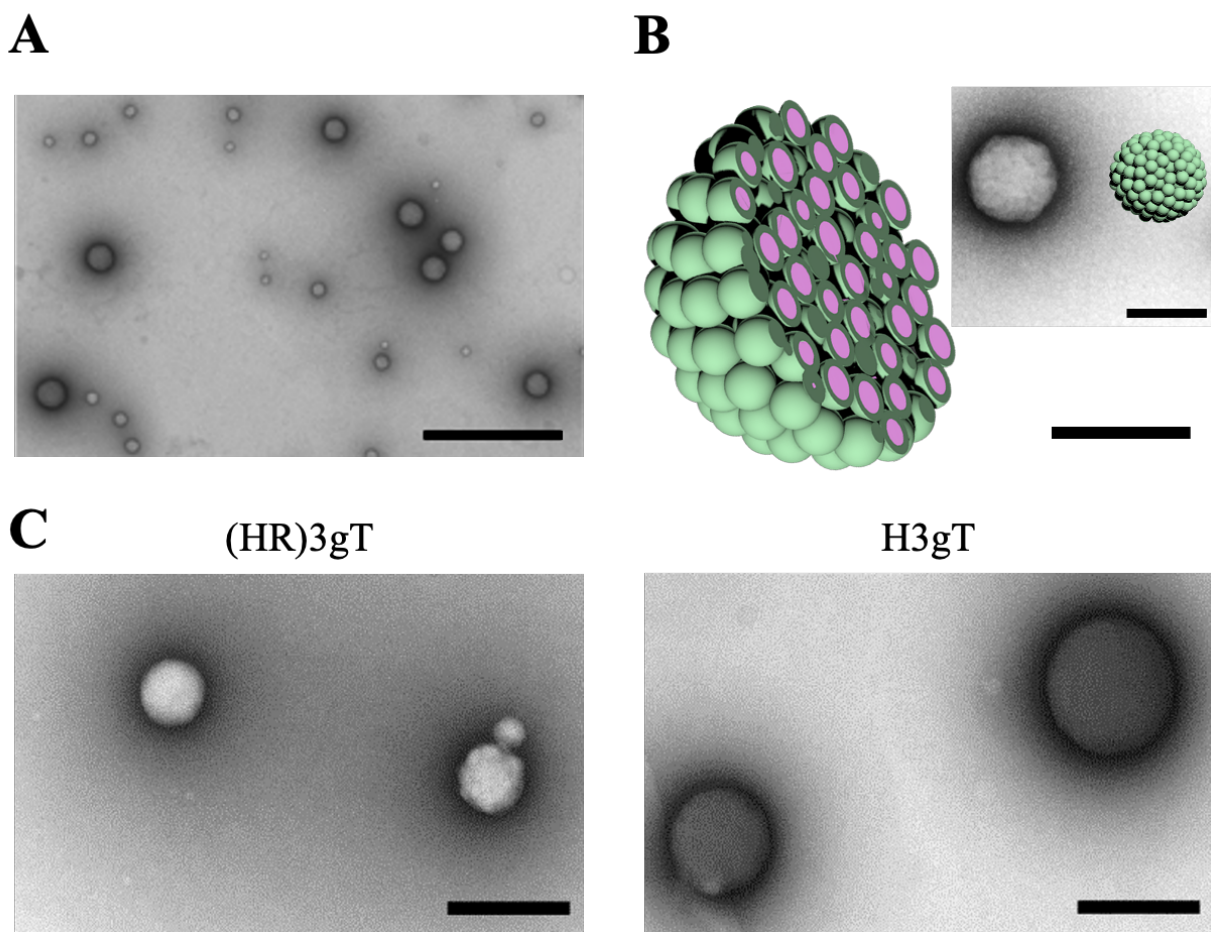


Figure 3.5: Ultrastructural morphology of peptide nanoparticles. (A) Overview TEM micrograph of (HR)3gT MCM-NPs, scale bar = 500 nm. (B) Schematic representation and high magnification image of self-assembled multi-compartment micelle nanoparticles in the absence of DNA, scale bar = 100 nm. (C) TEM micrographs of (HR)3gT and H3gT MCM-NPs. Scale bars = 200 nm.

In the presence of 22 nt ssDNA, ultrastructural analysis by TEM showed that the newly designed (HR)3gT peptide assembled NPs with a multi-compartment micellar architecture similar to that of H3gT MCM-NPs (**Figure 3.6 upper panel**). To test the ability of (HR)3gT to entrap dsDNA, we examined (HR)3gT self-assembly in the presence of 22 bp dsDNA and compared it to H3gT (**Figure 3.6 lower panel**).

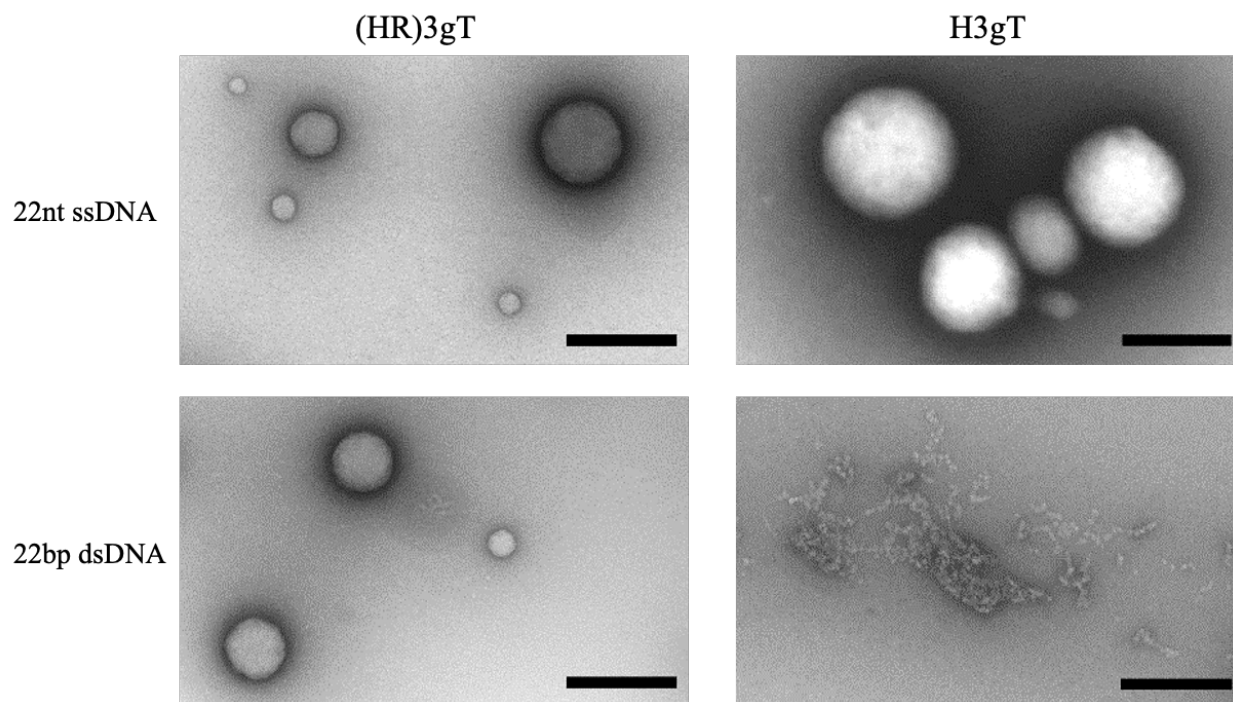


Figure 3.6: TEM micrographs of (HR)3gT and H3gT MCM-NPs in the presence of 22 nt ssDNA (upper panels) and 22 bp dsDNA (lower panels). Scale bars = 200 nm.

In contrast to H3gT, the newly designed (HR)3gT peptide was able to form spherical MCM-NPs also in the presence of double-stranded 22 bp DNA. Conceivably, the higher positive charge of (HR)3gT in comparison to H3gT results in an increased electrostatic interaction between the negatively charged DNA and positively charged peptide. In addition, because dsDNA is more rigid than ssDNA and has double the amount of negatively charged phosphate in its backbone, it is likely to require a higher driving force, i.e. more positive charges that are available for the electrostatic interactions needed to condense the stiffer dsDNA.

To bridge the gap in DNA loading between existing non-viral systems that deliver short single-stranded antisense oligonucleotides and those that are based on complex formation to transfer entire genes, we assessed the self-assembly process of (HR)3gT in the presence of single- and double-stranded DNA sequences of 100 nucleotides in length (**Figure 3.7**).

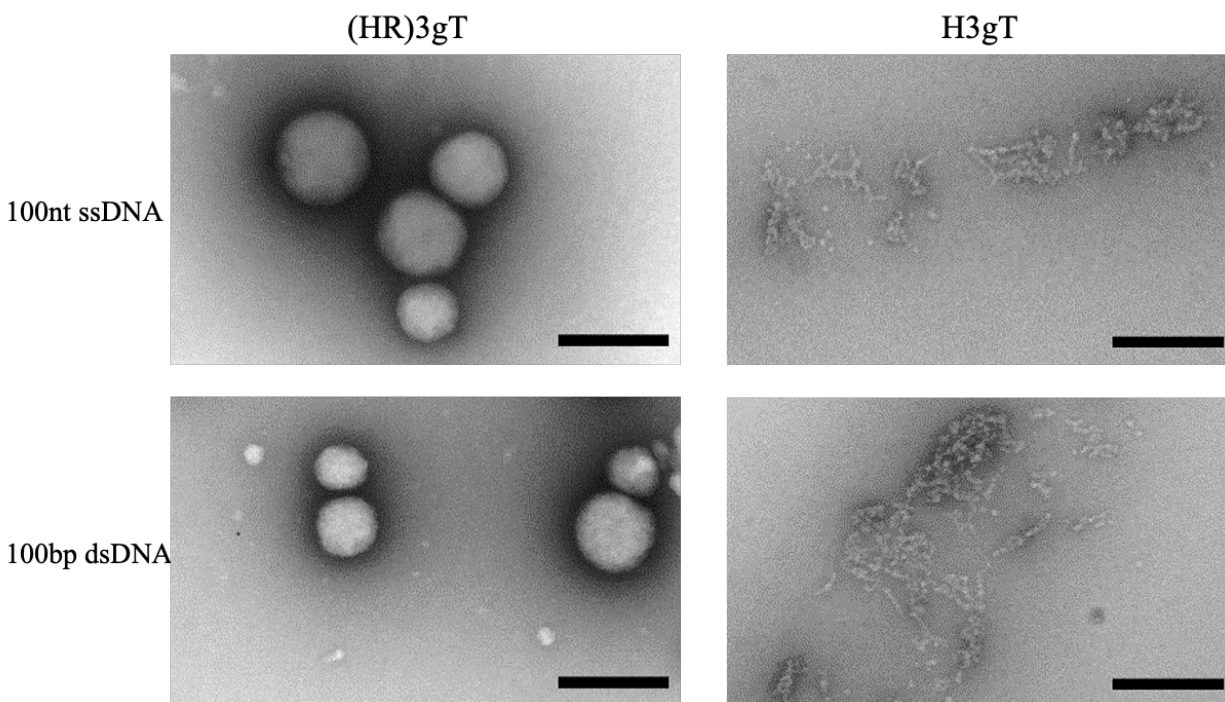


Figure 3.7: TEM micrographs of (HR)3gT and H3gT MCM-NPs in the presence of 100 nt ssDNA (upper panels) and 100 bp dsDNA (lower panels). Scale bars = 200 nm.

While (HR)3gT entrapped both 100 nt ssDNA and 100 bp dsDNA during self-assembly, the shorter, less charged H3gT peptide was not able to self-assemble into MCM-NPs in the presence of the longer DNA segments. In the self-assembly solution at pH 7.1, the net charge of the (HR)3gT peptide is +3 whereas H3gT has a net charge of +0.3 with regard to their isoelectric point. Therefore, H3gT peptide does not provide adequate positive charge to enable electrostatic forces that condense the longer ss/dsDNA. Thus, increasing the positive charge of the hydrophilic domain by arginine residues in (HR)3gT is essential for the entrapment of the longer DNA in MCM-NPs. Although the hydrophilic to hydrophobic weight ratio in (HR)3gT is slightly higher than in H3gT (44.6% compared to 38.4%), it is still within the range where micelles form. Our data suggest that optimizing the charge and tuning the ratio of hydrophilic to hydrophobic domains are key parameters in the development of DNA delivery systems based on peptidic MCM-NPs.

3.3.4.2 MCM-NP Size

Size analysis of DNA-free nanoparticles by DLS showed a hydrodynamic diameter (D_H) of 112 ± 21 nm for (HR)3gT and 211 ± 46 nm for H3gT (Table 3.1). The decrease in MCM-NP diameter for (HR)3gT is consistent with the smaller size observed by TEM (Figure xy). For DNA-loaded (HR)3gT assemblies, the scattered intensities measured by DLS demonstrated a narrow size distribution in the range of 100–180 nm for all DNA payloads (**Figure 3.8 A-D**). It is noteworthy that the average size for 22 nt ssDNA-loaded (HR)3gT NPs was smaller than the corresponding H3gT NPs (160 ± 18 nm versus 241 ± 73 nm in diameter) (Figure 3.8 A). This can be attributed to the higher charge interaction between (HR)3gT and DNA resulting in more compacted NPs.

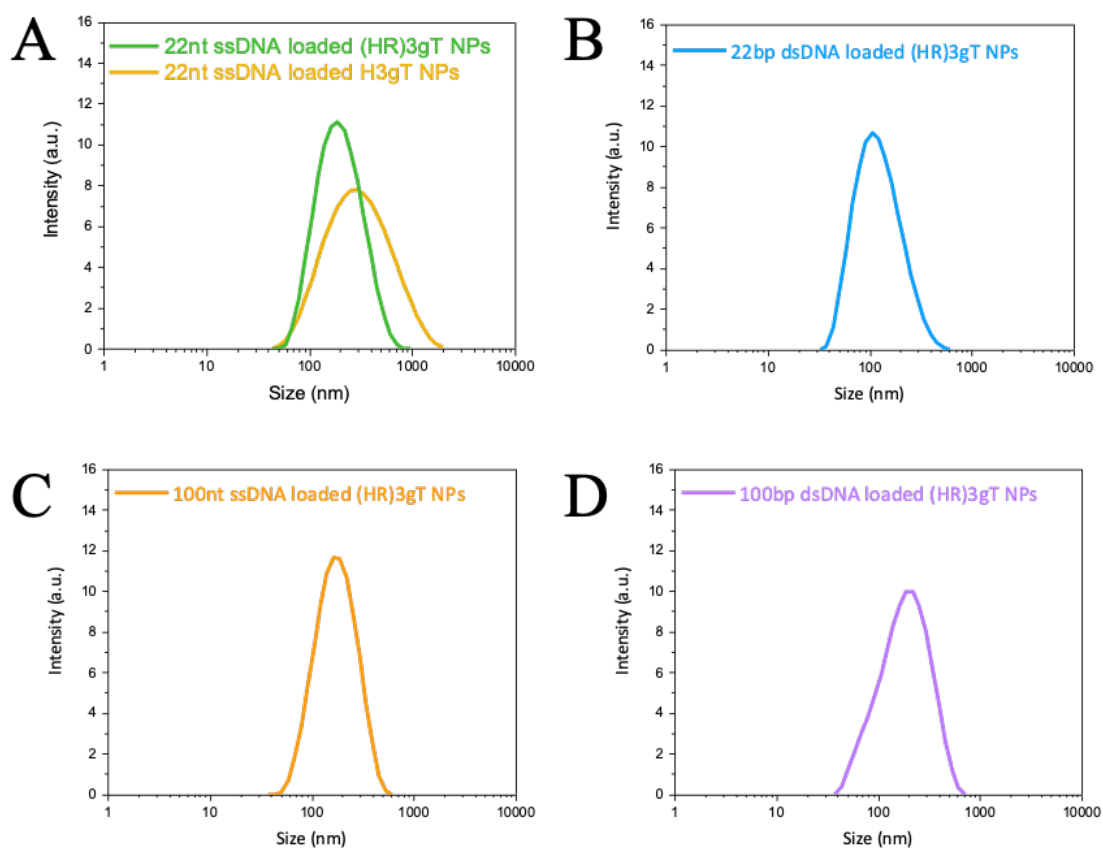


Figure 3.8: DLS of (HR)3gT MCM-NPs. (A) 22 nt ssDNA-loaded (HR)3gT compared to H3gT MCM-NPs, (B) 22 bp dsDNA-, (C) 100 nt ssDNA- and (D) 100 bp dsDNA-loaded (HR)3gT MCM-NPs.

Furthermore, increasing the length of the entrapped DNA sequence from 22 nt/bp to 100 nt/bp did not significantly affect the average size of (HR)3gT NPs. It is widely accepted that particle size plays a critical role in developing successful therapeutic delivery systems^{167,168}. For example, size is one of the most crucial determinants of nanoparticle half-life. In order to decrease the likelihood of liver or splenic trapping and increase systemic circulation time, a particle size below 200 nm is desired for *in vivo* applications of non-viral delivery systems¹⁶⁹. Thus, keeping the particle size below 200 nm independent of whether 22 nt/bp or 100 nt/bp were entrapped represents an important advance of the (HR)3gT peptide towards an efficient DNA delivery system. Moreover, as the upper size limit for a clathrin-mediated endocytosis is 200 nm^{170,171}, the characteristic average size of our newly generated DNA-loaded (HR)3gT MCM nanoparticles makes them well-suited for cellular uptake. DLS and TEM also demonstrated that (HR)3gT NPs with and without DNA do not tend to aggregate over time. This represents another advantage over H3gT peptide nanoparticles which tend to aggregate³⁷.

We employed FCS, NTA and DLS to determine the size and polydispersity index (PDI) of (HR)3gT MCM-NPs that had entrapped either single- or double-stranded DNA sequences of different lengths. A comparison of the corresponding measurements is presented in Table 3.1.

From the FCS measurements, we determined the hydrodynamic radius of NPs from Eq. (4) (see Methods) and extracted the diffusion time by solving Eq. (2), using the hydrodynamic diameter and the known diffusion coefficients of ss/dsDNA of different size¹⁷².

Table 3.1 Characterization of (HR)3gT and H3gT MCM-NPs, suspended in water, at pH 7.

MCM-NPs	PDI	D _H (DLS-nm)	D _H (FCS-nm)	D _H (NTA-nm)
H3gT NPs	0.32±0.024	211±46	NA*	236±57
(HR)3gT NPs	0.19±0.024	112±21	NA*	102±6
22nt ssDNA loaded H3gT NPs	0.34±0.027	241±73	242±12	233±29
22nt ssDNA loaded (HR)3gT NPs	0.23±0.026	160±18	144±58	151±12
22bp dsDNA loaded (HR)3gT NPs	0.22±0.023	115±19	124±62	129±10
100nt ssDNA loaded (HR)3gT NPs	0.28±0.021	176±11	186±78	164±4
100bp dsDNA loaded (HR)3gT NPs	0.27±0.02	165±12	174±99	150±11

*not applicable

A PDI \leq 0.3, which for polymer-based nanosystems implies a relatively monodisperse system, was obtained by DLS measurements of DNA-free and DNA-loaded (HR)3gT MCM-NPs^{173,174}. It is noteworthy that (HR)3gT MCM-NPs (DNA-free and DNA-loaded) had a lower PDI than corresponding H3gT MCM-NPs (**Table 3.1**). The mean diameter obtained by NTA was similar to that determined by DLS for each kind of (HR)3gT MCM-NPs (**Table 3.1**). The respective sizes were further corroborated by average sizes calculated from FCS measurements (**Table 3.1**). Indeed, FCS is a suitable method for characterizing the size of fluorescent NPs if the number of fluorescent species is \leq 3 and the particle size $<$ 500 nm¹⁷⁵. In contrast to the hydrodynamic diameters of (HR)3gT MCM-NPs loaded with different DNAs, which were all below 200 nm, H3gT MCM-NPs loaded with 22 nt ssDNA were above 200 nm in diameter (**Table 3.1**), which also limited their cellular uptake (**see below; Figure 3.15**). It has been reported that nanoparticles above 200 nm may be excluded from cellular internalization altogether^{176,177}.

3.3.4.3 Surface Charge

The surface charge of nanoparticles is known to play a key role in cellular uptake. In many instances, positively charged particles were shown to be efficiently endocytosed due to their interactions with the negatively charged cell membrane^{178,179}. As expected, in the absence of DNA, (HR)3gT MCM-NPs displayed a higher zeta potential than H3gT MCM-NPs due to the extra arginines included in the hydrophilic domain of (HR)3gT (**Table 3.2**). With a surface charge of 2.8 ± 3.35 mV, 22 nt ssDNA-loaded (HR)3gT MCM-NPs experience repulsion forces between each other that hinder their aggregation and support their stability while 22 nt ssDNA-loaded H3gT MCM-NPs are neutral (0.6 ± 2.3 mV) and thus, tend to aggregate after formation.

Table 3.2 Surface charge of (HR)3gT and H3gT MCM-NPs, suspended in water, at pH 7.

MCM-NPs	Zeta potential (mV)
H3gT NPs	3.42±3.62
(HR)3gT NPs	8.2±2.1
22nt ssDNA-loaded H3gT NPs	0.6±2.3
22nt ssDNA-loaded (HR)3gT NPs	2.8±3.35
22bp dsDNA-loaded (HR)3gT NPs	3.67±3.11
100nt ssDNA-loaded (HR)3gT NPs	3.46±3.87
100bp dsDNA-loaded (HR)3gT NPs	4.18±3.36

Moreover, to study the effect of DNA entrapment on the surface charge of MCM-NPs, the zeta potential of NPs loaded with different DNAs was measured (**Table 3.2**). With the entrapment of negatively charged DNA in self-assembling (HR)3gT, the surface charge of the resulting MCM-NPs was not significantly decreased compared to DNA-free NPs. These data support the presence of corresponding DNA payload between individual micelles of the multi-compartment rather than

its accumulation on the NP surface (**Table 3.2**) because the latter would lead to a larger decrease of the zeta potential. A positive surface charge has been shown to be advantageous for delivering DNA in a number of NP systems ¹⁸⁰. For example, PEGylated DNA/transferrin–PEI complexes bearing a positive charge of only +4 mV, were found to be the most efficient gene delivery system among other positively charged complexes ¹⁸¹. In another study on 140 distinct polymer compositions, DNA-loaded NPs bearing a charge of +1.8 mV demonstrated the third highest uptake and best overall transfection of a luciferase plasmid in NIH 3T3 cells ¹⁸². Accordingly, the overall positive charge of +2mV to +4 mV of (HR)3gT MCM-NPs loaded with different DNAs is expected to be conducive to an efficient DNA delivery. Thus, the modifications of our newly designed (HR)3gT peptide which led to MCM-NPs below 200 nm with a slightly positive surface charge, represent a crucial advance in fulfilling the physiochemical criteria required for generating successful therapeutic nanosystems.

3.3.5 Quantification of DNA Entrapment into Nanoparticles

3.3.5.1 FCS method

The incorporation of different sizes and types of DNA into (HR)3gT MCM-NPs was examined by FCS using Atto550-labeled DNAs. Diffusion time (τ_D) and count per molecule (CPM) of free Atto550 dye, Atto550-DNA in solution, and of Atto550-DNA-loaded (HR)3gT MCM-NPs were calculated by fitting the experimental autocorrelation curves (**Figure 3.9**) to a two-component fit (Eq. (1)).

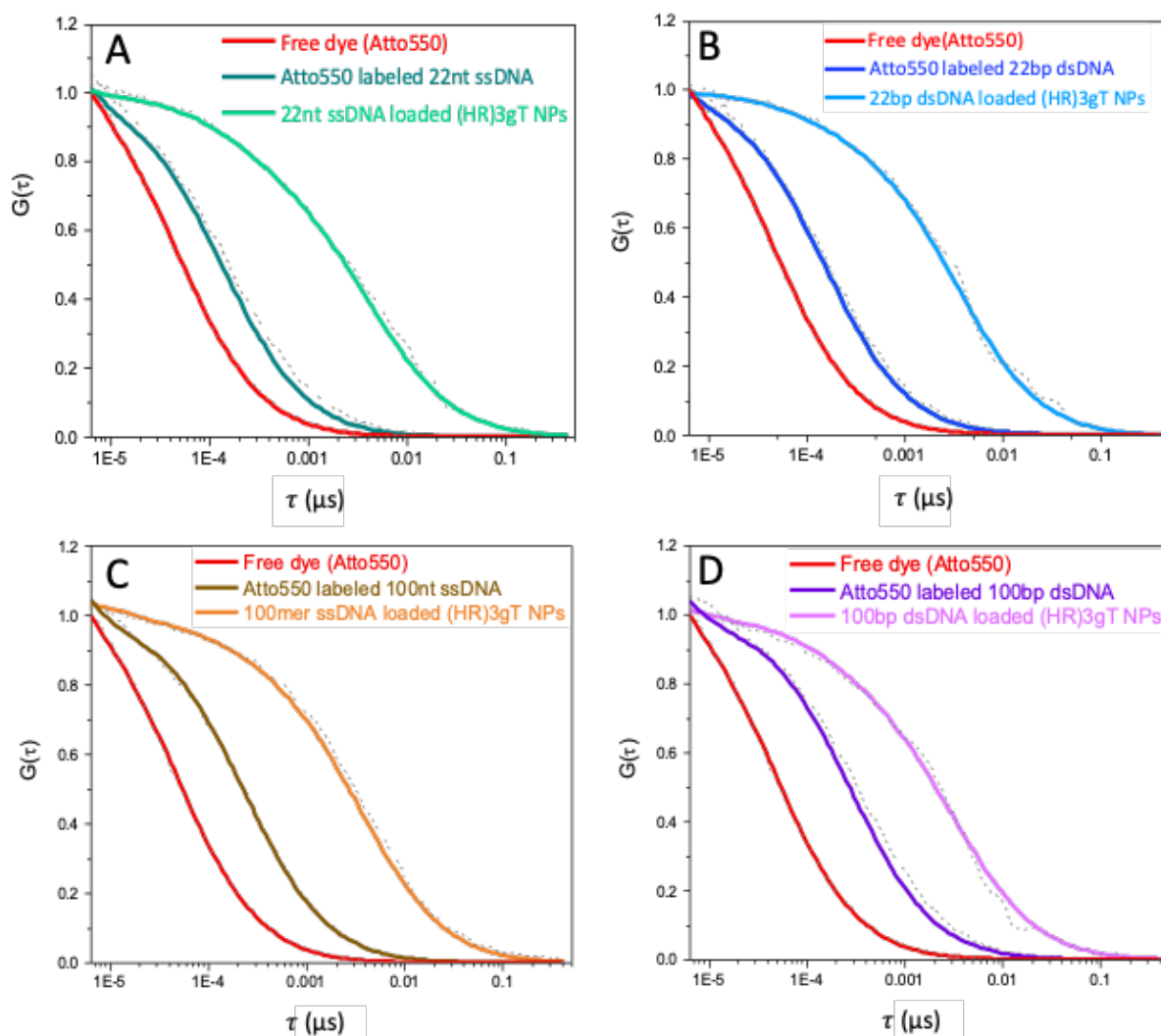


Figure 3.9: Normalized FCS autocorrelation curves showing incorporation of (A) Atto550-labeled 22 nt ssDNA in (HR)3gT MCM-NPs (light green), (B) Atto550-labeled 22 bp dsDNA in (HR)3gT MCM-NPs (light blue), (C) Atto550-labeled 100 nt ssDNA in (HR)3gT MCM-NPs (orange), (D) Atto550-labeled 100 bp dsDNA in (HR)3gT MCM-NPs (pink). Atto550 free dye is shown in red in all panels.

Subsequently, the number of DNA molecules per particle was calculated by dividing the CPM of DNA-loaded (HR)3gT MCM-NPs to the corresponding free Atto550-DNA in solution (Table 3.3). The significant increase in the diffusion time of all Atto550-DNA-loaded NPs compared to free Atto550-labeled DNA reflects that the DNA is entrapped in (HR)3gT MCM-NPs.

Table 3.3 Quantification of DNA loading in to (HR)3gT MCM-NPs by FCS.

Fluorescent species	Diffusion time (μ s)	DNA/particles
Atto550 fluorescent dye	48 \pm 3	N/A
Atto550 labeled 22nt ssDNA	139 \pm 5	N/A
Atto550-labeled 22bp dsDNA	157 \pm 9	N/A
Atto550-labeled 100bp dsDNA	283 \pm 12	N/A
22nt ssDNA-loaded H3gT NPs	5322 \pm 382	3.95 \pm 2.39
22nt ssDNA loaded (HR)3gT NPs	3894 \pm 1337	19.9 \pm 13.7
22bp dsDNA loaded (HR)3gT NPs	3235 \pm 1607	11.7 \pm 7.2
100nt ssDNA loaded (HR)3gT NPs	3875 \pm 1778	2.01 \pm 2.43
100bp dsDNA loaded (HR)3gT NPs	3553 \pm 1900	1.47 \pm 1.12

For (HR)3gT MCM-NPs, we calculated 19.9 ± 13.7 22 nt ssDNA molecules per particle while the H3gT peptide was able to entrap only 3.95 ± 2.39 22 nt ssDNA per particle. Although 22 nt ssDNA-loaded (HR)3gT MCM-NPs had entrapped five times more 22mer ssDNA than H3gT MCM-NPs, their average size is significantly smaller (160 ± 18 versus 241 ± 73 nm, **Table 3.1**, $p \leq 0.05$) (**Table 3.3**). The enhanced positive charge of (HR)3gT peptide compared to H3gT peptide results in increased electrostatic interactions between DNA and peptide and thus more compact assemblies. Consequently, the nanoparticle size remains smaller than the corresponding H3gT MCM-NPs despite more DNA and a longer peptide (19 versus 10 amino acids). For (HR)3gT MCM-NPs loaded with double-stranded 22 bp DNA, the average diffusion time of 3235 ± 1607 μ s indicated that the number of DNA molecules per particle is approximately half the number of corresponding ssDNA per particle (**Figure 3.9B** and **Table 3.2**). Considering that electrostatic interactions between DNA and peptide are responsible for the DNA entrapment during the self-assembly process, doubling the amount of negatively charged phosphates in the backbone of the

double-stranded DNA may explain why the entrapment is reduced by half. In addition, the higher rigidity of the 22 bp dsDNA may interfere with entrapment.

Likewise, for the longer DNA segments (100 nt/bp ss/dsDNA), the number of DNA molecules incorporated into (HR)3gT MCM-NPs decreased compared to both, single- and double-stranded 22 nucleotide-long DNA (**Figure 3.9C, D** and **Table 3.2**). (HR)3gT with an isoelectric point of 12.4 (versus 7.61 for H3gT) has a charge of +3 compared to 0 for H3gT at neutral pH. Because more electrostatic interactions that drive the DNA incorporation can occur, (HR)3gT is able to condense longer DNA segments (100 nt and 100 bp).

3.3.5.2 NTA method

In addition, the total concentration of particles in solution and the percentage of loaded particles were determined by nanoparticle tracking analysis (**Table 3.4**).

Table 3.4 Nanoparticle tracking analysis of DNA-free and DNA-loaded (HR)3gT MCM-NPs.

MCM peptide NPs	Total concentration (particles/ml)	Concentration of labeled particles (particles/ml)	Loaded particles (%)
22nt ssDNA loaded (HR)3gT NPs	$5.57 \text{ e}+08 \pm 7.03\text{e}+07$	$3.82 \text{ e}+08 \pm 2.29\text{e}+07$	68.5
22bp dsDNA loaded (HR)3gT NPs	$3.02 \text{ e}+08 \pm 3.06\text{e}+07$	$2.87 \text{ e}+08 \pm 3.10\text{e}+07$	95
100nt ssDNA loaded (HR)3gT NPs	$3.29 \text{ e}+08 \pm 7.65\text{e}+07$	$2.25 \text{ e}+08 \pm 1.10\text{e}+07$	68.3
100bp dsDNA loaded (HR)3gT NPs	$3.34 \text{ e}+08 \pm 8.64\text{e}+07$	$2.74 \text{ e}+08 \pm 1.52\text{e}+07$	82

The concentration of MCM-NPs formed in the presence of 100 nt long sequences was similar for single- and double-stranded DNA ($3.29 \times 10^8 \pm 7.65 \times 10^7 \text{ mL}^{-1}$ and $3.34 \times 10^8 \pm 8.64 \times 10^7 \text{ mL}^{-1}$, respectively), and comparable to that of NPs assembled in the presence of 22 bp dsDNA ($3.02 \times 10^8 \pm 3.06 \times 10^7 \text{ mL}^{-1}$). Significantly higher numbers of MCM-NPs ($5.57 \times 10^8 \pm 7.03 \times 10^7$) were obtained when (HR)3gT was assembled with 22 nt ssDNA. For all types of DNA,

more than 60% of the MCM-NPs were loaded with DNA whereby the percentage of loaded particles for dsDNA (22 bp and 100 bp) was clearly higher than for ssDNA (22 nt and 100 nt). Considering the FCS data presented above, which show that (HR)3gT MCM-NP entrap approximately twice as many ssDNA as dsDNA molecules, the overall amount of loaded DNA is higher for ssDNA compared to dsDNA MCM-NPs. Thus, while the total concentration of particles is similar for 100 nt ssDNA and 100 bp dsDNA MCM-NPs, the overall amount of entrapped DNA is higher with single-stranded than with double-stranded DNA despite the lower percentage of loaded particles (68.5% versus 82%). Similarly, the percentage of loaded particles for the 22 nt long DNA was 68.5% for ssDNA versus 95% for dsDNA ($3.82 \times 10^8 \pm 2.29 \times 10^7$ versus $2.87 \times 10^8 \pm 3.10 \times 10^7$). Due to the significantly higher concentration of MCM-NPs that self-assemble in the presence of 22 nt ssDNA, the difference in the amount of entrapped DNA between single- and double stranded is higher for 22 nucleotide long DNA sequences than for 100 nucleotide sequences.

In conclusion, the modifications of the (HR)3gT peptide, in particular the enhanced positive charge over H3gT, conveys not only the ability to entrap longer single- and double-stranded DNA upon nanoparticles but also the potential to more efficiently incorporate higher amounts of 22 nt ssDNA. Generating (HR)3gT MCM-NPs with improved DNA loading and smaller particle size compared to H3gT represents a significant progress towards developing an efficient and functional DNA delivery system.

3.3.6 Stability of Peptide Nanoparticles

To obtain insight on the stability of DNA-free and DNA-loaded (HR)3gT NPs, we analyzed the size of NPs stored at 4 °C by DLS over time (**Figure 3.10A**).

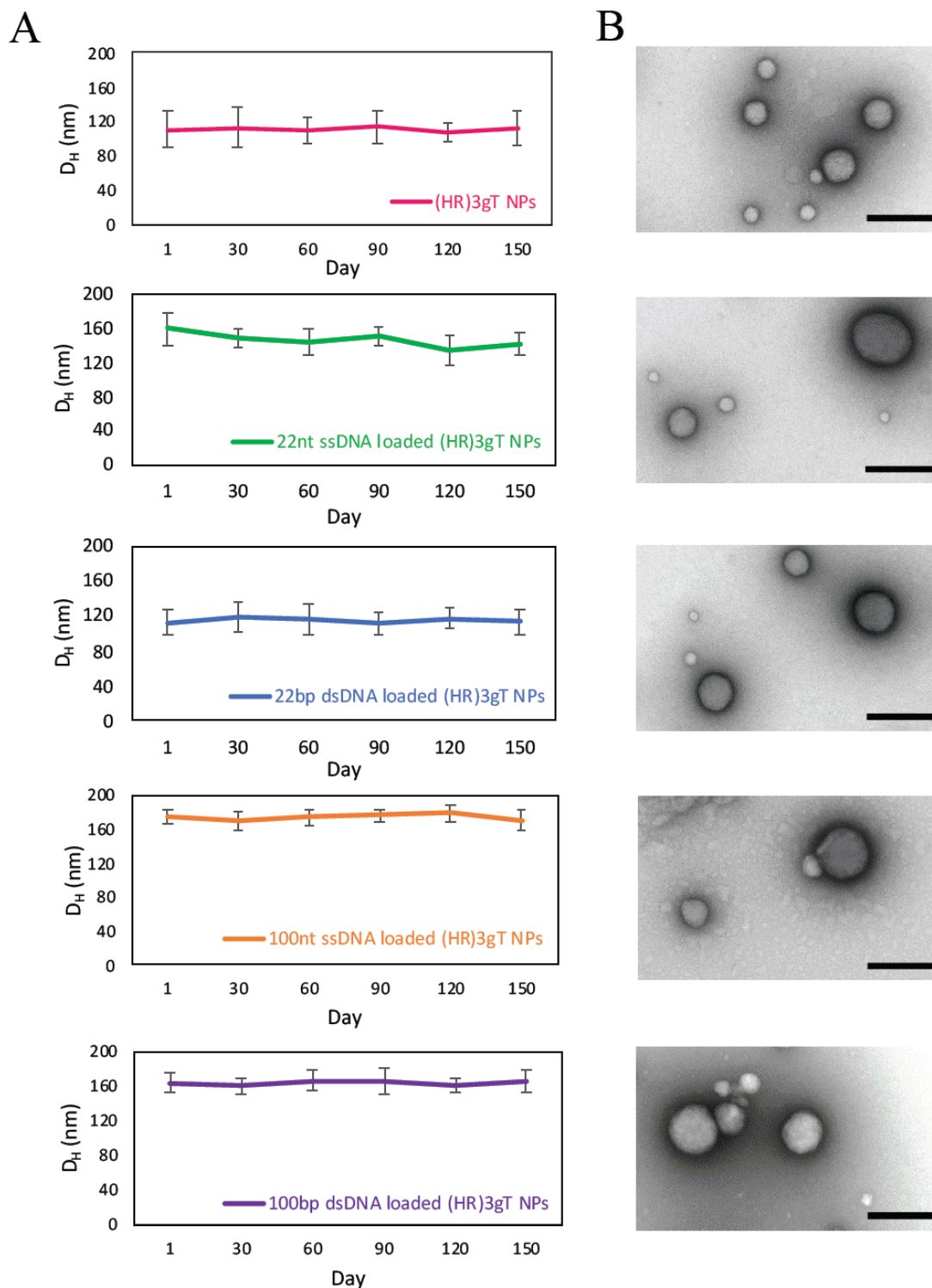


Figure 3.10: Stability of (HR)3gT MCM-NPs at 4°C. From top to bottom: (A) D_H by DLS over 150 days, (B) Corresponding TEM after 150 days for (HR)3gT MCM-NPs, 22 nt ssDNA-loaded (HR)3gT MCM-NPs, 22 bp dsDNA-loaded (HR)3gT MCM-NPs, 100 nt ssDNA-loaded (HR)3gT MCM-NPs, and 100 bp dsDNA-loaded (HR)3gT MCM-NPs. Scale bars = 200 nm.

Nanoparticle size measurements recorded every 30 days indicated that the average hydrodynamic diameter of DNA-free and DNA-loaded (HR)3gT MCM-NPs did not change over five months. TEM analyses of empty and DNA-loaded (HR)3gT MCM-NPs after 5 months (**Figure 3.10B**) showed that nanoparticles retained their initial multi-compartment micellar architecture. In contrast, H3gtT MCM-NPs, especially when loaded with 22 nt ssDNA, aggregated due to their neutral surface charge ³⁷.

3.3.7 Thermo-responsiveness of Peptide Nanoparticles

To assess thermo-responsiveness, DNA-free and DNA-loaded (HR)3gT MCM-NPs were incubated at 37 °C for 5 h and 24 h. Ultrastructural analysis by TEM revealed that compared to the MCM structure of NPs at 4 °C, (HR)3gT MCM-NPs disassembled into smaller MCMs and/or individual micelles after 5 h at 37 °C (**Figure 3.11A**). The tendency to disassembly increased over time and after 24 h at 37 °C (**Figure 3.11B**), only few MCM-NPs were detected.

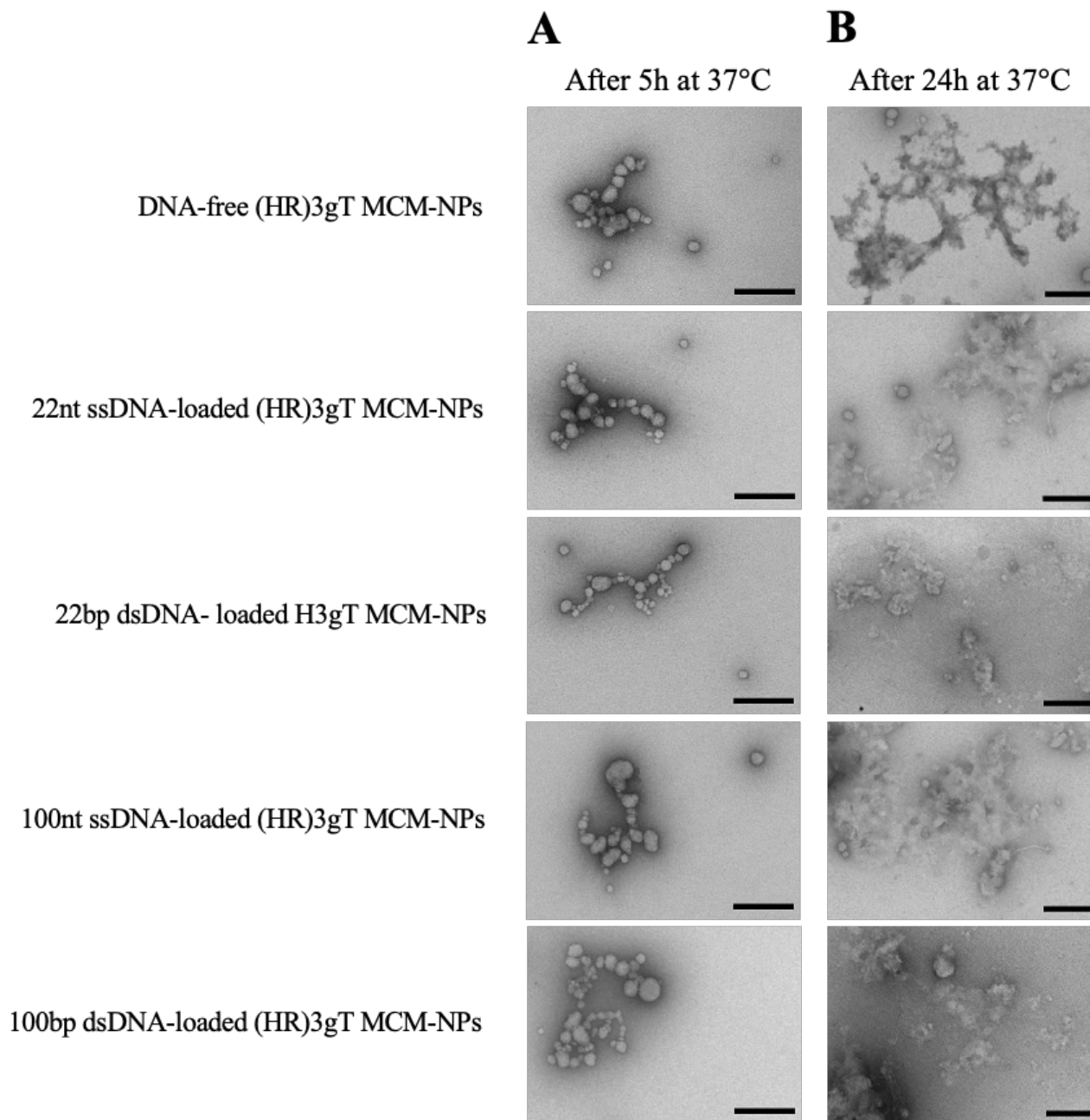


Figure 3.11: TEM micrographs of (HR)3gT MCM-NPs with different DNA loads after (A) 5 h incubation, and (B) 24 h incubation at 37°C. Scale bars = 200 nm.

When kept at 37 °C, all peptide MCM-NPs exhibited a similar trend in the change of their structure and size, independent of the length and type (single or double stranded) of the entrapped

DNA, whereas at 4 °C, (HR)3gT MCM-NPs remained stable for as long as 5 months (**Figure 3.10**). Likewise, H3gT MCM-NPs demonstrated a similar disassembly behaviour in response to temperature (**Figure 3.12**). Our data are consistent with the study by Schuster et al. who reported that the formation of MCM peptide NPs occurs as a function of temperature and solvent composition ³⁵.

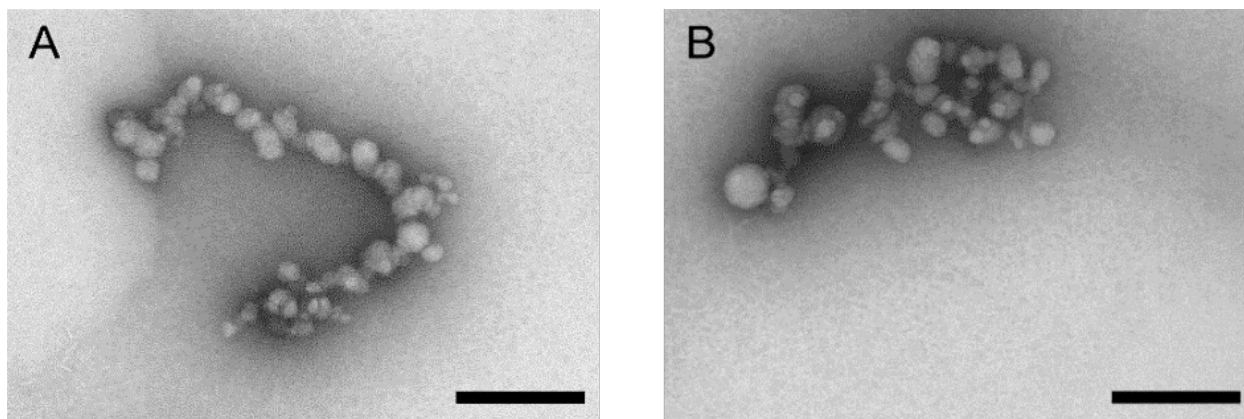


Figure 3.12: TEM micrograph of (A) H3gT NPs, and (B) 22nt ssDNA-loaded H3gT NPs after 5h incubation at 37°C. Scale bars=200nm.

3.3.8 Effect of Peptide Nanoparticles on Cell Proliferation

In order to assess the cytotoxicity of our non-viral DNA delivery system, MTS cell proliferation assays with HeLa cells and different concentrations of DNA-loaded and DNA-free (HR)3gT MCM-NPs (up to 1550 $\mu\text{g mL}^{-1}$) were performed (**Figure 3.13A**).

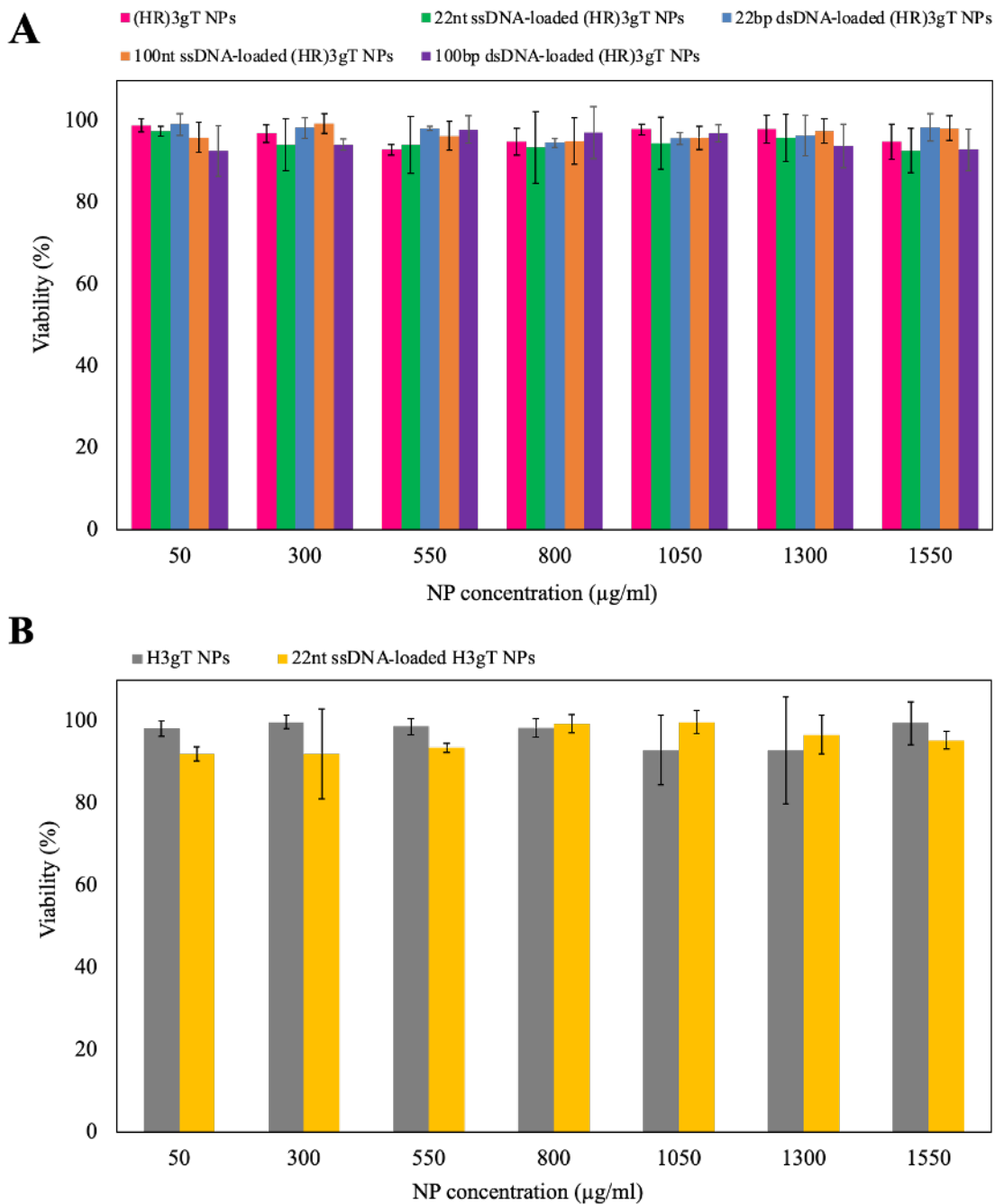


Figure 3.13: HeLa cell viability (MTS assays). Cells treated for 24 h with (HR)3gT MCM-NPs (pink), 22 nt ssDNA-loaded (HR)3gT MCM-NPs (green), 22 bp dsDNA-loaded H3gT MCM-NPs (blue), 100 nt ssDNA-loaded (HR)3gT MCM-NPs (orange), 100 bp dsDNA-loaded (HR)3gT MCM-NPs (purple). Cell viability was normalized to untreated HeLa cells (negative control, 100% viability). All data presented as the mean \pm SD (n = 3).

The data showed that after 24 h of incubation at 37 °C, DNA-loaded and DNA-free (HR)3gT MCM-NPs up to a concentration of 1550 $\mu\text{g mL}^{-1}$ had no toxic effects on HeLa cells. It is noteworthy that 22 nt ssDNA-loaded (HR)3gT MCM-NPs had no significant inhibitory effect on cell proliferation even though they are loaded with a 5-times higher amount of 22 nt ssDNA compared to corresponding H3gT MCM-NPs (**Figure 3.13B**) These findings suggest that the viability of cells remains largely unaffected not only by the MCM-NP concentration but also by the amount of entrapped DNA. Based on the apparent biocompatibility, (HR)3gT MCM-NPs are a viable candidate for a further development of a safe gene delivery systems.

3.3.9 Cell Uptake of Peptide Nanoparticles

The cellular uptake of peptide MCM-NPs loaded with different fluorescently labeled Atto550-DNA was examined in H2B-GFP expressing HeLa cells by confocal laser scanning microscopy (CLSM). Before evaluating the ability of (HR)3gT NPs to mediate cellular uptake of DNA and thus find out about potential of this gene delivery system, we studied the cellular uptake of free Atto550-labeled single- and double-stranded 22 and 100 nucleotide sequences as a control (**Figure 3.14**).

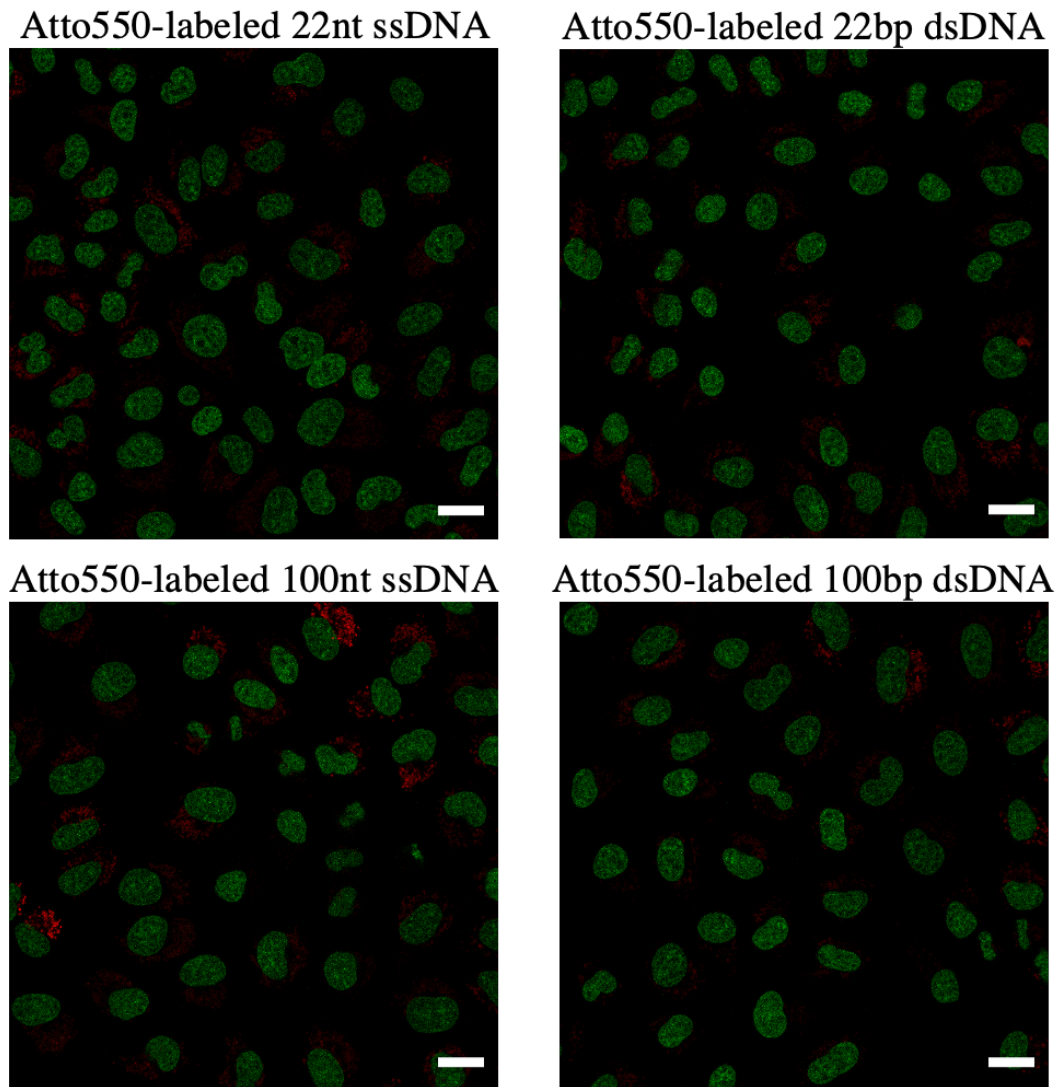


Figure 3.14: CLSM merged images (GFP and Atto550) of H2B-GFP expressing HeLa cells treated with free Atto550-labeled DNAs. Images are recorded under the same conditions as in Figure 3.15. Scale bars = 20 μ m.

Then we compared cells that were treated with 22 nt ssDNA-loaded (HR)3gT or H3gT MCM-NPs (**Figure 3.15**). Confocal images of cells incubated with NPs for 24 h revealed that at similar cell density, a significantly higher number of cells had taken up 22 nt ssDNA-loaded (HR)3gT MCM-NPs.

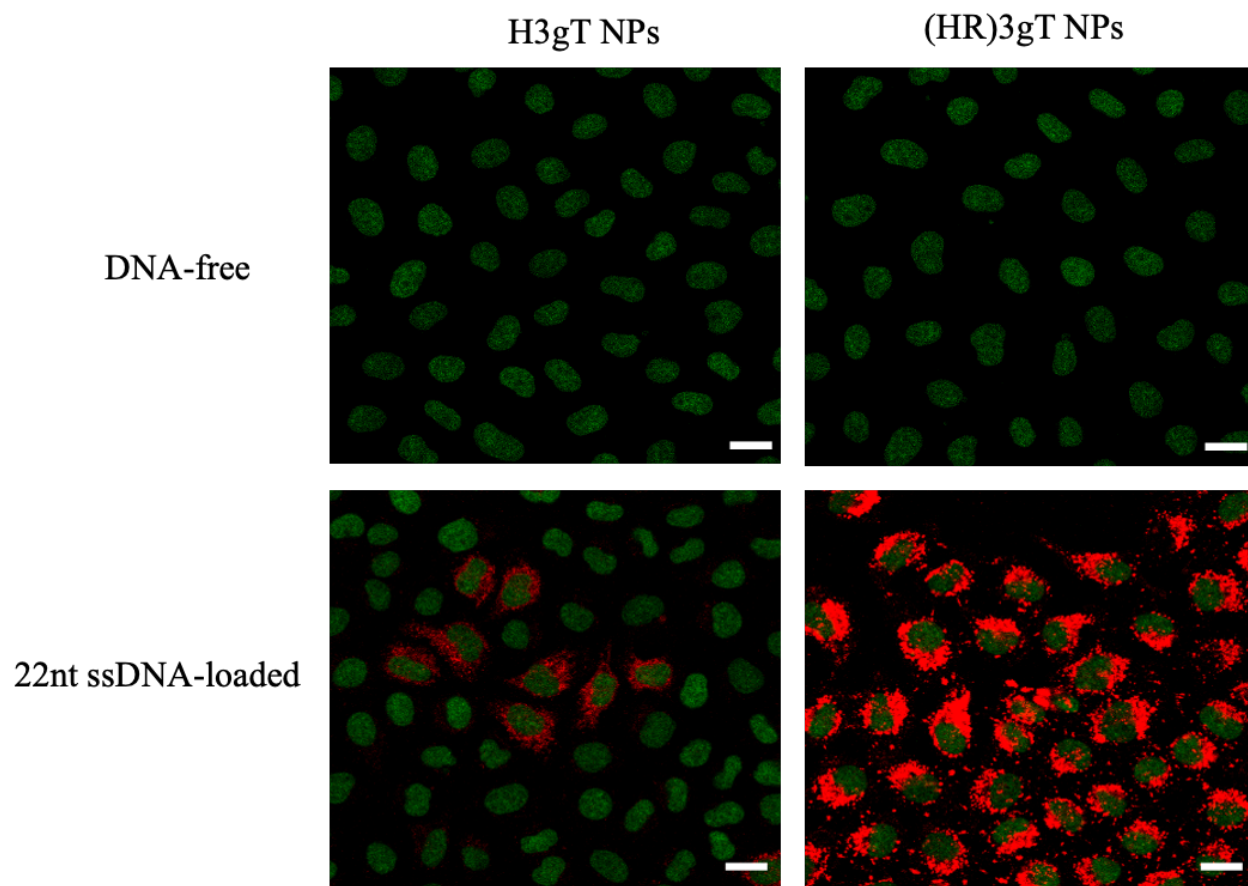


Figure 3.15: CLSM merged images (GFP and Atto550) of H2B-GFP expressing HeLa cells treated with Atto550-22nt ssDNA-loaded H3gT (*left*) and (HR)3gT MCM-NPs (*right*) for 24h. Scale bars = 20 μ m.

Besides the higher rate of uptake, the fluorescence signal in cells that had taken up 22nt ssDNA-loaded (HR)3gT MCM-NPs was considerably stronger than in cells containing H3gT MCM-NPs under identical imaging conditions. Also, after 48 h of NP incubation, the uptake efficiency for 22 nt ssDNA-loaded (HR)3gT was higher than for H3gT MCM-NPs (**Figure 3.16**).

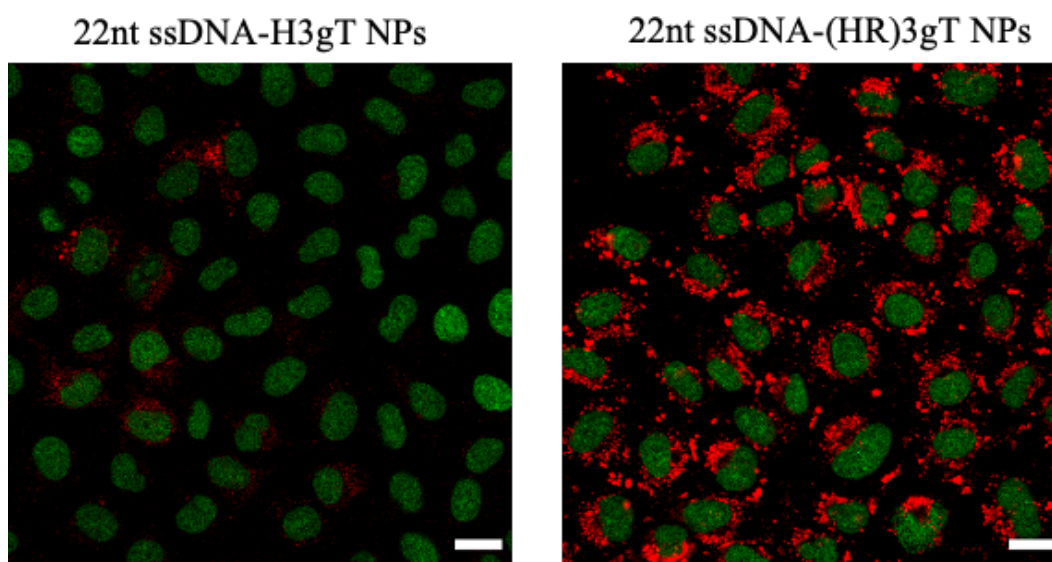


Figure 3.16: CLSM merged images (GFP and Atto550) of H2B-GFP expressing HeLa cells treated with Atto550-22nt ssDNA-loaded H3gT and (HR)3gT MCM NPs for 48h. Scale bars = 20 μ m.

Several properties of NPs assembled from the newly designed (HR)3gT peptide could account for the higher uptake efficiency of 22 nt ssDNA-loaded (HR)3gT MCM-NPs versus 22 nt ssDNA-loaded H3gT MCM-NPs. Nanoparticle size, shape, surface charge, and surface functionality are known to affect cellular uptake^{182,183}. Based on literature reports, the optimal size for NP uptake, especially in cancer treatment, is between 70–200 nm and ideally close to 100 nm. However, for specific applications, slightly larger particle sizes may be more advantageous^{184–188}. Accordingly, the mean diameter of 22 nt ssDNA-loaded (HR)3gT MCM-NPs (160 ± 18 nm) is in an optimal range promoting uptake whereas on average, 22 nt ssDNA-loaded H3gT MCM-NPs (241 ± 73 nm) are big for efficient uptake. Furthermore, the increased cellular uptake could be facilitated by other internalization mechanisms because of the arginine–histidine repeating units that are exposed on the hydrophilic surface of the (HR)3gT MCM-NPs. Numerous studies report that arginine residues promote cell penetration and increase internalization efficiency in the

delivery of therapeutic macromolecules, in particular nucleic acids ^{189–196}. For example, using a multifunctional envelope-type nanodevice (MEND) that comprises an octa-arginine as gene delivery system resulted in a 300-fold improvement in gene expression compared to unmodified MEND ¹⁹⁷. Besides a larger number of nanoparticles taken up per cell, the 5 times higher amount of 22 nt ssDNA loaded per particle compared to H3gT MCM-NPs also contribute to the increased fluorescence intensity.

Cellular uptake assays with (HR)3gT MCM-NPs loaded with 22bp dsDNA and longer sequences (100nt/bp) revealed a similarly high uptake efficiency for all (HR)3gT MCM-NPs (**Figure 3.17**).

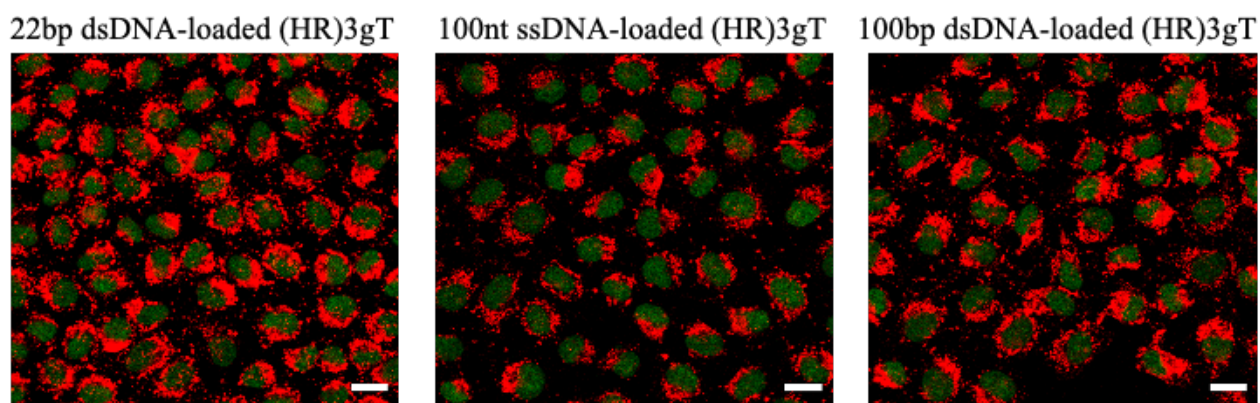


Figure 3.17: CLSM merged images (GFP and Atto550) of H2B-GFP expressing HeLa cells treated with Atto550-22bp and 100nt/bp ss/dsDNA-loaded (HR)3gT NPs after 24h. Imaging conditions were as in Fig. 3.16. Scale bars = 20 μ m.

As previously mentioned, the number of incorporated dsDNA molecules/particle is approximately half compared to the number of ssDNA molecules in corresponding (HR)3gT MCM-NPs. Thus, under identical imaging conditions, one can expect a lower fluorescence signal for dsDNA-loaded peptide NP uptake. However, CLSM images showed no significant difference between 22bp dsDNA and 22mer ssDNA-loaded (HR)3gT MCM-NPs (compare **Figure 3.17** and

3.15), and between 100bp dsDNA and 100mer ssDNA-loaded MCM-NPs (**Figure 3.17**). It is possible that small differences in size and surface charge between MCM-NPs loaded with dsDNA versus ssDNA (see **Table 3.1**) lead to an increase in cellular uptake and thus, account for the greater fluorescence signal. Furthermore, a time-dependent increase of intracellular fluorescence from 1 to 13 h for 100bp dsDNA-loaded (HR)3gT MCM-NPs is shown in Figure 3.18.

As previously mentioned, the number of incorporated dsDNA molecules/particle is approximately half compared to the number of ssDNA molecules in corresponding (HR)3gT MCM-NPs. Thus, under identical imaging conditions, one can expect a lower fluorescence signal for dsDNA-loaded peptide NP uptake. However, CLSM images showed no significant difference between 22bp dsDNA and 22mer ssDNA-loaded (HR)3gT MCM-NPs (compare **Figure 3.17** and **3.15**), and between 100bp dsDNA and 100mer ssDNA-loaded MCM-NPs (**Figure 3.17**). It is possible that small differences in size and surface charge between MCM-NPs loaded with dsDNA versus ssDNA (see **Table 3.1**) lead to an increase in cellular uptake and thus, account for the greater fluorescence signal. Furthermore, a time-dependent increase of intracellular fluorescence from 1 to 13 h for 100bp dsDNA-loaded (HR)3gT MCM-NPs is shown in Figure 3.18.

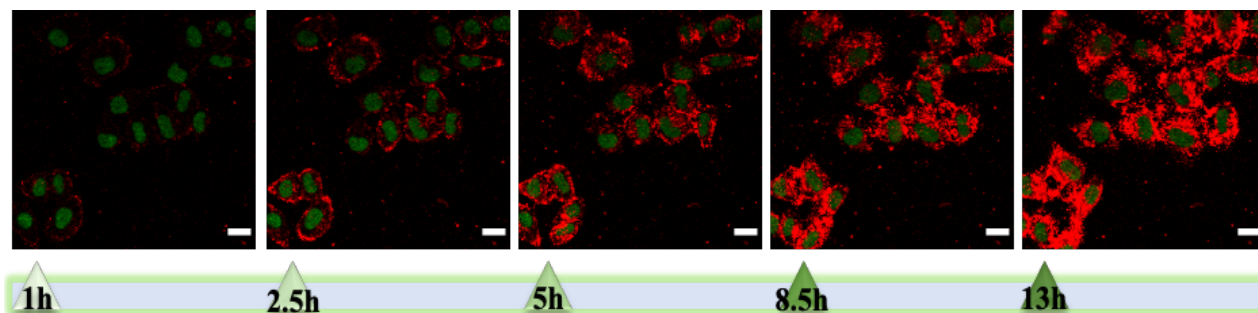


Figure 3.18: Time course of Atto550-100bp dsDNA-loaded (HR)3gT MCM NP uptake. Scale bars = 20 μ m.

Although *in vitro* analysis of thermo-responsiveness showed a disassembly of MCM-NPs after 5h, earlier time points, i.e., 1 and 2 h, revealed that the multicompartiment micellar architecture of 100bp dsDNA-loaded (HR)3gT NPs was still intact (**Figure 3.19A**). Moreover, the analysis of cells incubated with dsDNA-loaded (HR)3gT NPs showed that uptake occurred within an hour (**Figure 3.19B**) which suggests that at least some of the MCM-NPs are taken up before disassembly. Conceivably, the time-course of MCM-NP thermo-responsiveness adds to the release of DNA inside the cell.

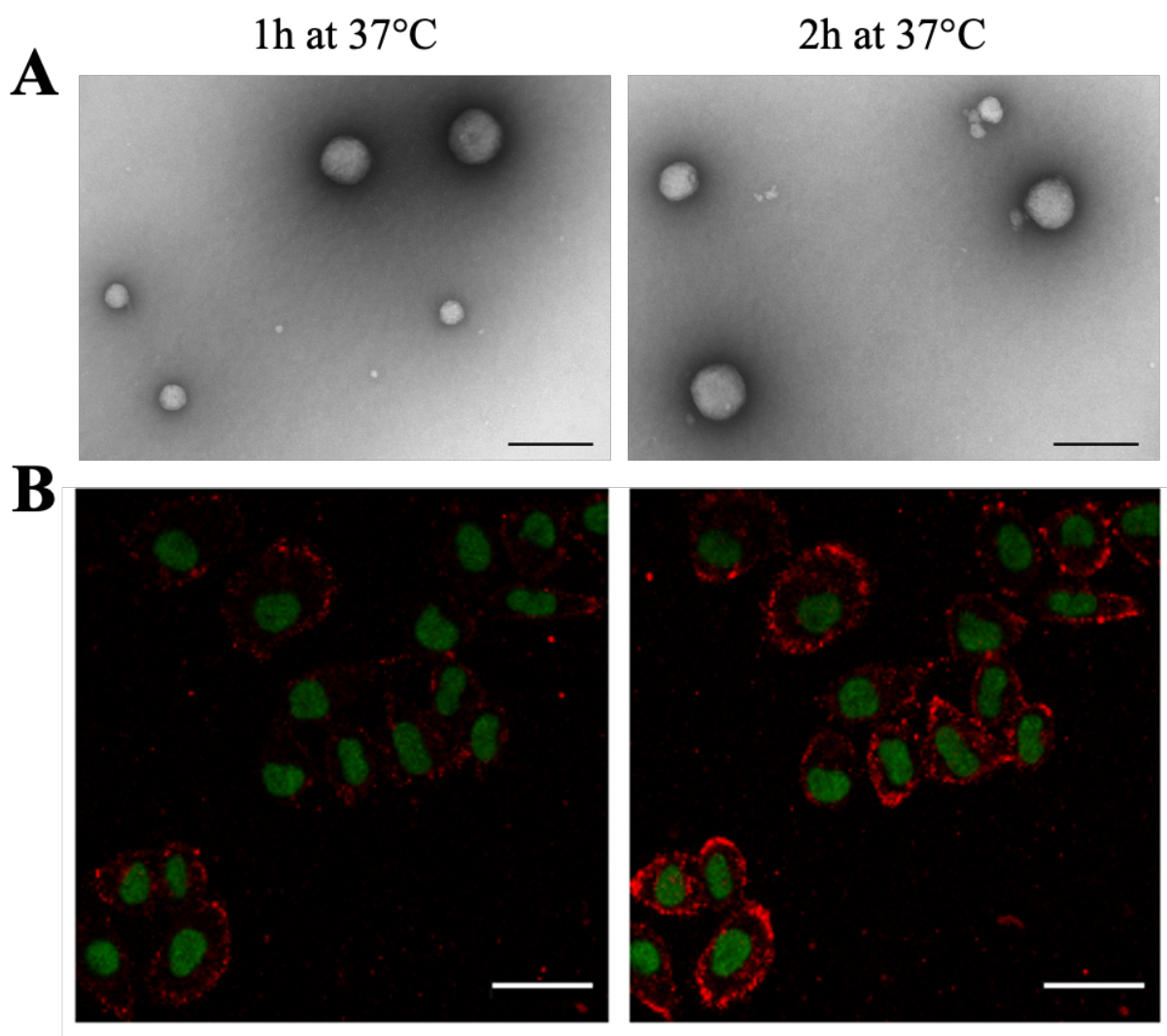


Figure 3.19: (A) TEM images of 100bp dsDNA-loaded (HR)3gT MCM-NPs after 1h (*left*) and 2h (*right*) incubation at 37°C. Scale bars = 200nm. (B) CLSM merged images (GFP and Atto550) of H2B-GFP incubation at 37°C.

expressing HeLa cells treated with 100bp dsDNA-loaded (HR)3gT MCM NPs for 1h (*left*) and 2h (*right*). Scale bars = 40 μ m.

Our data suggest that the type of the DNA sequence (i.e., single-stranded or double-stranded) and the length (22 or 100 nucleotides) affect the assembly of MCM-NPs and consequently their cellular uptake properties. Thus, to ultimately achieve a safe and efficient delivery system for protein encoding genes, the size of the DNA will need to be successively increased and tested for its effects on the self-assembly behavior of the (HR)3gT peptide. It is possible that further modifications of the peptide design might be necessary to accommodate for longer DNA sequences.

3.4 Conclusion

In this study, we addressed the challenge of developing an efficient and safe non-viral delivery system for DNA sequences larger than the average antisense oligonucleotide. Specifically, we established for the first time a purely peptidic self-assembling MCM-NP that is able to entrap single- and double-stranded DNA of 100 nucleotides/base pairs. We rationally designed and synthesized the amphiphilic (HR)3gT peptide where we significantly modified a short H3gT peptide by (i) increasing the charge of the hydrophilic domain and (ii) extending the hydrophobic domain to achieve a ratio that typically leads to the self-assembly of micellar nanostructures. The comprehensive analysis of the physicochemical characteristics of (HR)3gT MCM-NPs in the presence of different DNA cargoes indicates that the entrapment is primarily governed by electrostatic interactions between DNA and peptide, and the solvent conditions used for self-assembly. Based on the amino acid modifications, (HR)3gT peptide was able to entrap single- and double-stranded DNA sequences of 100 nucleotides whereas the short H3gT MCM-NPs could only entrap 22 nt ssDNA. A thermodynamically stable system was obtained, in which

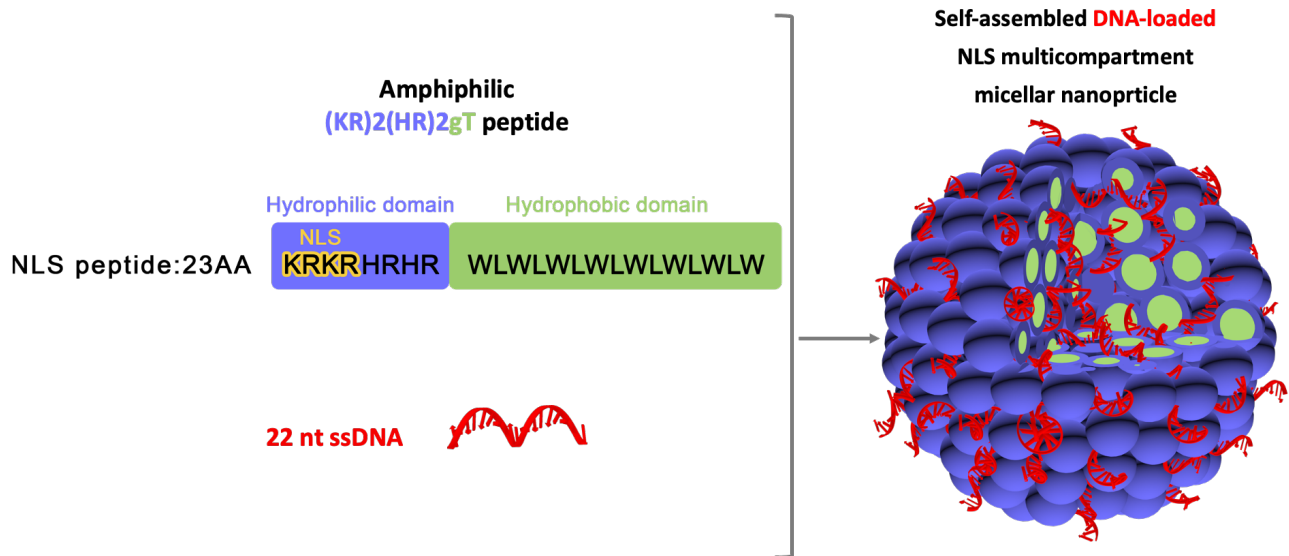
the sum of different factors including chain stretching, interfacial tension, and repulsive interactions between hydrophilic domains, especially in the presence of negatively charged DNA are minimized. Moreover, the addition of arginine residues facilitated the crossing of biological barriers which points to a great potential of (HR)3gT MCM-NPs for non-viral gene-delivery applications. (HR)3gT MCM-NPs with different DNA loads maintained a stable size and multi-compartment micellar structure over five months at 4 °C, but disintegrated into smaller MCMs and/or individual micelles at 37 °C. The thermo-responsiveness, together with the low cell toxicity and rapid cellular uptake constitute essential features in the efficient delivery of the entrapped DNA. In addition, the possibility of chemical modification by variation of the amino acid sequence and composition renders peptide nanoparticles easily tunable compared to lipid nanoparticles. Taking into account these advantages, our (HR)3gT non-viral DNA delivery system provides the first stepping stone towards developing a purely peptide-based self-assembling nanostructure for the delivery of entire genes. Future designs will need to address several parameters, for example nuclear targeting, to optimize the delivery efficiency of peptidic MCM-NPs for medical applications.

4 Self-Assembled Peptide Nanoparticles Targeting DNA to the Nucleus³

The nucleus controls DNA replication and RNA transcription processes which makes it a prominent functional target in gene therapy ¹⁹⁸. In order to treat diseases associated with genetic disorders, therapeutic DNA must be delivered to the cell nucleus. Being negatively charged, DNA by itself cannot easily cross cellular membranes without an appropriate delivery system ¹⁹⁹. Accordingly, considerable research efforts have been directed toward tailoring non-viral gene delivery systems to overcome these barriers, in particular the plasma and nuclear membrane ^{200,201}. Nevertheless, the transport of non-viral delivery systems to the nucleus is considered to be a rate-limiting step in the gene delivery process and thus remains a major challenge ¹⁰².

Limitless combinations of amino acid sequences and diverse secondary structures in peptides offer many options for targeted delivery and enhanced internalization approaches ^{202,203}. Peptides can potentially overcome biological barriers by targeting cell-surface receptors, membrane disruption or nuclear import ²⁰⁴. In particular, targeting of non-viral delivery systems by a nuclear localization sequence (NLS), typically one or more short sequences of positively charged lysines or arginines, is a widely exploited strategy for achieving selective nuclear delivery ²⁰⁵. To combine the advantages of vector properties offered by peptides with utilizing NLS-mediated targeting, we designed a novel peptide aimed to self-assemble into a nanocarrier that promotes the translocation of oligonucleotides into the nucleus.

³ A publication based on the data discussed in this chapter is Submitted: **S. Tarvirdipour**, M. Skowicki, C. A. Schoenenberger, L. Kapinos, R. Y. H. Lim, K. Benenson, C. G. Palivan, (2022), Submitted.



4.1 Abstract

Gene delivery systems encounter several cellular barriers on their way to successful gene therapy. Once inside the cell, non-viral vectors have to overcome the nuclear membrane to finally deliver DNA to the nucleus. To take this hurdle, we developed a novel nuclear targeting vector based on the self-assembly of an amphiphilic peptide comprising a nuclear localization signal (NLS). The NLS-peptide was produced by introducing KRKR residues at the amino-terminus of the hydrophilic domain of (HR)3gT peptide. While the NLS functionality of KRKR has been established, to the best of our knowledge, it has not been exploited for the nuclear targeting of nanoparticles so far. In order to promote self-assembly of the NLS-peptide into multi-compartment micelles (MCMs), the weight ratio of the hydrophilic to hydrophobic domain was kept similar to that of the precursor peptide (HR)3gT. Self-assembled ordered nanostructures of NLS-peptide were prepared by rapid and scalable solvent exchange method. Electrostatic interactions between negatively charged DNA cargoes and the positively charged NLS-peptides led to DNA entrapment in MCMs. The initial average size of NLS-MCMs was 90nm, but was reduced after 24h incubation at 37°C which further facilitated their nuclear translocation. Similar to (HR)3gT MCMs, NLS-

MCMs did not affect the viability of HeLa cells. However, detailed chemical, biophysical, cellular and ultrastructural analyses demonstrated that NLS-MCMs have higher cellular and nuclear uptake efficiency than (HR)3gT MCMs lacking an NLS. Statistical analysis confirmed that NLS-MCMs successfully enter the cell nucleus through the nuclear pore complex. Our findings highlight the propensity of this unique, purely peptidic nanovector to efficiently entrap and deliver oligonucleotides directly into the cell nuclei.

4.2 Introduction

The nucleus is key to all diseases derived from gene mutations, e.g. neurodegenerative diseases, heart dysfunction and muscular dystrophy, both at the level of transcription regulation and/or RNA processing ²⁰⁶⁻²⁰⁸. The importance of delivering genetic material into the nucleus for the purpose of treating human diseases gave rise to advanced non-viral delivery systems ²⁰⁹⁻²¹¹. However, non-specific uptake, insufficient targeting, inability to escape endosomes, and inefficient nuclear delivery of non-viral delivery systems limit their applications ²¹². To overcome cellular barriers and translocate therapeutic DNA to the site of action, substantial attempts have been directed toward specific engineering non-viral delivery systems ^{201,213}.

Nuclear pore complexes (NPCs) represent the only selective gateway to and from the nucleus. Generally, molecules smaller than 40-60 kDa passively diffuse through the NPC to the nucleoplasm while larger molecules require sorting signals termed nuclear localization signals (NLS) for nuclear import ¹⁹⁸. NLS are usually short stretches of amino acids recognized by nucleocytoplasmic transporters (karyopherins or kaps) that promote active transport of proteins into the nucleus ²¹⁴.

The NPC is a large proteinaceous structure composed of about 30 different proteins termed nucleoporins (Nups), of which about one third contain numerous phenylalanine-glycine (FG)-

repeat motifs. These FG-Nups are subdivided into cytoplasmic, nucleoplasmic and symmetric subtypes. The FG-repeat regions of the symmetric Nups face the NPC central channel where they are thought to form a network of filaments that presumably forms the permeability barrier of the NPC ²¹⁵.

Nuclear targeting and efficient translocation through the NPC mediated by NLS involves complex formation with karyopherins, predominantly kap β and kap α ²⁰⁹. Kap β 1 makes multivalent binding interactions with FG Nups while establishing a heterodimer with a Kap α which in turn, acts as import receptor for NLS ²¹⁶. Once the ternary import complex importin β/α /NLS interact with the FG-repeats of Nups, nuclear transport occurs in a RanGTP-regulated manner ²¹⁷.

Taking advantage of peptides, alone or as components of hybrid materials, is a widely utilized strategy to increase transfection efficiency of non-viral delivery systems ^{218,219}. Almost all attempts to specifically improve nuclear entry of DNA using non-viral vectors involve NLS peptide motifs ²⁰⁰. Four basic residues (KRKR), which are found in many NLS sequences, play a crucial role in nuclear targeting and possibly act as a monopartite NLS motif ^{220–222}. Notably, the optimal consensus patterns required for high-affinity binding to import receptors were found to be KR(K/R)R and K(K/R)RK ¹²⁹. Several pieces of evidence indicate that KRKR by itself is an authentic NLS ^{223–225}.

Here we set out to develop a novel, targeted nanoassembly made of pure peptides that is able to deliver DNA to the nucleus. In the design of the amphiphilic (KR)₂(HR)₂(WL)₇W peptide we considered that it should (i) comprise a nuclear targeting moiety, (ii) condense nucleic acids via electrostatic interactions and (iii) self-assemble into multi-compartment micelles (MCMs). To favour self-assembly, the hydrophobic to hydrophilic weight ratio of the peptide was kept similar

to our recently published (HR)3gT peptide which forms multi-compartment micelles (MCMs)¹⁴¹. Because this is the first time a purely peptidic nano-vector is functionalized with the minimal, classical NLS via the extension of the hydrophilic domain with KRKR residues, the morphology and physicochemical properties of the self-assembly structures were systemically investigated. In particular, we examined the incorporation of oligonucleotides into the nanoassemblies and the *in vitro* interactions of the DNA-loaded nanoassemblies with components of the nuclear translocation machinery. To resolve the nuclear targeting ability of self-assembled NLS-MCMs, biophysical, ultrastructural, and cellular studies with statistical analysis of DNA delivery to the nucleus were carried out and compared to corresponding MCMs lacking an NLS. Our study revealed that owing to the intrinsic targeting properties, in addition to the propensity for self-assembly and efficient DNA entrapment of the peptide, our NLS-MCMs represent an excellent DNA delivery system with little cell toxicity but great power in overcoming biological barriers, resulting in an enhanced cellular uptake and nuclear localization. Our findings unveil the purely peptide-based nano-vector as a promising candidate for nuclear-targeted gene delivery applications.

4.3 Results and Discussion

4.3.1 Design, Synthesis and Self-Assembly of Peptide Amphiphiles

Despite an increasing number of non-viral delivery systems, strategies tackling intracellular targeting, in particular targeting the nucleus, remain in demand^{217,218,102,128,200}. We aimed at responding to this demand by rationally designing an amphiphilic peptide that promotes nuclear translocation of oligonucleotides via an NLS incorporated into the peptide backbone. The 23 amino acid amphiphilic peptide (KR)2(HR)2(WL)7W, henceforth termed NLS-peptide, is based on the recently studied (HR)3gT peptide which was able to self-assemble into multi-compartment micelles (MCMs) in the presence of DNA (**Figure 4.1**). The hydrophilic, nucleotide

condensing histidine-arginine repeats of (HR)3gT were extended by a lysine-arginine tandem repeat (KRKR) which constitutes the shortest functional NLS sequence²²⁵. To maintain a hydrophilic to hydrophobic weight ratio conducive to the assembly of micelles²²⁶, the extension of the hydrophilic domain was compensated by increasing the repetitive tryptophan leucine residues in the hydrophobic domain of (HR)3gT.

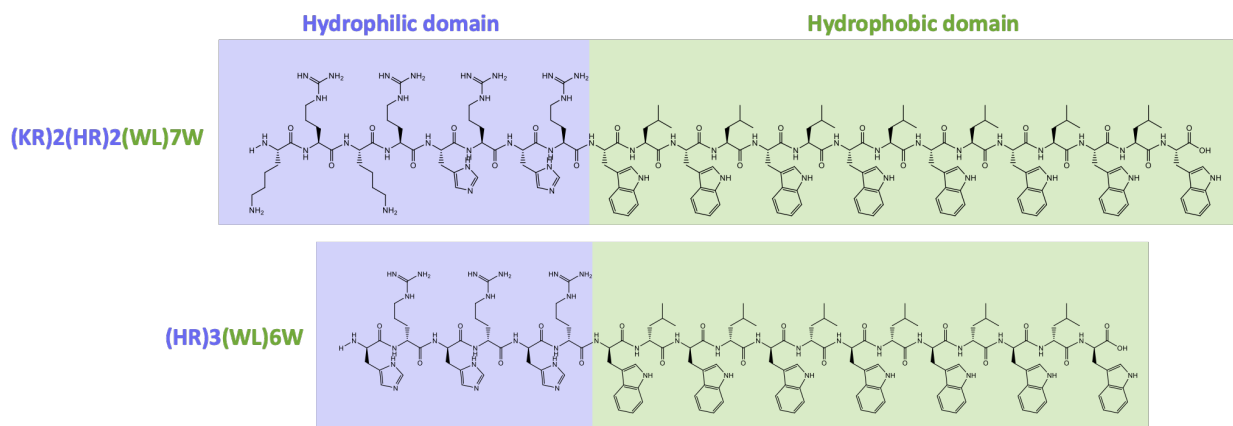


Figure 4.1: Amino acid sequence of the amphiphilic NLS-peptide ((KR)2(HR)2gT) and its precursor (HR)3gT.

The NLS-peptide was synthesized using standard Fmoc-based solid phase peptide synthesis and purified by RP-HPLC. The expected molecular mass of 3455 gmol⁻¹ was confirmed by MALDI-TOF mass spectrometry (**Figure 4.2**).

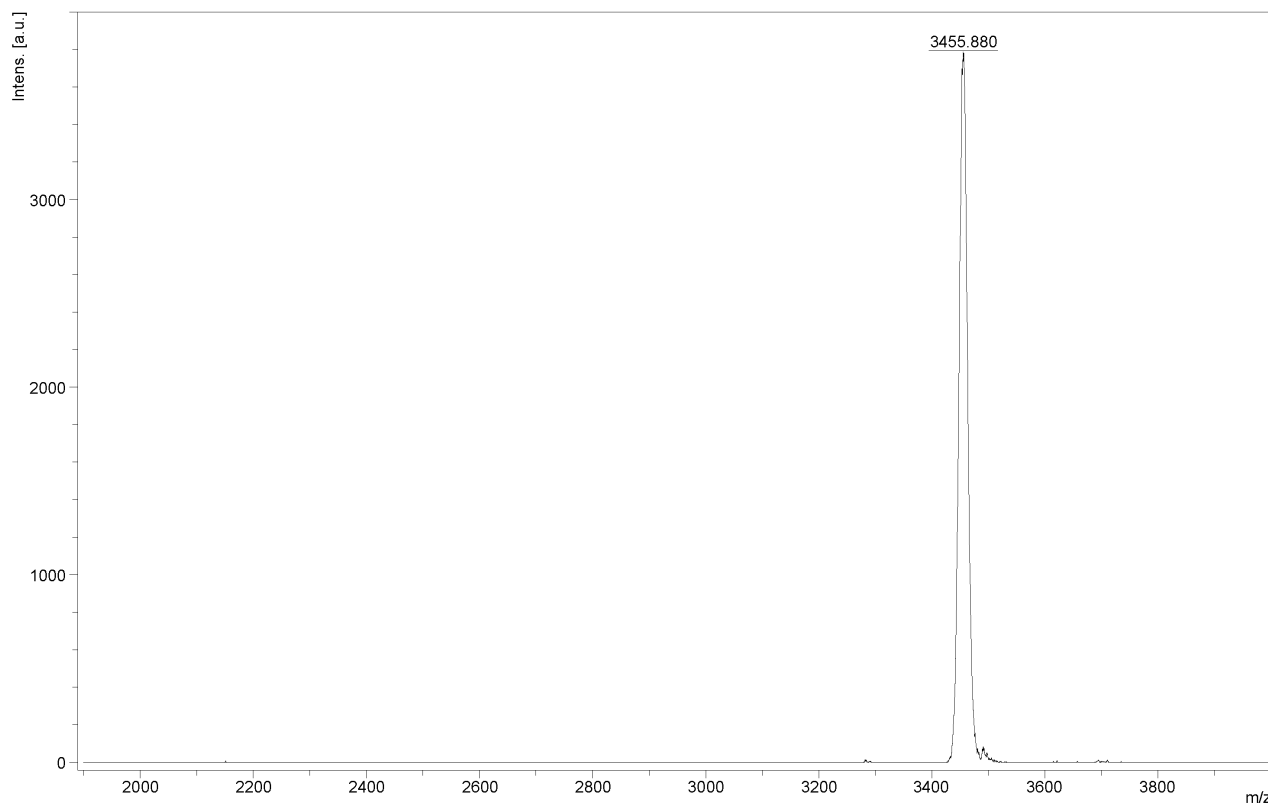


Figure 4.2: MALDI-TOF mass spectrum of NLS-peptide.

Self-assembly of NLS-peptide in the presence of a 22-nucleotide single strand DNA (22nt ssDNA) was performed by solvent exchange using dialysis against water for approximately 24h at 4°C, with two changes of water. The hierarchical self-assembly process of the NLS-peptide into micelles and subsequently into spherical MCMs in the presence of short ssDNA is outlined in Figure 4.3. The short ssDNA is entrapped between individual micelles of the MCM as a result of electrostatic interactions between the positively charged peptide and negatively charged DNA²²⁷.

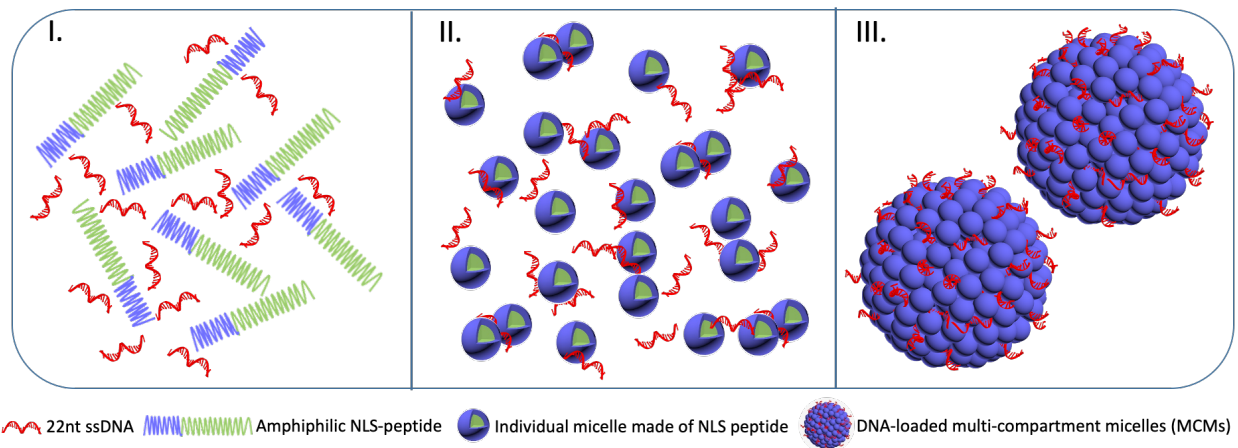


Figure 4.3: Sequential self-assembly process of NLS-peptide in the presence of short ssDNA.

4.3.2 Characterization of NLS-MCMs

4.3.2.1 Morphology

Ultrastructural analysis of NLS-peptide self-assembled in the presence of 22nt ssDNA by electron microscopy (**Figure 4.4**) revealed a spherical morphology and multicompartiment architecture of DNA-loaded NLS-MCMs similar to that observed for (HR)3gT-MCMs, henceforth termed nonNLS-MCMs.

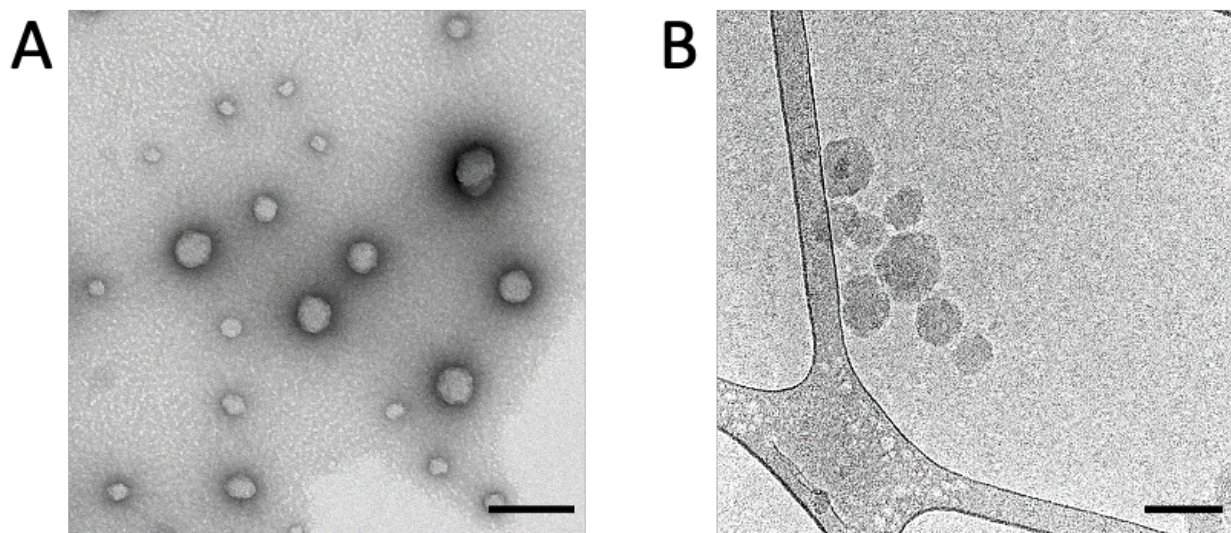


Figure 4.4: Morphology of 22nt ssDNA-loaded NLS-MCMs. (A) TEM, (B) Cryo-EM. Scale bars 100nm.

In the absence of DNA, NLS-MCMs showed a similar architecture (**Figure 4.5**).

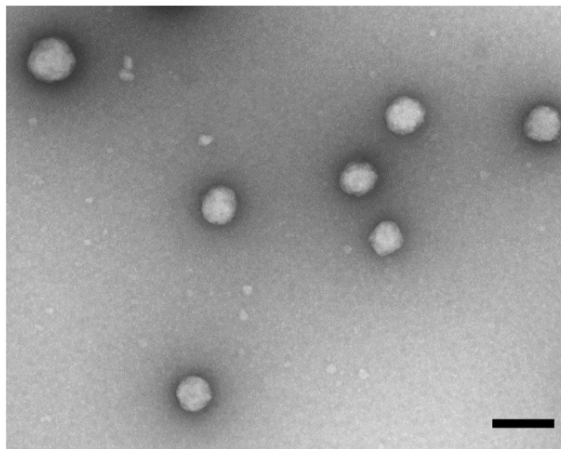


Figure 4.5: TEM image of DNA-free NLS-MCMs, Scale bar = 200nm.

4.3.2.2 Size

NLS-MCMs have a hydrodynamic diameter, D_H of 94 ± 8 nm as measured by DLS (**Figure 4.6A**) with a polydispersity index (PDI) of 0.18. Consistent with DLS measurements, D_H determined by NTA was 91 ± 2 nm (**Figure 4.6B**).

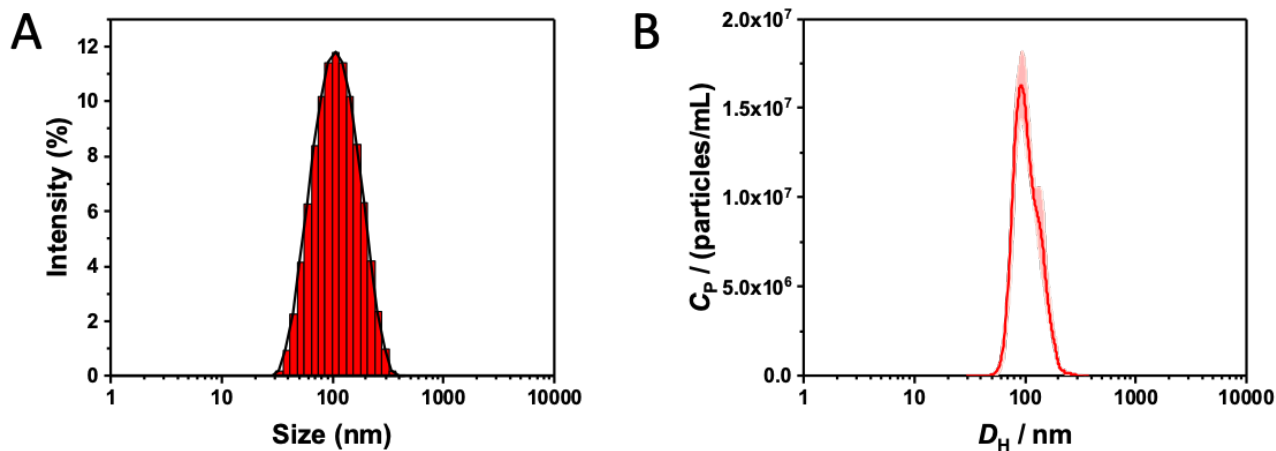


Figure 4.6: Hydrodynamic diameter of 22nt ssDNA-loaded NLS-MCMs. (A) DLS, (B) NTA.

DNA-free NLS-MCMs had the same PDI (0.18) as their DNA-loaded counterpart but exhibited a larger hydrodynamic diameter of 145 ± 4 nm (**Figure 4.7**). The NLS-MCM size

reduction by DNA incorporation is consistent with our previously reported observation that electrostatic interactions between DNA and peptide lead to more compact assemblies ²²⁷.

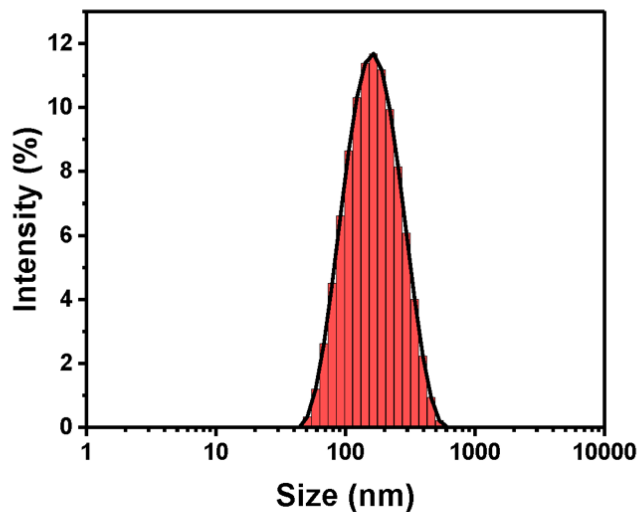


Figure 4.7: DLS of DNA-free NLS-MCMs

4.3.2.3 Surface charge

Zeta potential measurements showed that the surface charge of NLS-MCMs decreased from 45 ± 7 mV to 20 ± 5 mV when negatively charged DNA was entrapped (**Figure 4.8**).

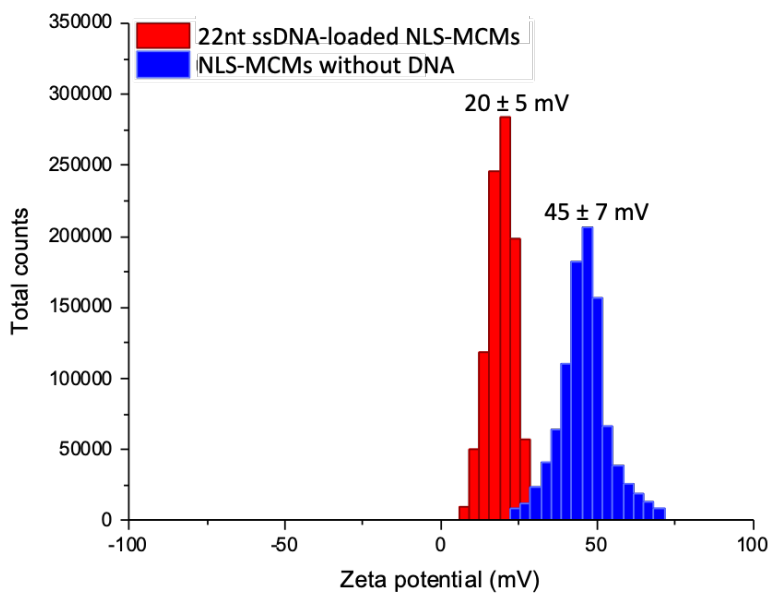


Figure 4.8: Zeta potential of NLS-MCMs with (red) or without 22nt ssDNA (blue).

These data support that the majority of DNA molecules are entrapped between the individual micelles rather than being merely accumulated on the NLS-MCM surface which would yield a more negative zeta potential. The zeta potential of 20 ± 5 mV reflects the physical stability of NLS-MCMs due to the electrostatic repulsion forces between NLS-MCMs which hinder their aggregation. In addition, a zeta potential of ± 20 mV was shown to be advantageous for an effective accumulation of non-viral vectors in target cells ²²⁸.

4.3.3 Quantification of DNA Entrapment into Nanoparticles

The incorporation of DNA into NLS-MCMs was elicited by FCS using Atto550-labeled 22nt ssDNA. Diffusion times (τ_D) of free DNA and DNA-loaded NLS-MCMs in solution are displayed by fitting the experimental autocorrelation curves to the one- and two-component fit, respectively, where τ_D of the free DNA was fixed as the first component (**Figure 4.9**) ²²⁷.

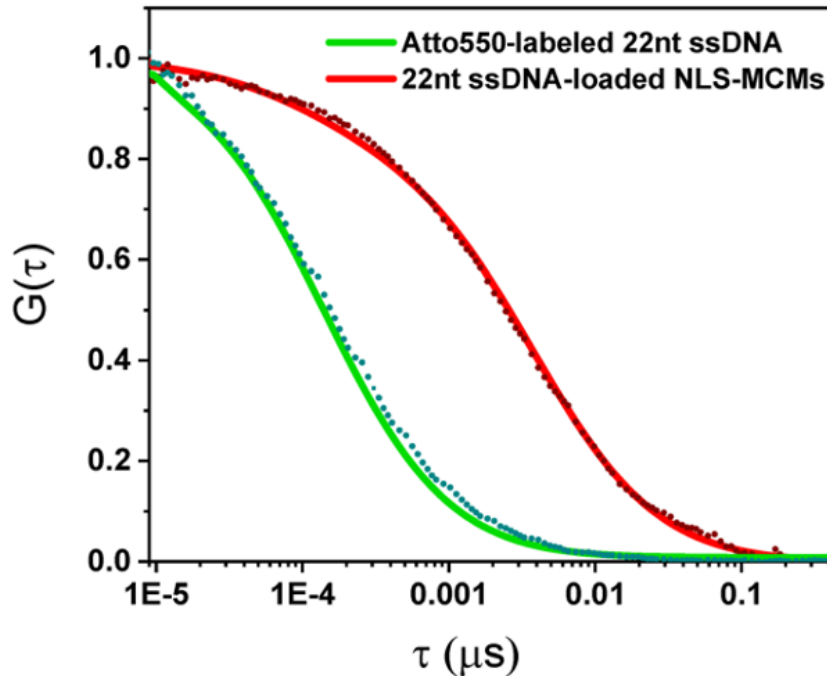


Figure 4.9: Normalised FCS autocorrelation curves of Atto550-labeled 22nt ssDNA-loaded NLS-MCMs (red) and Atto550-labeled 22nt ssDNA (green). Dotted lines represent experimental auto correlation curves and solid lines are fitted curves.

The increased τ_D of DNA-loaded NLS-MCMs ($3778 \pm 1505 \mu\text{s}$) compared to free 22nt ssDNA ($138 \pm 8 \mu\text{s}$) is indicative of DNA entrapment by nanoparticles. Moreover, the number of 22nt ssDNA molecules per particle was calculated to be 14.3 ± 4.4 based on the count per molecule (CPM) ratio of DNA-loaded NLS-MCMs to free DNA.

4.3.4 Thermo-responsiveness of NLS-MCMs

To assess thermo-responsiveness, NLS-MCMs with and without DNA were incubated at 37 °C, and the hydrodynamic diameter and ultrastructure was examined by DLS and TEM, respectively, after 8, 24, 48 and 60 h. The DLS and TEM analyses revealed no change in the size and morphology of MCMs after 8 h at 37 °C. However, after 24 h at 37°C, NLS-MCMs with and without DNA started to disassemble and this temperature response continued over time (**Figure 4.10**). DLS and TEM revealed the gradual formation of two populations consisting of either dispersed or clustered smaller MCMs and individual micelles. The appearance of individual micelles at 24 h resulted in a small shoulder around twenty nanometers in the DLS intensity distribution which increased over time. When kept at 37 °C, the trend to disassemble (change in size and structure) was faster in NLS-MCMs (**Figure 4.10A**) compared to DNA-loaded NLS-MCMs (**Figure 4.10B**), suggesting that the presence of DNA affected the disassembly behavior. It is conceivable that the electrostatic interactions between negatively charged DNA entrapped between positively charged micelles hold micelles together more tightly in DNA-loaded MCMs, resulting in a more compact MCM structure which takes longer to disassemble in response to temperature.

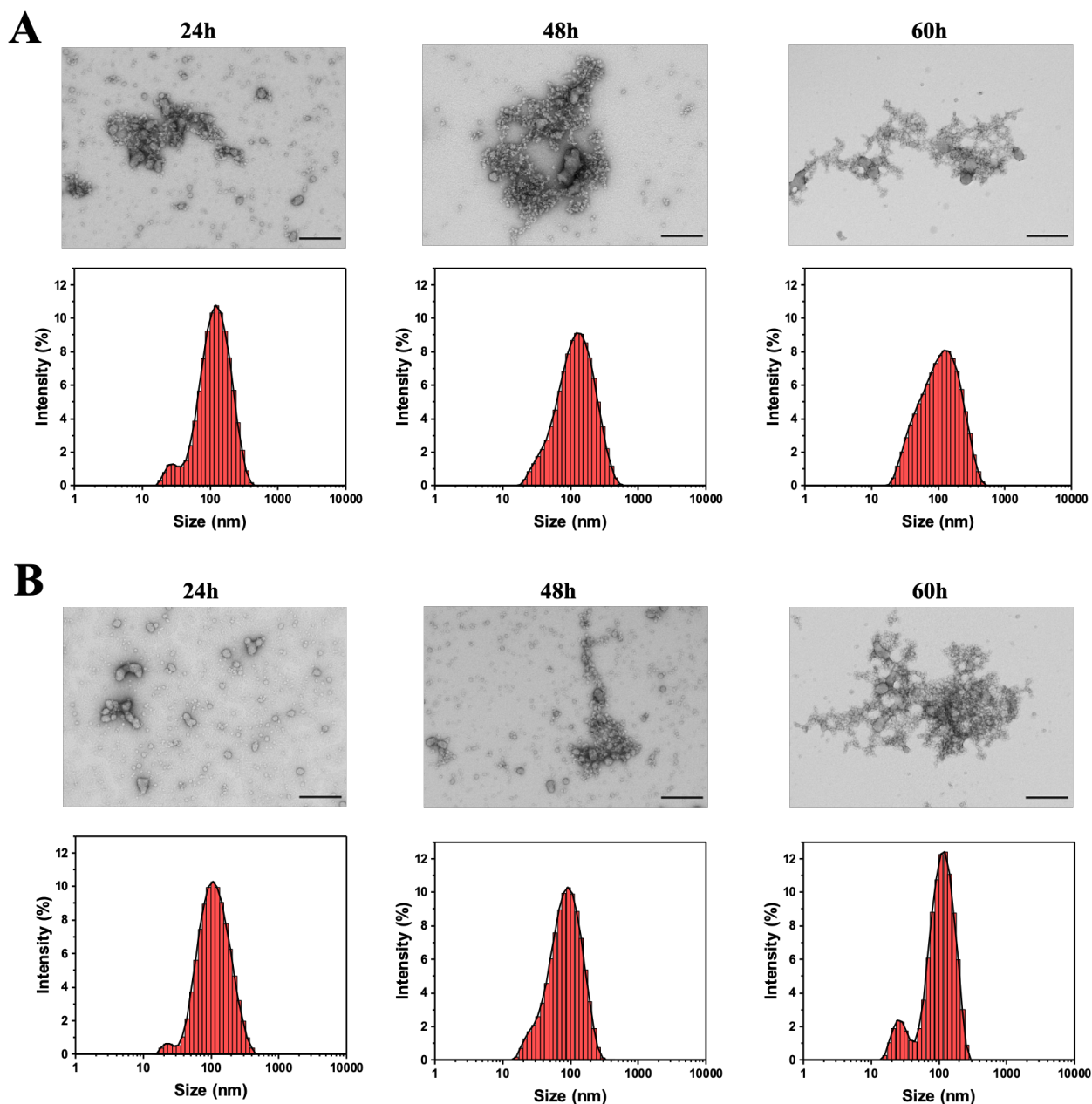


Figure 4.10: TEM and DLS of (A) NLS-MCMs without DNA, (B) 22nt ssDNA-loaded NLS-MCMs after 24, 48 and 60 h incubation at 37°C. Scale bars = 200 nm.

4.3.5 Nuclear Translocation of NLS-MCMs

The successful transport of biomolecules across the selective NPC requires their interaction with different disordered phenylalanine-glycine-rich nucleoporins (FG-Nups) that act as a molecular filter^{229,230}. Most cargo molecules delivered to the nucleus do not interact directly with

FG Nups but require specific transport receptors, predominantly members of the karyopherin beta protein family (Kap β s) such as Kap β 1. Cargoes possessing an NLS can interact with Kap β 1 directly or via an adaptor protein, e.g., karyopherin alpha (Kap α) to enable transport through the NPC. To do so, Kap β 1 forms a heterodimer with Kap α which can then directly bind to NLS-cargo and facilitate its import (Figure 4.11). Ran guanosine triphosphate (RanGTP) gradients control the directionality of transport by triggering the release of cargo inside the nucleus²³¹. As the number of Kaps by far exceeds the number of NPCs in the cell, there is a high likelihood that the pores are always populated by Kaps, but also that Kap β 1 transport complexes are formed in close vicinity of the NPCs²²⁹. In addition, high binding affinity towards FG Nups is necessary for NLS-cargo-Kap α -Kap β 1 ternary complexes to mediate cargo transport^{229,232}. Therefore, the bigger the cargo, the more transport receptors might be required to enable translocation through the NPC²³³.

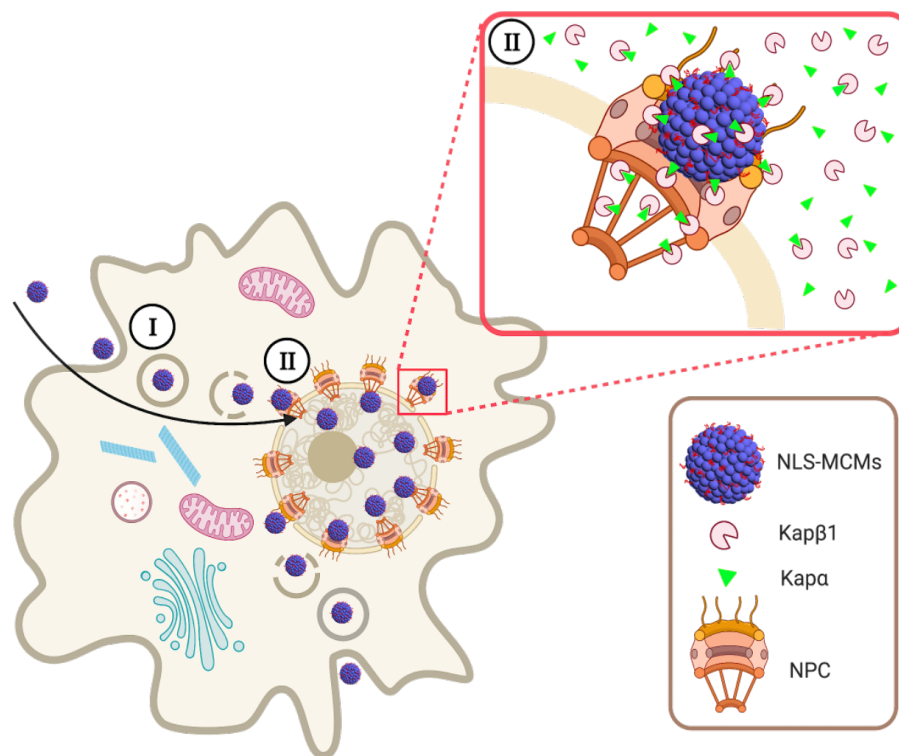


Figure 4.11: Selective nuclear transport of NLS-MCMs facilitated by Kaps.(I) and nuclear localization (II) of NLS-MCMs (created with BioRender.com).

To examine whether NLS-MCMs follow a corresponding nuclear translocation mechanism, we measured the binding of $\text{Kap}\beta 1 \cdot \text{Kap}\alpha$ and $\text{Kap}\beta 1 \cdot \text{Kap}\alpha \cdot \text{NLS-MCM}$ complexes to the FG Nup layer formed on a sensor chip by either cytoplasmic Nup214 or central channel Nup62, by surface plasmon resonance (SPR) (**Figure 4.12A**). Langmuir isotherm analyses using a two-component fit (**Figure 4.12A**) demonstrate that there is no significant difference (within error limits) in the apparent equilibrium dissociation constants (K_{D1} and K_{D2}) obtained for the stand-alone $\text{Kap}\alpha \cdot \text{Kap}\beta 1$ and $\text{Kap}\alpha \cdot \text{Kap}\beta 1 \cdot \text{NLS-MCMs}$ complexes with Nup214 or Nup62 (see **Table 4.1**). Since the $\text{Kap}\alpha \cdot \text{Kap}\beta 1$ complex by itself is already multivalently interacting with FG Nups, it is expected that the measured apparent K_{Ds} would be very similar also for $\text{Kap}\beta 1 \cdot \text{Kap}\alpha \cdot \text{NLS-MCMs}$, because the equilibrium dissociation constants approximate very similar values for the multivalent binding species, when the number of the binding pockets starts to exceed 10 (e.g. for Kaps)²³⁴. Obviously, no difference is expected in the presence of nonNLS-MCMs, which do not interact with the $\text{Kap}\alpha \cdot \text{Kap}\beta 1$ and as such do not interfere at all with the $\text{Kap}\alpha \cdot \text{Kap}\beta 1$ binding to FG Nups. In Table 4.1, the equilibrium dissociation constants are listed together with the maximal SPR binding responses ($R_{\text{max}1}$ and $R_{\text{max}2}$ in resonance units [RU]) for the binding components with K_{D1} and K_{D2} , respectively.

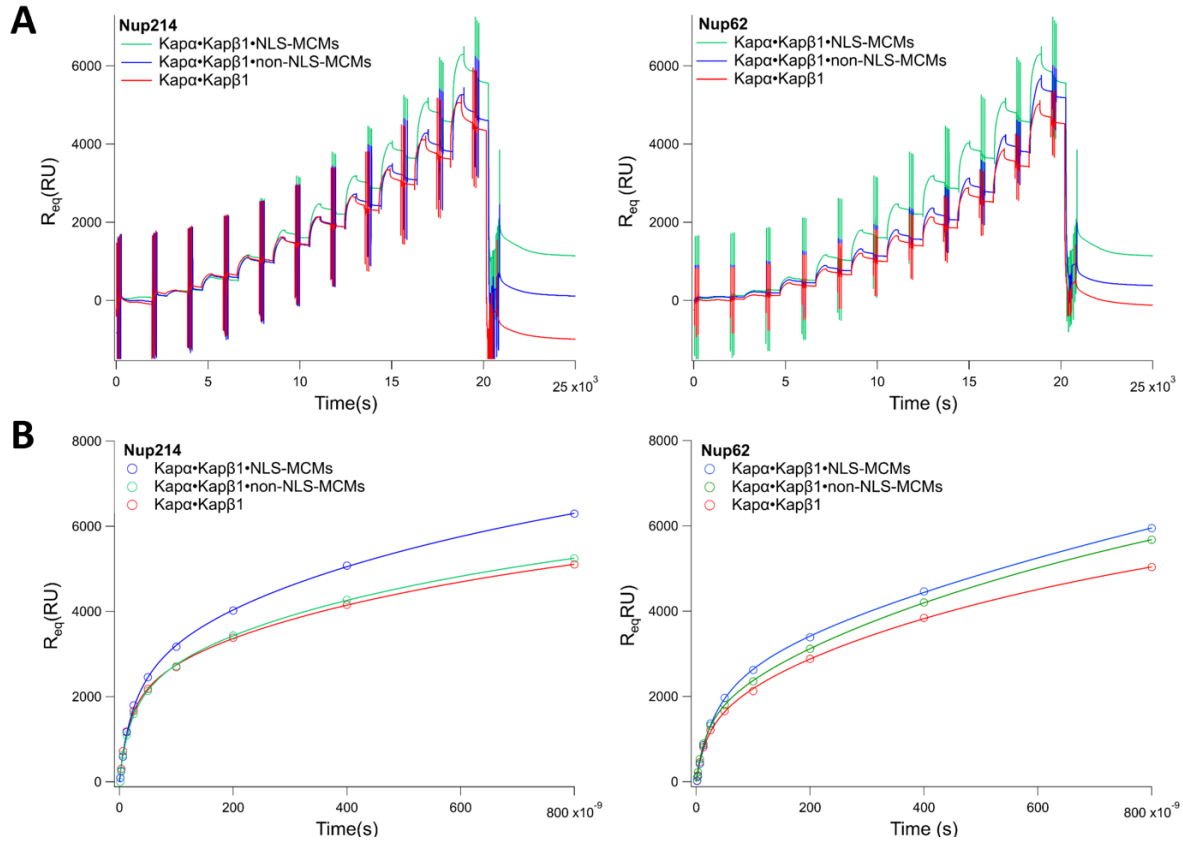


Figure 4.12: SPR sensograms resolve the binding interactions of Kap α •Kap β •NLS-MCMs, Kap α •Kap β •nonNLS-MCMs, and standalone Kap α •Kap β 1 to Nup214 and Nup62. (A) Langmuir isotherms using two-component fit, (B) Langmuir isotherm fits (solid lines) yielding the maximal response signal (R_{max} ; circles). NLS-MCM binding response measured by SPR elicited the highest FG Nup-binding response (blue). NonNLS-MCMs (green) do not bind to the Nup 214 while they demonstrate binding to Nup 62, still lower than NLS-MCMs. Standalone Kap α •Kap β 1 binding is shown in red.

Table 4.1 Maximal SPR response signals and equilibrium dissociation constants of nanoparticles/karyopherin complexes to Nups.

		K_{D1} (nM)	K_{D2} (nM)	R_{max1} (RU)	R_{max2} (RU)
Kapα•Kapβ1•NLS-MCMs	Nup214	28.2+4.7	1183.5+652	3352.3+373	7599.7+1840
	Nup62	36.7+7.4	3387.6+4190	2967.6+399	16295+1470
Kapα•Kapβ1•nonNLS-MCMs	Nup214	23.2+5.5	954.8+647	2723.3+415	5711.8+1480
	Nup62	20.8+2.4	1423+332	2057.2+140	10201+1260
Kapα•Kapβ1	Nup214	19.4+4.8	1028.1+779	2672+387	5711.4+1850
	Nup62	22.4+5.7	1077.3+477	1895+229	7495.2+1420

Interestingly, an increase of 680 and 1888 RU was detected in the binding to Nup214 responses ($R_{\max 1}$ and $R_{\max 2}$) of $\text{Kap}\alpha\cdot\text{Kap}\beta 1\cdot\text{NLS-MCMs}$ compared to standalone $\text{Kap}\alpha\cdot\text{Kap}\beta 1$, respectively. Notably, the binding of $\text{Kap}\alpha\cdot\text{Kap}\beta 1\cdot\text{NLS-MCMs}$ to Nup62 led to a much bigger increase of 1072 and 8800 RU in the maximal binding responses. In contrast, in the presence of nonNLS-MCMs, no (in case of Nup214) or a much smaller (in case of Nup62) increase in the maximal binding response was observed for the $\text{Kap}\alpha\cdot\text{Kap}\beta 1$ binding to the corresponding Nup which confirms that the observed extra response in case of $\text{Kap}\alpha\cdot\text{Kap}\beta 1\cdot\text{NLS-MCMs}$ could be attributed to the additional NLS-MCMs mass in the binding complex. While compared to NLS-MCMs, the increase observed for binding of $\text{Kap}\alpha\cdot\text{Kap}\beta 1$ to Nup62 in the presence nonNLS-MCMs is significantly lower, it can be attributed to the presence and binding affinity of histidine arginine repeats on the surface of nonNLS-MCMs. Arginine-rich regions are prone to interact with binding sites of $\text{Kap}\alpha$ ^{235,217,236}. Nevertheless, our results demonstrate that the HRHRHR residues of nonNLS lack the ability to act as NLS due to the marginal binding affinity for Nup62.

In addition, to compare the NLS functionality in self-assembled MCM nanoparticles to that of free NLS-peptide, the binding of both species to FG Nups was determined (**Figure 4.13**). The maximal response signal ($R_{\max 1}$ and $R_{\max 2}$) and the equilibrium dissociation constants (K_{D1} and K_{D2}) are summarized in Table 4.2.

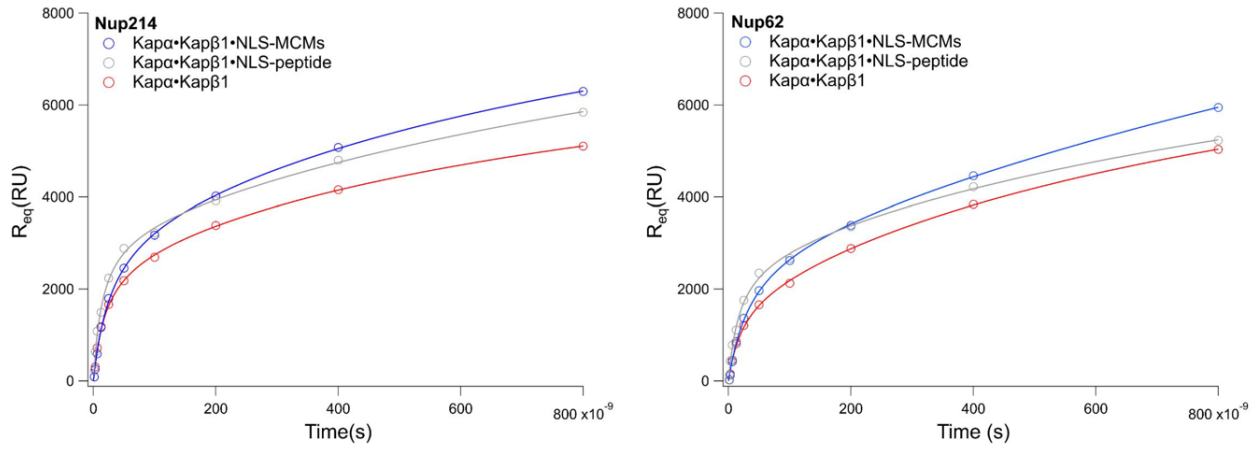


Figure 4.13: Langmuir isotherm fits (solid lines) for Kap α •Kap β 1•NLS-MCMs elicit the highest FG Nup-binding response compared to free NLS-peptide as measured by SPR.

Table 4.2 Maximal SPR response signals and equilibrium dissociation constants of free peptide/karyopherin complexes to Nups.

		K _{D1} (nM)	K _{D2} (nM)	R _{max1} (RU)	R _{max2} (RU)
Kapα•Kapβ1•NLS (free peptide)	Nup214	14.6+2.5	1574.6+1340	3282.8+286	7809.3+3870
	Nup62	17.7+3.4	1396.3+990	2706+283	7122+2700
Kapα•Kapβ1•nonNLS (free peptide)	Nup214	14.1+3.6	878.8+637	2814.9+384	5748.8+1690
	Nup62	14.5+3.2	637.2+216	1804.6+226	4764.2+485
Kapα•Kapβ1	Nup214	19.4+4.8	1028.1+779	2672+387	5711.4+1850
	Nup62	22.4+5.7	1077.3+477	1895+229	7495.2+1420

NLS-MCM binding to Nup214 and Nup62 provoked a maximal binding response that was approximately ~ 0.5 and 1 kRU higher than free NLS-peptide. This data corroborates that when self-assembled into MCMs, NLS-peptides, particularly at higher concentrations, more efficiently expose binding sites for karyopherin complex formation that is required for the interaction with FG Nups. Thus, the high surface to volume ratio offered by nanoparticles represent an attractive

approach to substantially enhance the interactions of biomolecules with their microenvironment and modulated the physicochemical properties with regard to the original molecule^{237,238}.

4.3.6 Effect of NLS-MCMs on Cell Proliferation

To evaluate the cytotoxicity of our peptidic DNA delivery platform, we measured cell proliferation/viability of MCF-7 cells treated for 24 and 48 h with different types of MCMs (Figure 4.14) at a peptide concentration of 0.75 mg/ml. Without DNA cargo, the NLS-MCMs and the nonNLS-MCMs did not affect cell viability after 24 h or 48 h of incubation, showing that the platform by itself is not cytotoxic, also at higher peptide concentrations (Figure 4.15).

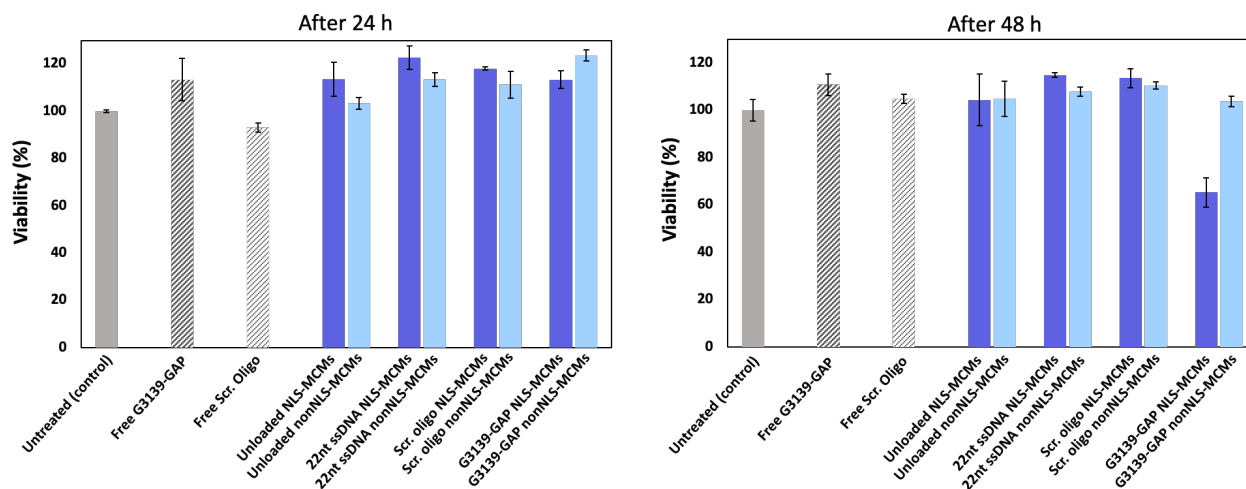


Figure 4.14: Effect of DNA-free and 22nt ssDNA-loaded NLS-MCMs on cell proliferation at a peptide concentration of 1500 μ g/ml compared to lipofectamine complex with corresponding 22nt ssDNA concentration after 24 h of exposure.

Similarly, both NLS- and nonNLS-MCMs loaded with control 22nt ssDNA, scrambled oligonucleotide or ASO had no toxic effects on cell viability after 24 h of exposure. In contrast, lipofectamine-mediated transfection of 22nt ssDNA at the same concentration used for

incorporation into NLS-MCMs (96ng) demonstrated a 40% lower cell viability compared to non-transfected cells (Figure 4.15A).

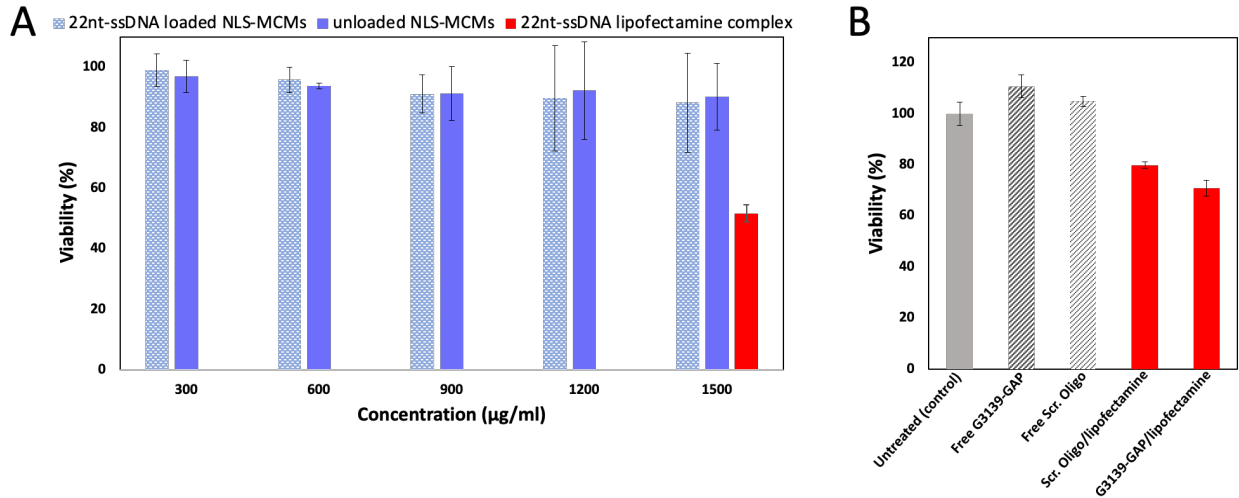


Figure 4.15 A) Effect of DNA-free and 22nt ssDNA-loaded NLS-MCMs on MCF-7 cell proliferation at different peptide concentrations after 24 h of exposure. Comparison at 1500µg/ml peptide concentration to lipofectamine complex with corresponding 22nt ssDNA concentration. B) lipofectamine-mediated transfection of scrambled oligonucleotides and G3139-GAP ASO after 48 h of exposure.

After 48 h, however, cells treated with G3139-GAP loaded NLS-MCMs demonstrated a reduced cell viability of $65 \pm 6\%$. Conceivably, this reduction is caused by G3139-GAP delivery since G3139 ASO was shown to reduce Bcl-2 expression which was associated with apoptosis and a decrease in cell proliferation^{239–242}. Whereas scrambled oligo loaded NLS-MCMs had no toxic effects (Figure 4.14), using lipofectamine reagent to transfect scrambled oligonucleotides revealed a $20 \pm 3\%$ decrease in cell viability after 48 h (Figure 4.15B). The apparent absence of cytotoxicity renders our peptidic platform a promising candidate for therapeutic applications.

4.3.7 Cell Uptake of NLS-MCMs

Uptake of NLS-MCMs loaded with fluorescent DNA in H2B-GFP expressing HeLa cells was examined by CLSM after 5 and 24 hours. The efficiency of 22nt ssDNA uptake at both time points was significantly higher for NLS- than for nonNLS-MCMs (**Figure 4.15**).

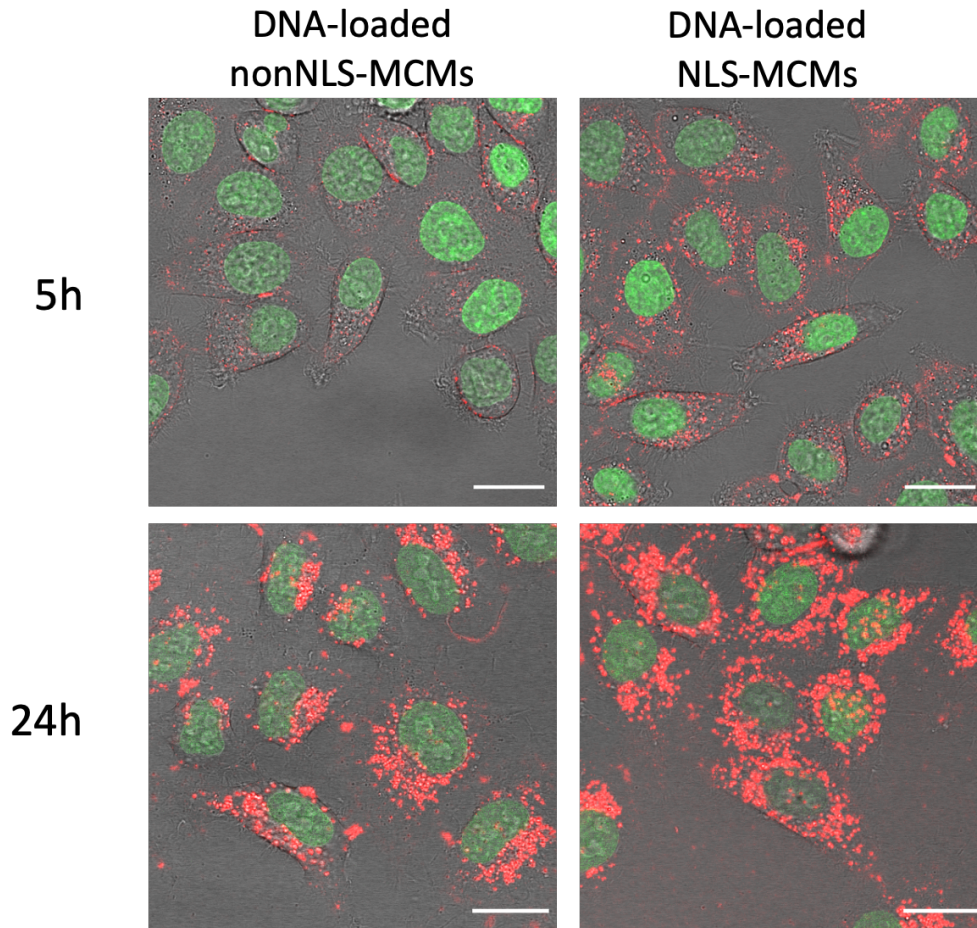


Figure 4.16: CLSM merged images of H2B-GFP expressing HeLa cells recorded after 5 h and 24 h incubation with DNA-loaded nonNLS-MCMs and NLS-MCMs. Scale bars, 20 μ m.

In addition to the enhanced uptake, we observed an increased translocation of NLS-MCMs into the nucleus compared to nonNLS-MCMs. The enhanced cellular uptake can be attributed to different properties conferred upon MCMs by the new NLS-peptide. The KR repeats comprising

the NLS sequence afford the cell penetrating properties and when exposed on the surface of NLS-MCMs, aid in overcoming biological barriers²⁴³. Many studies firmly support the significance of various combinations of lysine and arginine residues in boosting the ability of nanoparticles to enter cells ^{218,244,245}. Moreover, the higher positive surface charge (+20 mV versus +3 mV) and smaller size (90 nm versus 160 nm) of NLS-MCMs compared to nonNLS MCMs play a crucial role in the enhanced uptake ²⁴⁶.

4.3.8 Ultrastructural Localization of NLS-MCMs in Cells

To reveal the fate of MCMs inside the cell at the ultrastructural level, ultrathin serial sections of cell pellets were prepared from HeLa-GFP treated with NLS-MCMs and nonNLS-MCMs, and examined by electron microscopy (**Figure 4.16**). Electron micrographs showed that NLS-MCMs accumulate at the cytoplasmic face of the nuclear envelope (**Figure 4.16A**) where some of them are associated with NPCs. Nanoparticles were frequently detected at NPCs and inside the nucleus, confirming transport through the NPC (**Figure 4.16a-d**). In contrast, nonNLS-MCMs were mainly distributed throughout the cytoplasm. Despite the occasional vicinity of nonNLS particles to the nuclear membrane, a clear association with the NPC was not evident (**Figure 4.16B**).

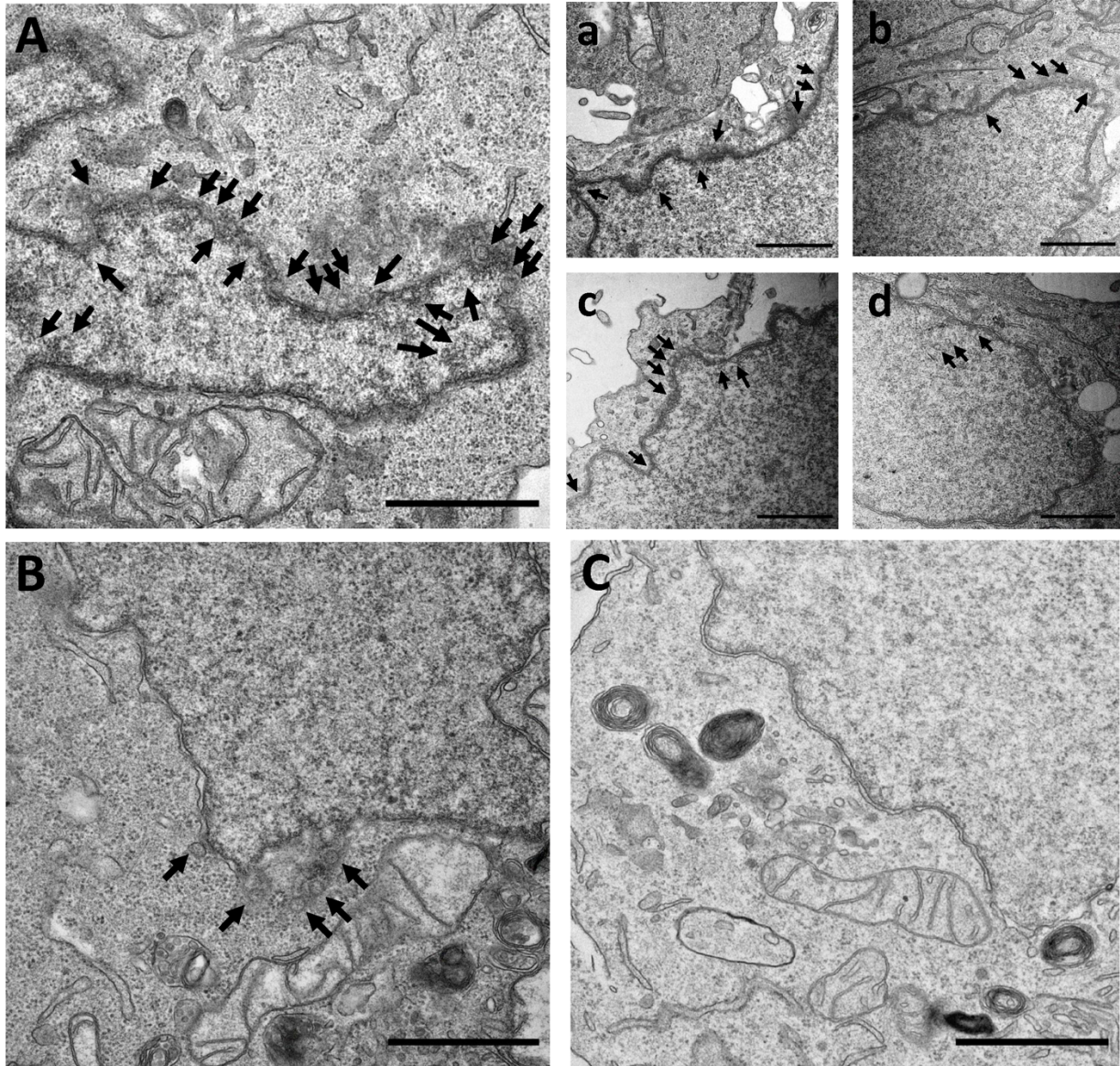


Figure 4.17: Ultrastructural localization of DNA-loaded NLS-MCMs and nonNLS-MCMs in cells. (A, a-d), Electron micrographs reveal NLS-MCMs accumulation at the nuclear envelope, associated with NPCs, and inside the nucleus. (B) Particles assembled from nonNLS-peptide are occasionally detected near the nuclear envelope. (C) Untreated HeLa-GFP cells. Scale bars, 1 μ m.

This data provides further evidence that the KRKR residues at the hydrophilic end of the (HR)3gT peptide serves as functional NLS sequence, able to mediate trafficking of micellar particles to the nucleus. Furthermore, the data are consistent with our SPR results which revealed no (in case of Nup214) or much smaller (in case of Nup62) binding response for nonNLS-MCMs

compared to NLS-MCMs. The presence of histidine-arginine residues on the surface of nonNLS-MCMs appears to also support transport through NPCs but to a significantly lower extent.

4.3.9 Statistical Analysis of Nuclear Localization of NLS-MCMs

Because nonNLS-MCMs also appeared to be entering the nucleus to a limited extent, we statistically investigated HeLa-GFP cells treated with NLS-MCMs or nonNLS-MCMs loaded with fluorescently labeled 22nt ssDNA. Multiple z-stacks of cells were recorded by confocal microscopy at 5, 10, 36, and 48 h of MCM incubation and used for 3D reconstructions based on which the number of MCMs associated with the nuclear membrane and inside the nuclei were determined (**Figure 4.17**).

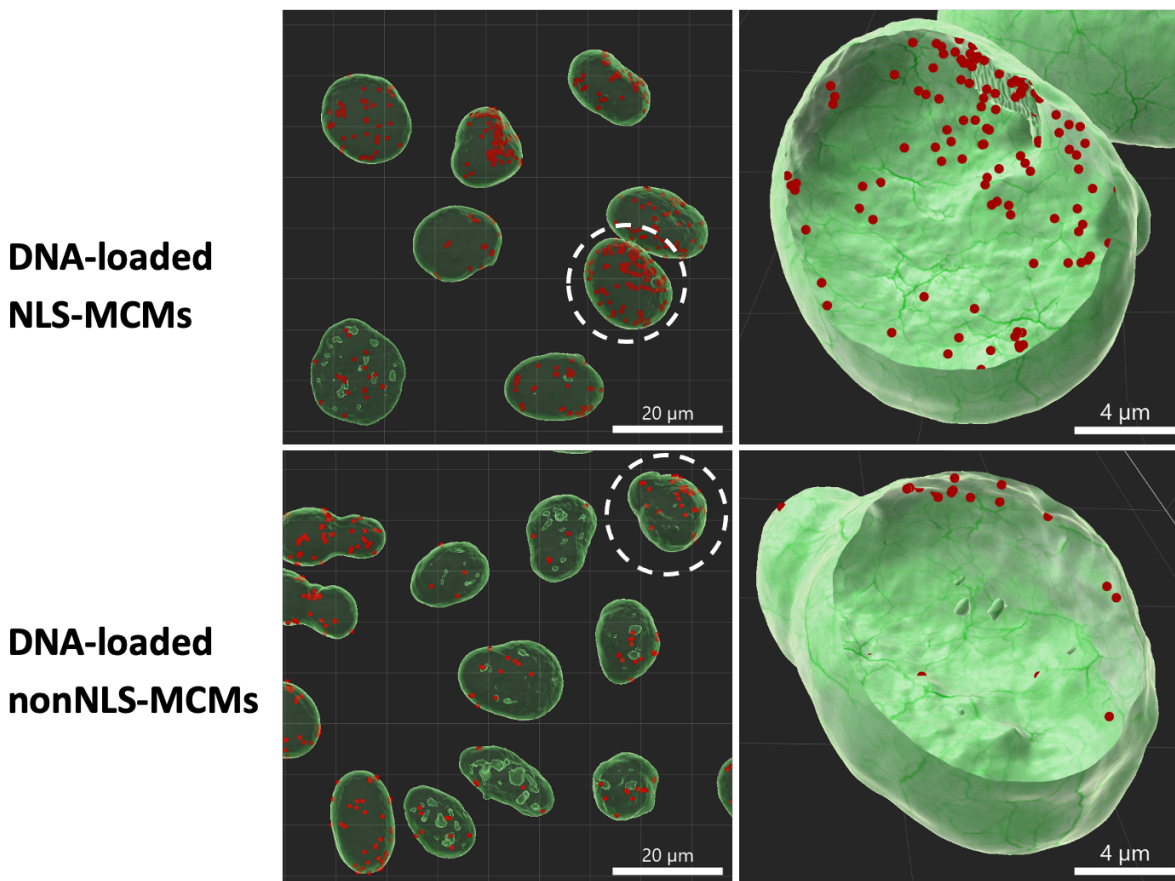


Figure 4.18: Nuclear accumulation of peptide nanoparticles. Imaris 3D reconstructions from multiple confocal sections of HeLa-GFP cells treated for 10h with (A) DNA-loaded nonNLS-MCMs, and (B) DNA-

loaded NLS-MCMs. MCMs are represented by red dots and the nuclear boundaries as green ‘surfaces’, based upon the fluorescence of the corresponding dyes. Displayed spots are at a distance below 0.1 μm to the nuclear membrane and are considered to be inside the nucleus. Dots are displayed in a center point mode.

Statistical analysis of 3D reconstructions at different time-points (5, 10, 36, and 48 h) demonstrated that there is a significant difference in nuclear localization of DNA-loaded NLS-MCMs compared to nonNLS-MCMs (**Figure 4.18**). The average number of DNA-loaded NLS-MCMs inside the nucleus as well as at the nuclear membrane was at least double the number of nonNLS-MCMs ($\alpha=0.05$, $P < 0.01$). The ability of DNA-loaded nonNLS-MCMs to enter the nucleus can be attributed to the surface-exposed arginine–histidine repeating units which have been shown to promote charge interactions with the membrane¹⁶³. The statistical analysis of MCMs in individual cell nuclei confirmed that NLS-MCMs accumulate in the nucleus over time. These results suggested that NLS-MCMs are a promising nanocarriers for the delivery of antisense oligonucleotides targeting pre-mRNA in the cell nucleus.

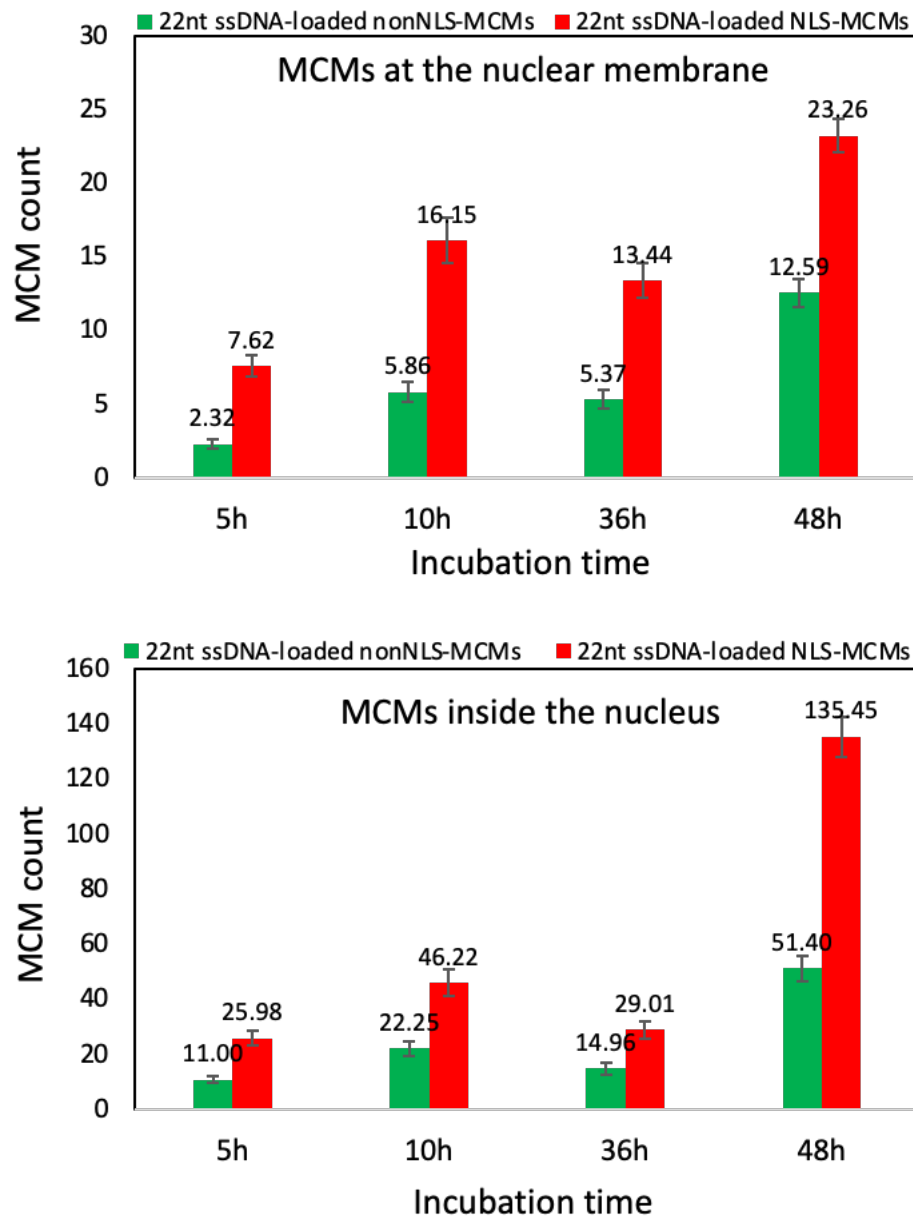
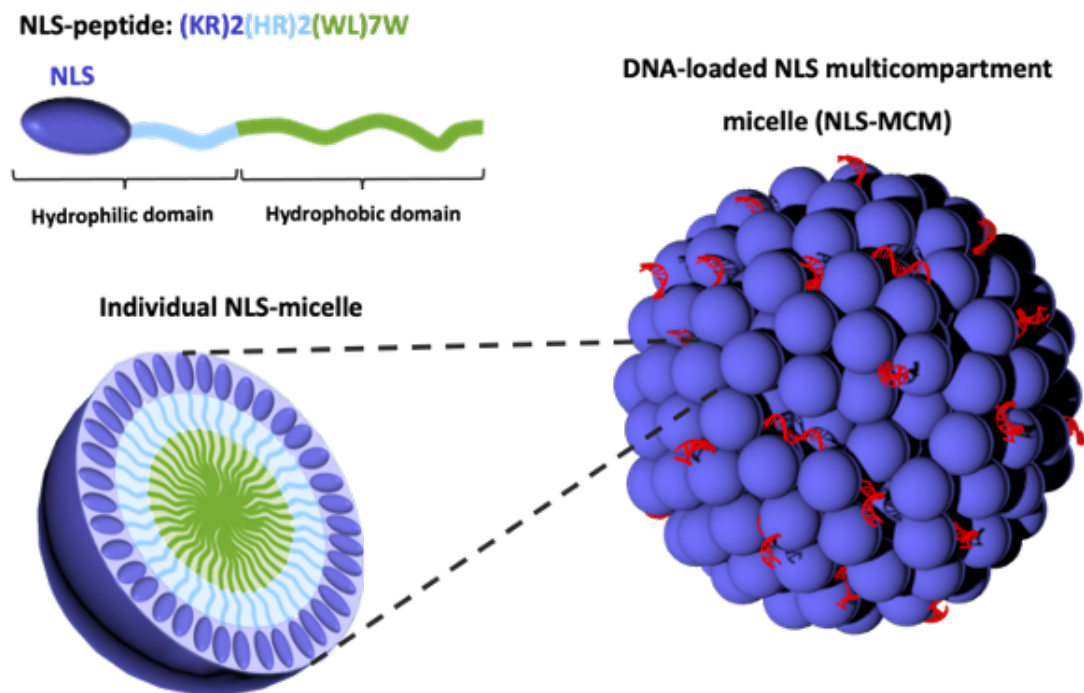


Figure 4.19: Statistical evaluation of NLS- compared to nonNLS-MCMs localized inside the nucleus and at the nuclear membrane at different time-points by Imaris. Bars represent number of MCMs per nucleus. *Top*, MCMs detected within a distance of $\pm 0.1 \mu\text{m}$ to the nuclear membrane were considered on the membrane. *Bottom*, MCMs at a distance below $-0.1 \mu\text{m}$ to the nuclear membrane were considered inside the nucleus. The differences for each time-point were statistically significant between NLS- and nonNLS-MCMs ($p < 0.01$) on both graphs. Error bars represent standard error of the mean (SEM). The number of analyzed nuclei for 5, 10, 36 and 48 h timepoints were 38, 44, 78, 98 and 41, 41, 78, 116 for nonNLS- and NLS-MCMs, respectively.

4.4 Conclusion

In this part of the Thesis, we developed DNA-loaded MCMs to direct DNA delivery to the cell nucleus. To this end, we integrated KRKR amino acid residues as NLS targeting moieties in the rational design of the amphiphilic (KR)₂(HR)₂gT peptide. Purely peptidic nanoparticles with a positive surface charge of +20 mV and an average diameter of 90 nm had no toxic effect on HeLa cells which points to a great potential of NLS-MCMs for a safe delivery of genetic materials to the nucleus. Our SPR results confirmed that Kap α •Kap β 1 authenticates and binds NLS-MCMs and subsequently facilitates their binding to specific FG Nups in order to efficiently transport particles through the NPC. Moreover, molecular and cellular studies together with statistical analysis demonstrated that KRKR residues mediate trafficking of micellar particles to the nucleus. TEM-based ultrastructural results verify that while the majority of NLS-MCMs were detected at the nuclear membrane or about to enter the NPC, nonNLS-MCMs were much less abundant in the vicinity of the nuclear envelope and showed no apparent association with the NPC. Notably, MCMs are thermo-responsive and start to dissociate to smaller micellar structures and/or individual micelles after 24 h at 37°C. The ease of producing targeted peptide-based vectors through one-step self-assembly besides the countless variations of their amino acid sequence make peptides an attractive platform for delivering diverse genetic payloads. Future *in vivo* biodistribution and pharmacokinetic studies are required to explore the biocompatibility and stability of peptidic MCM-NPs in model organisms and to optimize their delivery efficiency for medical applications.

5 NLS-MCMs for the delivery of antisense oligonucleotides directed against Bcl-2⁴



Antisense oligonucleotides (ASOs) are synthetic DNA oligomers whose potential as therapeutic agents has been extensively explored^{247,248}. ASOs modulate the stability, processing, or activity of RNA by various mechanisms. In the cytoplasm, ASOs are designed to bind to a target mRNA which can lead to a steric block of the translation machinery, and more importantly, recruit ribonuclease H (RNase H), a ubiquitous endonuclease specific for DNA-RNA heteroduplexes that will cleave or degrade the RNA. Once the mRNA is degraded, the ASO is recycled for another

⁴ A publication based on the data discussed in this chapter is Submitted: S. Tarvirdipour, M. Skowicki, C. A. Schoenenberger, L. Kapinos, R. Y. H. Lim, K. Benenson, C. G. Palivan, (2022), Submitted.

base-pairing with any available target mRNA molecule. The overall effect of this procedure is a sustained decrease in target mRNA translation and subsequent reduction of the corresponding protein level^{249,250}. In the nucleus, ASO mainly hinder mRNA maturation by inhibiting 5'-mRNA cap formation, by RNA splice modulation, and RNase H-mediated pre-RNA cleavage²⁵¹. RNase H found both in the cytoplasm and the nucleus although it enriches in the nucleus, where it is involved in DNA replication²⁵². Cleavage of mRNA by RNase H is the most validated ASO mechanism, widely used for mRNA knockdown²⁵³.

G3139 is an 18nt phosphorothioate ASO (Genasense®), complementary to the first six codons of Bcl-2 mRNA, resulting in the inhibition of mRNA translation and triggering RNase H dependent mRNA degradation²⁵⁴. The Bcl-2 gene product is an integral membrane protein that inhibits apoptosis. It has been implicated in the growth of a variety of solid tumors including breast, lung, renal, ovary, prostate and skin cancers (melanomas), and has been reported to promote chemo- and radiotherapy resistance²⁵⁵. There are several phase I to III clinic trials investigating different ASOs that target bcl-2²⁵⁶. The aim in G3139 gene therapy is that by downregulating Bcl-2, a pro-apoptotic effect is achieved that counteracts the cancer cell's ability to evade programmed cell death. Although G3139 functions both in the cytoplasm and nucleus, the different subcellular localization in particular nucleus affect its therapeutic potency^{257,258}. Notably, it was shown that accumulation of G3139 in the nucleus following cationic lipid transfection correlates with Bcl-2 down-regulation brought about by the enrichment of RNase-H in the nucleus²⁵⁹.

Given peptides unique properties and straightforward production, finetuning functional peptides opens multi-faceted avenues in a variety of complex applications including antisense oligonucleotide therapies^{260,218}. The studies described in chapter 4 revealed that ssDNA-loaded NLS-MCMs were efficiently internalized into the cytoplasm and trafficked to the nucleus with no

cytotoxic effect. To take advantage of these vector properties, we aimed for loading NLS-MCMs with G3139, a RNase-H dependent ASO ²⁵⁰ and testing the effect of G3139 delivery on Bcl-2 expression. Notably, Cheng et al. developed a lipid nanoparticle formulation to deliver chemically modified G3139 for lung cancer treatment ²⁶¹. Their findings suggested that the gapmer version of G3139 (G3139-GAP) containing additional 2'-methoxyethyl (2'-MOE) substitutions at the 5' and 3' end of the ASO, more efficiently downregulated Bcl-2 in A549 lung cancer cells compared to the early-generation phosphorothioate G3139 ²⁶¹.

In this chapter, as a proof of concept we address the potential of NLS-MCM platform as a non-viral delivery vector in ASO therapy. In this regard, we investigated the incorporation of G3139-GAP and G3139 into NLS-MCMs by characterising the morphology and physicochemical properties of ASO-loaded NLS-MCMs. Then, cell studies were performed to evaluate the ability of G3139-GAP-loaded MCMs to deliver functional G3139-GAP that can modify Bcl-2 mRNA and reduce overall Bcl-2 levels.

5.1.1 Morphology of ASO-loaded MCMs

The ultrastructure of nanocarriers resulting from NLS- and nonNLS-peptide self-assembly in the presence of G3139-GAP, G3139 and scrambled non-specific oligonucleotides was examined by TEM (**Figure 5.1**). High magnification TEM micrographs indicated multi-compartment micellar nanostructure formation in the presence of all three oligonucleotides similar to that previously observed in the presence of the 22nt ssDNA (**Figure 4.4**). A comparison of NLS- (**Figure 5.1A**) and nonNLS-peptide nanoassemblies (**Figure 5.1B**) showed that both peptides self-assembled into MCMs with a similar multicompartment micellar morphology though G3139-GAP loaded NLS-MCMs appeared to form large numbers of smaller MCMs.

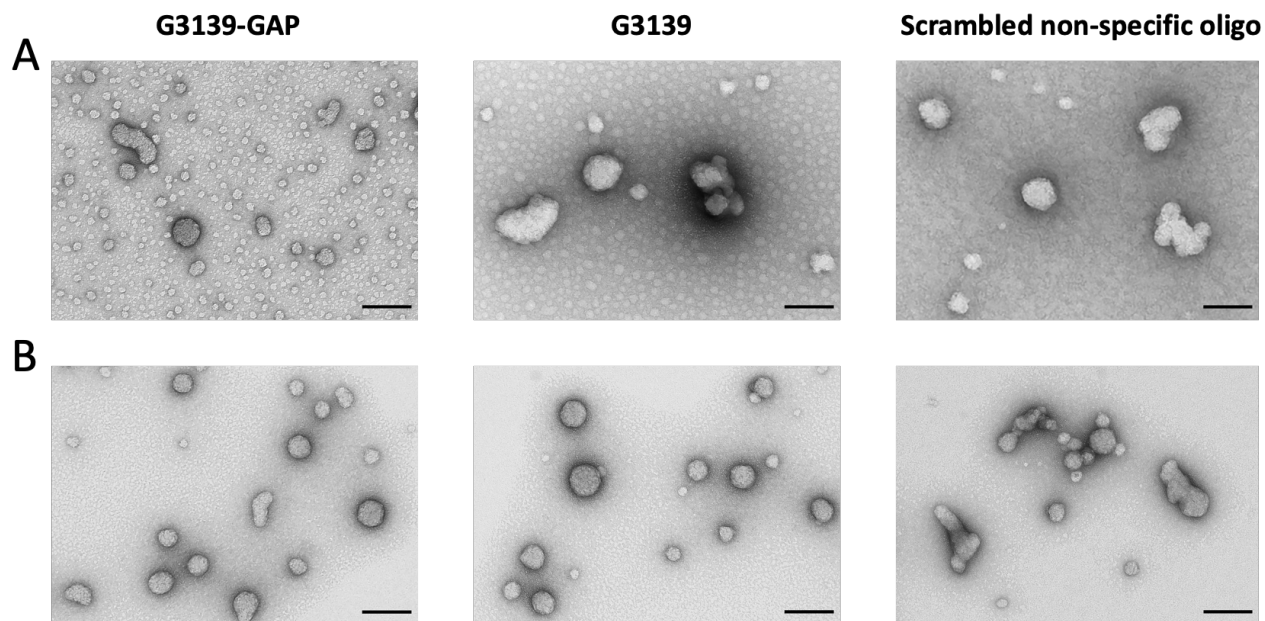


Figure 5.1: TEM micrographs of (A) NLS-MCMs and (B) NonNLS-MCMs loaded with different oligonucleotides. Scale bars = 100 nm.

5.1.2 Size of ASO-loaded MCMs

The scattered numbers measured by DLS demonstrated a narrow size distribution below 100 nm for all oligonucleotide payloads (**Figure 5.2**), consistent with DLS measurements obtained for the 22ss DNA shown in chapter 4 (**Figure 4.6**). Size analysis of G3139-GAP loaded NLS-MCMs by DLS showed a hydrodynamic diameter (D_H) of 48 ± 12 nm (**Figure 5.2A**). The physicochemical properties of gene delivery assemblies, notably size have a great impact on cellular uptake which, in turn may influence the intracellular mobility and stability of nanoassemblies and thus, affect transfection efficiency²⁶². It is noteworthy that an average size below 100 nm showed maximum cellular uptake regardless of the nanoparticle core composition or surface charge²⁶³.

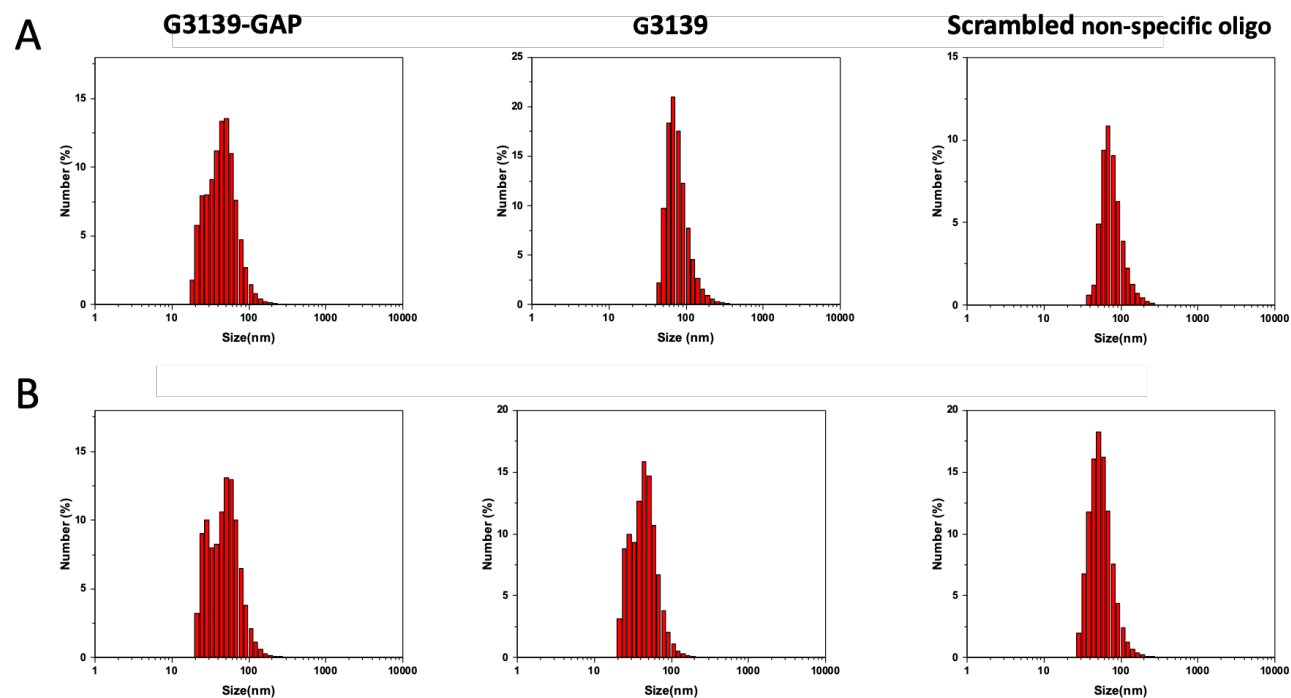


Figure 5.2: DLS measurements revealing the hydrodynamic diameter of (A) NLS-MCMs and (B) NonNLS-MCMs loaded with different oligonucleotides.

5.1.3 Charge of ASO-loaded MCMs

Zeta potential measurements showed that the surface charge of 25 ± 6 mV for G3139-GAP loaded NLS-MCMs (**Figure 5.3**) is similar to the surface charge of 20 ± 5 mV for NLS-MCMs after loaded with 22ss DNA. As expected, due to the extra arginines and lysines included in the hydrophilic domain of the NLS-peptide, the surface charge of NLS-MCMs loaded with ASOs was higher than for corresponding nonNLS-MCMs. A summary of the mean hydrodynamic diameters (D_H), polydispersity indices (PDI) and zeta potentials for the corresponding MCMs is presented in Table 5.1.

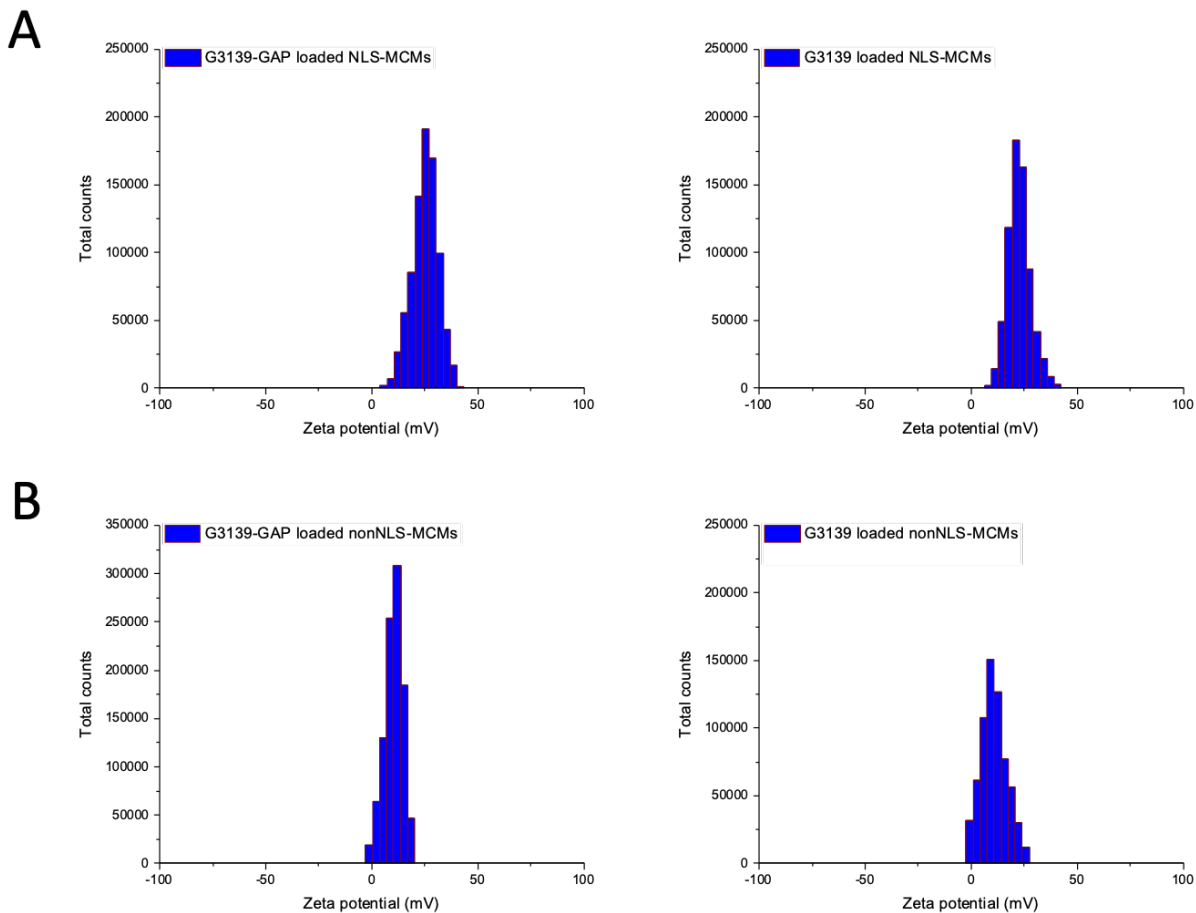


Figure 5.3: Zeta potential of (A) NLS-MCMs and (B) NonNLS-MCMs loaded with G3139-GAP or G3139.

Table 5.1 Characterization of NLS- and nonNLS-MCMs loaded with different oligonucleotides, suspended in water, at pH 7.

MCM-NPs	PDI	D _H (DLS-nm)	Zeta potential (mV)
G3139-GAP loaded NLS-MCMs	0.26	48±12	25±6
G3139-GAP loaded nonNLS-MCMs	0.28	52±14	10±4
G3139 loaded NLS-MCMs	0.21	79±7	23±5
G3139 loaded nonNLS-MCMs	0.23	47±12	9±3
Nonspecific oligo loaded NLS-MCMs	0.19	76±2	NA*
Nonspecific oligo loaded nonNLS-MCMs	0.18	58±8	NA*

*Not Applicable

5.1.4 Cellular uptake of ASO-loaded MCMs

The cellular uptake of NLS- and nonNLS-MCMs loaded with fluorescently labeled Atto550-G3139-GAP and Atto550-G3139 was examined in HeLa, PMA-stimulated THP-1 and MCF-7 cells by confocal laser scanning microscopy (CLSM). Comparing the confocal images of different cells incubated with NPs for 24 h revealed that for all cell lines, significantly higher numbers of ASO-loaded NLS-MCMs were internalized compared to nonNLS-MCMs (**Figure 5.4**). However, CLSM images showed no major difference between G3139-GAP and G3139 payloads. As detailed in chapter 4 for NLS-MCMs, the higher uptake efficiency of ASO-loaded NLS-MCMs can be largely attributed to surface-exposed NLS functional groups consisting of arginine–lysine repeating units which also contribute to the higher positive surface charge of NLS-MCMs. The cell penetration properties of arginine, lysine and histidine have been extensively utilized to translocate payloads across biological membranes²⁴⁴.

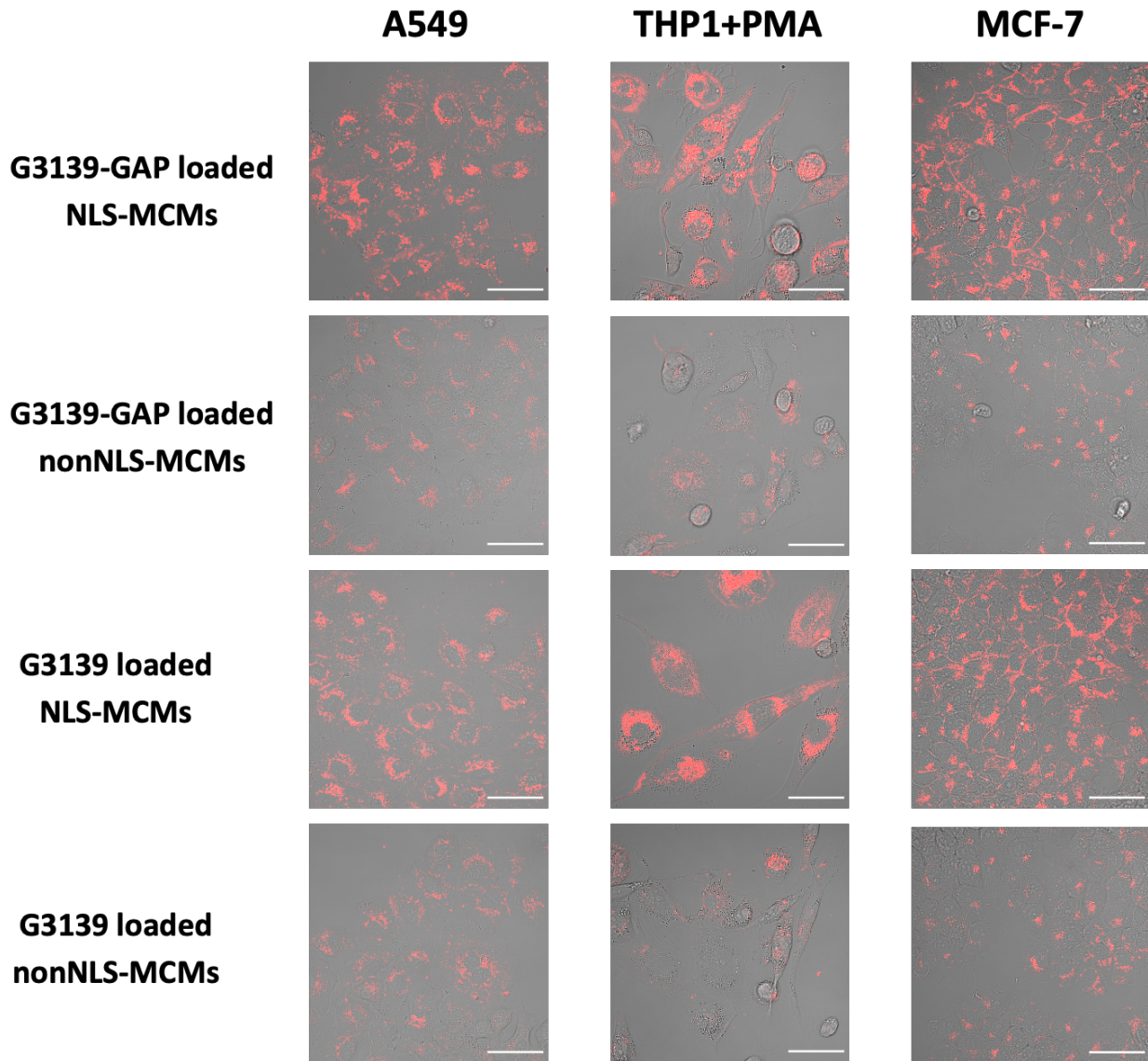


Figure 5.4: CLSM merged images of A549, THP-1stimulated with PMA and MCF-7 cells recorded after 24 h incubation with G3139-GAP- and G3139-loaded NLS- and nonNLS-MCMs. Scale bars, 50µm.

5.1.5 Bcl-2 Downregulation by ASO-loaded MCMs

We first validated the specificity of primary antibodies to Bcl-2 and GAPDH, a reference housekeeping protein, in different cell lines (**Figure 5.5**). After separating equal amounts of total protein extract by SDS-PAGE, proteins were transferred to a carrier membrane which was then probed with antibodies against GAPDH and Bcl-2. The intensity of the bands detected by the

antibody against GAPDH was comparable for all cell lines, confirming that similar amounts of protein were loaded. The antibody against Bcl-2 hardly detected any protein in the A549 cell line, whereas for all the other cell lines it revealed two bands, one of which most likely represents the phosphorylated form of Bcl-2²⁶⁴⁻²⁶⁶. Although normalization against GAPDH showed that THP-1 cells express the highest level of Bcl-2 protein, we chose to test the effect of NLS-MCMs loaded with Bcl-2 antisense oligonucleotides in MCF-7 cells as all our uptake studies were done in adherent cells.

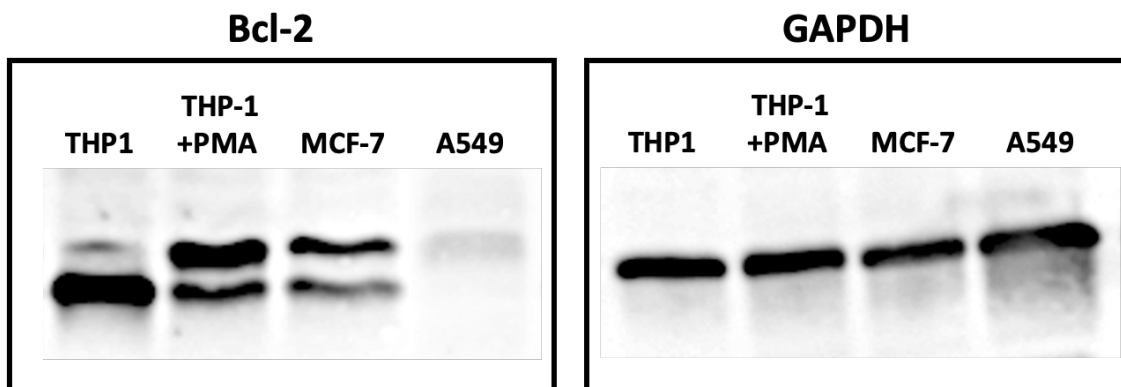


Figure 5.5: Validation of antibody against (A) Bcl-2, and (B) GAPDH in untreated THP-1, PMA-stimulated THP-1, MCF-7, and A549 cell extracts. For immunoblotting, equal amounts of total protein cell extract were loaded in each lane of an anykD precast protein gel and separated by SDS-PAGE.

To obtain quantitative data from Western blots, we determined the linear range of signal intensities for GAPDH detection by probing increasing dilutions of MCF7 cell lysates and the sensitivity of Bcl-2 detection by probing different concentrations of human recombinant Bcl-2 (Figure 5.6 A and C, respectively). For GAPDH, the linear regression with R^2 of 0.98 reflected that the loading range of 1-15 μ g of MCF-7 cell lysates is in the linear range (Figure 5.6 B). Human recombinant Bcl-2 demonstrated a proportional increase in the band intensity in the range of 0.25-10ng (Figure 5.6 D).

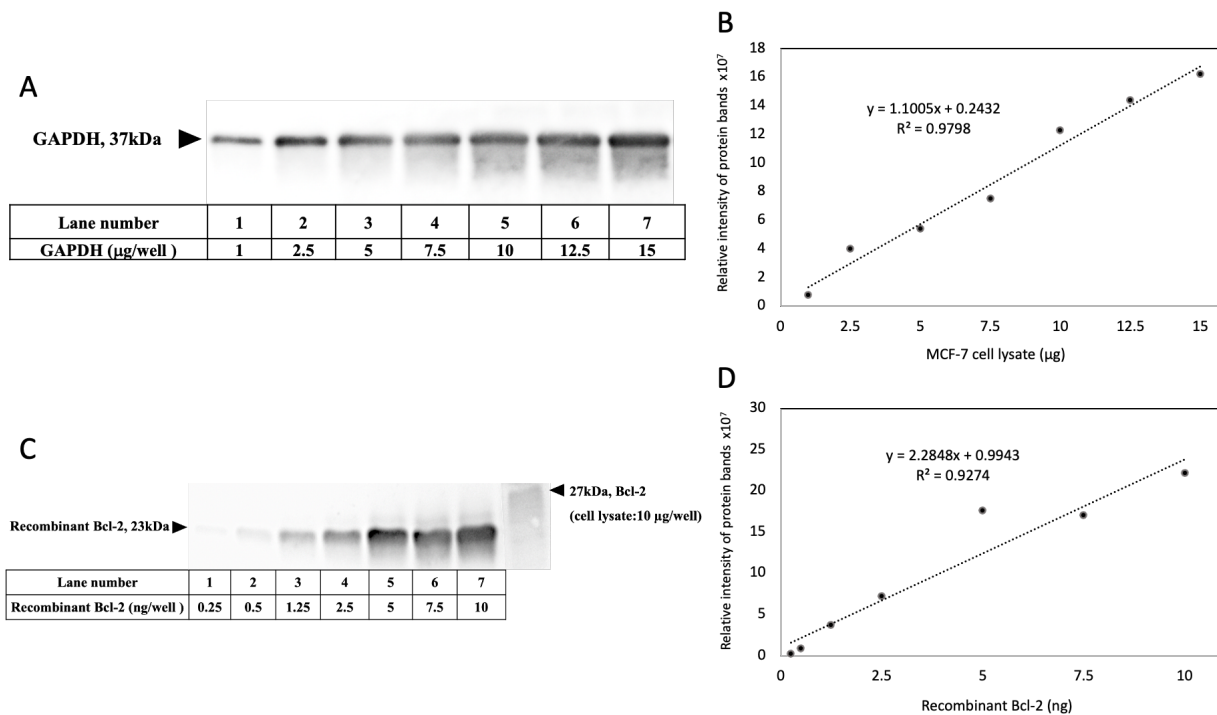


Figure 5.6: Linear relationship between sample concentration and band intensity in Western blot probed with (A, B) antibodies against GAPDH, and (C, D) antibodies detecting Bcl-2.

To assess whether NLS-MCMs loaded with ASOs against Bcl-2 had an effect on Bcl-2 protein levels, MCF-7 cells were treated with equal amounts ($7.3 \times 10^7 \pm 9.86 \times 10^6$ NPs/ml) of NLS- and nonNLS-MCMs loaded with G3139, G3139-GAP, a scrambled oligo (negative control), and with ASO/lipofectamine complexes (positive control) for 48 h. Western blots with 10 μg of cell lysates probed with antibodies against Bcl-2 and GAPDH revealed a decrease of Bcl-2 in cells transfected with NLS-MCMs loaded with G3139-GAP compared to untransfected cells (**Figure 5.7 A, B**). Consistent with the study by Cheng et al., our data for NLS-MCMs demonstrated a higher reduction in Bcl-2 protein levels for G3139-GAP than G3139 (**Figure 5.7**)²⁶¹. For G3139-GAP payload, Bcl-2 levels were decreased by 19% in cells transfected with NLS-MCMs whereas nonNLS-MCMs appeared to have no effect on Bcl-2 translation. It is possible that decrease mediated by NLS-MCMs reflects the increased nuclear localization of the NPs and a

corresponding release of the ASO. Transfection with lipofectamine/ASO complex showed a stronger decrease in the level of Bcl-2 (33% versus 19%). However, as shown in Figure 4.14, lipofectamine complexes exhibit considerable cytotoxicity which overrides the advantage of the increased downregulation.

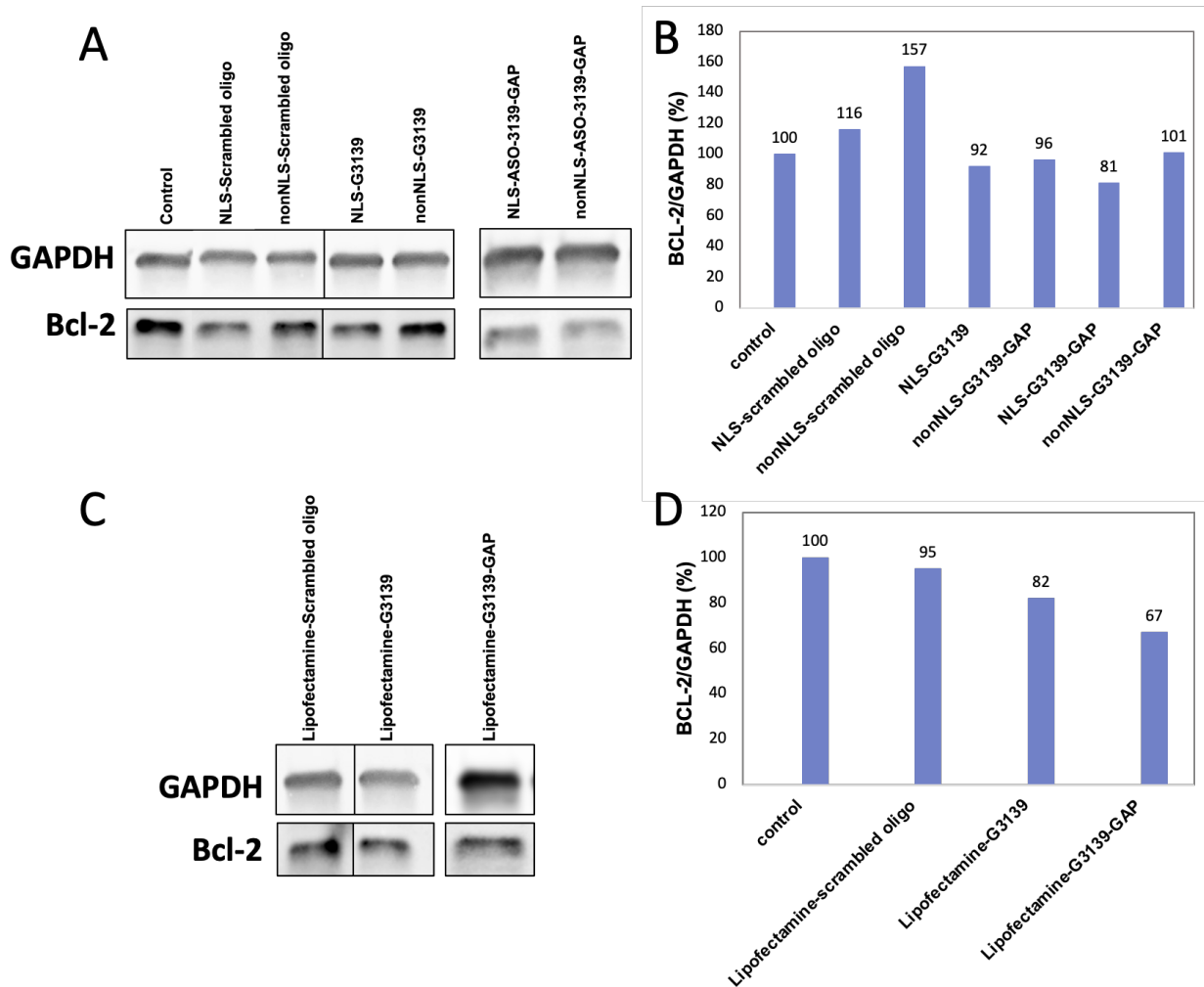


Figure 5.7: Western blot analysis of Bcl-2 proteins in 10 μ g of MCF-7 cell lysates (A)NLS and nonNLS MCMs, (B) lipofectamine (positive control). Relative Bcl-2 protein expression to GAPDH upon treatment with (C)NLS and nonNLS MCMs, (D) lipofectamine.

In the next step, we assessed the particle-number dose response using the four times higher MCM concentrations. Western blots were carried out to quantitatively assess overall BCL-2 levels

in cells incubated for 24 and 48 h with equal amounts ($2.2 \times 10^8 \pm 2.96 \times 10^7$ NPs/ml) of either NLS- or nonNLS-MCMs loaded with G3139-GAP or a scrambled oligonucleotide, with MCMs not carrying ASO, and with ASO/lipofectamine complexes, and with untreated control cells (Figure 5.8 and Figure 5.9). Blots representing total cell extracts were probed with antibodies against BCL-2 and GAPDH as an internal loading control

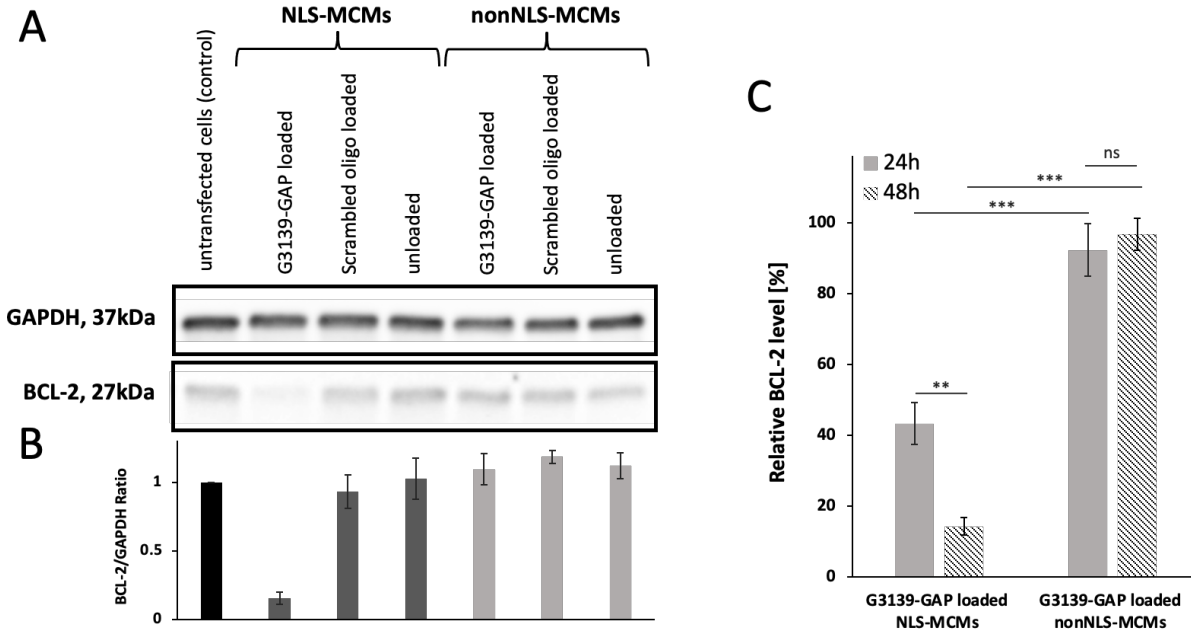


Figure 5.8: Therapeutic effects of NLS-MCMs delivering G3139-GAP ASO. A) Western blot analysis of BCL-2 proteins in $6\mu\text{g}$ of MCF-7 total cell extract after 48 h. GAPDH was used as loading control. B) Quantitative densitometry of the immunoblots; nonNLS-MCM-treated (light grey bars), NLS-MCM-treated (dark grey bars), untreated (black bar). C) BCL-2 expression levels in cells transfected with G3139-GAP relative to scrambled oligo delivered with NLS- or nonNLS MCMs. Data are mean \pm s.d. of the relative intensity of the bands from three independent assays (not significant (ns) $p > 0.05$, ** $p < 0.01$ and *** $p < 0.001$).

Comparison of cells transfected with cargo-free, 'empty' MCMs to untransfected cells (control) after 24 and 48 h showed that the nonNLS- and NLS-MCM platforms by themselves had no significant effect on BCL-2 levels. In contrast, when NLS-MCM nanocarriers were loaded with G3139-GAP, after 24 h, a 57% reduction in BCL-2 levels relative to cells transfected with

scrambled oligo-loaded NLS-MCMs was observed (Figure 5.8C). More importantly, after 48 h of treatment, nuclear targeting of G3139-GAP by NLS-MCMs led to 86% downregulation of BCL-2 levels relative to cells transfected with scrambled oligo-loaded NLS-MCMs (Figure 5.8C). In contrast, delivery of G3139-GAP by nonNLS-MCMs only reduced BCL-2 levels by 8 (after 24h) and 4% (after 48h) relative to cells transfected with scrambled oligo-loaded nonNLS-MCMs. These data show that the nuclear targeting of the nanocarriers and a corresponding release of G3139-GAP are essential for a significant decrease in BCL-2.

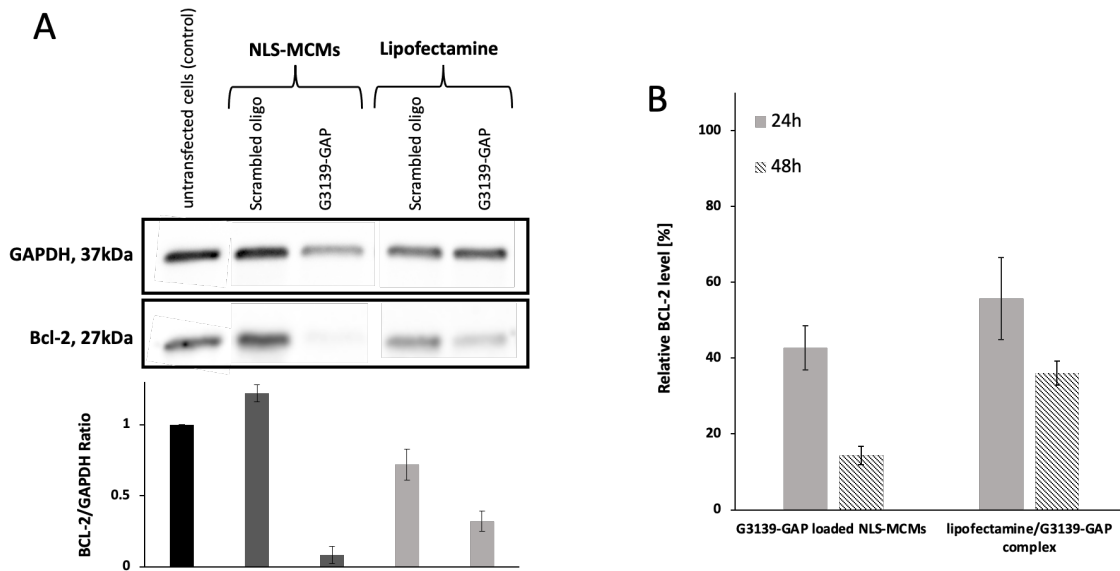


Figure 5.9 Therapeutic effects of cells transfected with lipofectamine/G3139-GAP complex. A) Western blot analysis of BCL-2 proteins in 6µg of MCF-7 total cell extract after 48 h. GAPDH was used as loading control. B) Quantitative densitometry of the immunoblots. Lipofectamine-treated (light grey bars), NLS-MCM-treated (dark grey bars), untreated (black bar). C) BCL-2 expression levels in cells transfected with G3139-GAP relative to scrambled oligo delivered with NLS-MCMs or lipofectamine complexes. Data are mean±s.d. of the relative intensity of the bands from three independent assays.

Notably, when compared to cells transfected with lipofectamine/G3139-GAP complexes relative to lipofectamine/scrambled oligo complexes at corresponding ASO concentrations, we

observed a more efficient BCL-2 reduction by G3139-GAP loaded NLS-MCMs (57% versus 45% after 24 h and 86% versus 63% after 48 h) (Figure 5.9 A,B). In a recent study, cell penetrating peptide (CPP) conjugated exosomes (EXOs) were used as a platform for ASO delivery ²⁴¹. Their western blot analysis revealed a decrease of 51.71% and 69.69% in BCL-2 levels by EXO-G3139 and EXO-R9-G3139 in HepG2 cells. In another example, a 70% downregulation in Bcl-2 mRNA was found in MCF-7 cells incubated with self-assembled peptide nanofibers for G3139 delivery ²⁴². In comparison, our peptidic platform with G3139-ASO payloads for BCL-2 protein downregulation displayed stronger downregulation effect after 48 h which suggest that NLS-MCMs are promising nanocarriers for efficient delivery of therapeutic oligonucleotides to the nucleus.

6 General Conclusion and Outlook

In this thesis, cationic amphiphilic peptides were designed for maximizing their potential for gene delivery applications. Peptides are particularly attractive building blocks for non-viral delivery platforms due to their biocompatibility and biodegradability which are critical properties for *in vivo* applications. Moreover, peptides offer diverse functional properties provided by a variety of interactions among the amino acids side chains. The peptide sequences described in this thesis combine truncated gramicidin A (gT) repeats as the hydrophobic domain combined with a rational design of positively charged amino acids comprising the hydrophilic domain. The gT sequence consists of highly hydrophobic L-tryptophan-D-leucine [_LW-_DL] repeats, displaying a β -turn secondary structure in aqueous solution. The hydrophilic domain can be tailored to exhibit specific properties and/or intended functionalities, e.g by selecting defined combinations of positively charged histidine, arginine and lysine residues. Our study demonstrates that the combination of positively charged amino acids plays a role not only in the electrostatic interactions with oligonucleotides but also strongly influence the performance of non-viral vectors in physiologically relevant environments due to their chemical characteristics.

We first produced purely peptidic nanoparticles that efficiently entrapped single- and double-stranded DNA sequences of different lengths. We showed that peptides hierarchically self-assemble and finally form multicompartments micelles, have the capacity to embed various oligonucleotides between their segregated hydrophilic compartments with high loading efficiency. By incorporation of histidine-arginine moieties to the hydrophilic domain, the amphiphilic peptide (HR)3gT was designed to condense nucleic acid payloads while the hydrophobic core constituted the main driving force for self-assembly. Based on rational design of these desired features, individual peptide chains were able to form DNA-loaded noncytotoxic peptide nanoparticles by a

one-step self-assembly process. Nanoparticles loaded with ssDNA or dsDNA of either 22 and 100 nucleotides in length ranged between 100-180 nm in diameter and showed good colloidal stability at 4°C over months, both of which are essential attributes for biomedical applications. In addition, all types of DNA-loaded nanoparticles demonstrated high loading efficiency and eventually released the payloads at 37°C in response to temperature. In addition, by virtue of the (HR)₃ residues, this novel delivery system is prone to be rapidly and effectively taken up by cells.

The second part of the thesis centers around integrating KRKR, a minimal NLS, into the amphiphilic peptide backbone to achieve targeting of genetic materials to the nucleus in addition to enhancing cellular uptake efficiency by the extra positive charge. DNA delivery to the nucleus, especially when non-viral vectors are used, is a crucial step to ensure genome editing and modification of gene expression. The direct integration of (KR)₂ in the self-assembling peptide represents a novelty in non-viral vector delivery systems. More importantly, introducing the NLS-targeting moiety as part of the amphiphilic peptide sequence averts additional conjugation steps in the preparation of nanoparticles. The successful production of NLS-functionalized, DNA-loaded superstructures through a single-step self-assembly process highlights the versatility of hierarchical self-assembly as elegant approach to developing desirable properties and functions. Following extensive physicochemical characterization of self-assembled NLS-NPs, we applied several state-of-the-art methods to verify that (i) DNA-loaded NLS-NPs are taken up by cells more efficiently than corresponding NPs lacking an NLS (non-NLS-NPs), (ii) the NLS mediates interactions of the NPs with the nuclear translocation machinery, and (iii) DNA-loaded NLS-NPs successfully ferry DNA to the nucleus. In addition, our findings reveal that the NLS-NPs with an average size of 90nm, dissociated to smaller multicompartment micelles in response to physiological temperature which further facilitated their transport through the nuclear pore. Most

importantly, findings with ASO payloads that resulted in up to 86% knockdown of BCL2, an inhibitor of apoptosis that is overexpressed in more than half of all human cancers suggest that NLS-MCMs are suitable nanovectors for delivering therapeutic oligonucleotides to the nucleus. The unprecedented combination of a straightforward manner of production, non-cytotoxicity and efficient DNA delivery to the nucleus makes our purely peptidic platform superior to established nanocarriers.

In summary, the present dissertation demonstrates that by rational design of peptides we can realize self-assembling multifunctional, biocompatible and biodegradable nanostructures. A particular advantage of purely peptidic nanoassemblies is, that functionality can be directly integrated in the peptide sequence provided the effect of the functional amino acids on the secondary structure and self-assembly behavior are taken into account. Our findings suggest that the platform presented in this Thesis has the potential to be further developed for systemic gene therapy and vaccination applications. The data from cell studies encourage *in vivo* studies of the the peptidic nanoparticles in order to explore their biological and pharmacological aspects. We envisage that our strategy to use self-assembled peptide nanoparticles as DNA carriers can be extended to the delivery of the diverse oligonucleotide cargos including mRNA, siRNA and ASO. Furthermore, vector functionalities could be broadened by developing a stimuli-responsive peptide for triggered delivery of cargo, or by incorporating an MRI contrast agent which converts the self-assembled nanoparticles from a delivery to a theranostic system. Finally, additional conjugation of specific targeting moieties, e.g. antibodies recognizing cell- or tissue-specific markers, to the surface of our peptidic nanocarrier would allow targeting and release of payloads at the disease site while minimizing off-target effects. A detailed understanding of such purely peptide-based platforms is prerequisite for their tuning such as to obtain properties that are desired for biomedical

applications, specifically for gene therapy. The presented work unveils the great potential of amphiphilic peptide self-assembly into higher ordered nanostructures and functional platforms for a broad range of biomedical applications.

7 Material and Methods

7.1 Materials

Solvents and reagents were purchased from Sigma-Aldrich unless otherwise specified. Triisopropylsilane, piperidine and N,N'-diisopropylcarbodiimide (DIC) were of synthesis grade. Rink Amide AM resin (0.71 mmol/g) and Fmoc-Trp(Boc)-OH were purchased from IRIS Biotech GmbH. All other Fmoc-protected amino acids and ethyl cyano(hydroxyimino)acetate (Oxyma Pure) were purchased from Novabiochem. Dimethylformamide (DMF) was purchased from J.T. Baker. Dichloromethane (DCM) and acetonitrile (ACN) were purchased from VWR chemical. Solvent exchange was performed in dialysis tubes from Spectrum Laboratories (cellulose ester, MWCO 500–1000 Da, 3.2 cm/mL). Atto550 was purchased from ATTO-TEC GmbH. Atto550-labeled and unlabeled 18 nucleotide (nt) G3139, 18nt G3139-GAP, 22nt and 100nt DNA and their unlabeled complementary stands and unlabeled scrambled non-specific sequence were purchased from Microsynth. The oligonucleotide sequences are provided in Table 6.1. All cysteine-tagged FG domains of human nucleoporins, Nup62, Nup214 and exogenous proteins, such as human Kap β 1, Kap α , wild-type Ran (RanWT) were provided by Lim Lab after cloning, expression and SDS PAGE purification as described previously^{267,268}. Fetal calf serum (FCS) and phosphate buffer saline (PBS) was purchased from BioConcept. Live cell imaging solution was obtained from Thermo Fisher Scientific. Dulbecco's modified eagle medium (DMEM), Opti-MEM, and Pen/Strep were obtained from Gibco life technologies. CellTiter 96 AQueous One Solution Cell Proliferation Assay (MTS) was purchased from Promega.

Table 7.1 Sequence of oligonucleotides.

	oligonucleotide sequence
18nt G3139	5'-T*C*T*C*C*C*A*G*C*G*T *G*C*G*C*C*A*T-3' * Fully phosphorothioate substitutes For the labeled batch, Atto550 conjugation to the 5' end
18nt G3139-GAP	5'-8*6*8*C*C*C*A*G*C*G*T *G*C*G*C*6*5*8-3' * Fully phosphorothioate substitutes 5 = 2OMeA, 6 = 2OMeC, 8 = 2OMeU For the labeled batch, Atto550 conjugation to the 5' end
Scrambled non-specific sequence	5'-G*T *G* A*T *A* C*C *T* C*C *G* T*C *C* G*C *C-3' * Fully phosphorothioate substitutes
22nt ssDNA	5'-TAA CAG GAT TAG CAG AGC GAG G-3' For the labeled batch, Atto550 conjugation to the 5' end
22nt ssDNA complementary strand	5'-CCT CGC TCT GCT AAT CCT GTT A-3'
100nt ssDNA	5'-AAA CTC CAA CCA AAA CCT CCT CCC CCA CCC TAA CTC ATT ATC CCC CCT TAC CCA TTT ACC CCA ACA CAC CAA CCT CCC AAC AAC CTC CCT CCA CCA ACC A-3' For the labeled batch, Atto550 conjugation to the 5' end
100nt ssDNA complementary strand	5'-TGG TTG GTG GAG GGA GGT TGT TGG GAG GTT GGT GTG TTG GGG TAA ATG GGT AAG GGG GGA TAA TGA GTT AGG GTG GGG GAG GAG GTT TTG GTT GGA GTT T-3'

7.1.1 Peptide Synthesis and Purification

(KR)₂(HR)₂gT peptide consists of 23 amino acids (AA), H_2N -[K-R]₂-[H-R]₂-[W-DL]₇-W-NH₂, (with DL = D-Leucine), (HR)₃gT peptide consists of 19 AA, H_2N -[H-R]₃-[W-DL]₆-W-NH₂, and the previously reported H3gT of 10 AA, H_2N -[H]₃-[W-DL]₃-W-NH₂⁵⁰. All peptides

were synthesized using Liberty Blue™ automated microwave peptide synthesizer (CEM, Kamp-Lintfort, Germany). The synthesis was performed on a rink amide resin using standard fluorenylmethoxycarbonyl (Fmoc) solid phase peptide synthesizer chemistry and DIC/OXYMA coupling protocols. After completing synthesis in the Liberty Blue™ synthesizer, the peptidyl resin was collected and washed alternately with DMF and dichloromethane. Peptides were manually cleaved from the resin by 5 mL trifluoroacetic acid (TFA) under gentle agitation over a period of 2 h at room temperature in the presence of scavengers (standard cleavage solution: TFA/triisopropylsilane (TIPS)/Water 95:2.5:2.5). The cleavage cocktail was filtered and the resin was washed with 1 mL cleavage solution. The peptides were precipitated from the combined cleavage solution by the addition of 40 mL cold diethyl ether and pelleted by centrifugation at 4500 rpm for 3 min at 4°C. The pellet together with supernatant were incubated at -20°C for 1 h and again centrifuged under the same conditions and supernatant was discarded. The pellet was dissolved in ACN/H₂O (1:1) and TFA (0.05%, v/v) solution. The crude peptide was filtered and lyophilized.

Purification of the crude (KR)2(HR)2gT and (HR)3gT peptides was carried out by reversed phase high performance liquid chromatography (RP-HPLC) (Prominence 20A, Shimadzu, Japan) on a C18 (RP18e, 100 mm × 10 mm, Merck Chromolith, Germany) column whereas H3gT peptide was purified on a C18-TSE column (VDSpher OptiBio PUR 300 C18-TSE, 20 x 250mm, VDS Optilab, Germany). A mobile phase of water and acetonitrile containing 0.1% TFA with a gradient of 35-50% ACN over 40 min for (KR)2(HR)2gT, a gradient of 25-60% ACN over 30 min for (HR)3gT and 20-65% ACN over 30 min for H3gT was used to separate peptides. Peptide purification was monitored at 280 nm. Fractions of purified peptides were collected, lyophilized and stored at -20 °C. The molecular mass of each peptide was determined by PerSeptive

Biosystems Voyager-DE-PRO time-of-flight mass spectrometer (MALDI-TOF-MS) in positive mode. Peptides were characterized by analytical high performance liquid chromatography (HPLC) and (MALDI-TOF) mass spectroscopy before and after purification.

7.2 Methods

7.2.1 Self-assembly of Peptide Nanoparticles

For self-assembly of empty and DNA-loaded peptide nanoparticles, a 1 mg/mL peptide stock solution was prepared in 50/50 ethanol/water from the respective lyophilized peptide and filtered through a 0.2 μm hydrophilic syringe filter. Self-assembly was achieved via the solvent exchange method by dialysing the organic solvent (ethanol) against milli-Q H_2O (Merck Millipore, Milli-Q Direct 8 water purification system). For loading nanoparticles with DNA, the following synthetic DNA cargoes were prepared at a concentration of 100 μM in water: 5'Atto550-labeled 22nt and 100nt single-stranded DNA (22nt ssDNA / 100nt ssDNA), and 22 and 100 base pair double-stranded DNA (22bp dsDNA / 100bp dsDNA) with one 5'Atto550-labeled strand (**Table 6.1**). In order to form DNA-loaded peptide nanoparticles, 100 μL of peptide stock solution (1mg / mL) were mixed with 3 μg of DNA (100 μM solution). The DNA-peptide mixture was then adjusted to a final volume of 500 μL in a final concentration of 35% ethanol and transferred to a prewashed 500–1000 MWCO dialysis tube. The self-assembly was induced by dialysis at 4°C for approximately 20 h against two changes of 500mL ultrapure DNase/RNase-free distilled water. To prepare the control nanoparticles without DNA, peptide solutions were diluted to a concentration of 0.2 mg/mL in a corresponding final ethanol concentration and subsequently dialyzed under the same conditions.

7.2.2 Dynamic Light Scattering

The mean hydrodynamic diameter (z-average) and polydispersity index (PDI) of the self-assembled peptide nanoparticles were determined by dynamic light scattering (DLS) at a wavelength of 633 nm at 25°C with an angle detection of $\theta = 173^\circ$ using a Zeta Sizer Nano ZSP (Malvern Instruments Ltd., UK). All measurements were performed in triplicate.

7.2.3 Zeta-potential

For measuring the zeta-potential by Zeta Sizer Nano ZSP (Malvern Instruments Ltd., UK), 500 μL of self-assembled peptide nanoparticles in water were added to a cuvette and the zeta-potential recorded after each polyelectrolyte deposition. Zeta potential data represent the mean of three consecutive measurements.

7.2.4 Transmission Electron Microscopy

For transmission electron microscopy (TEM), aliquots of self-assembled peptide nanoparticles were deposited on a glow-discharged, carbon-coated, parlodion-(2% in n-butyl acetate) copper grid and adsorbed for 2 min. Excess liquid was blotted with a filter paper and grids were negatively stained for 10s with 5 μL 2% uranyl acetate, washed 3 times with water and dried. Grids were examined with a CM100 transmission electron microscope (Philips, Eindhoven, The Netherlands) operated at an accelerating voltage of 80 kV.

7.2.5 Cryogenic Electron Microscopy

Four microliters of self-assembled peptide nanoparticles were adsorbed onto glow discharged carbon-coated grids (Lacey, Tedpella, USA). Excess sample was blotted off with grade 1 Whatman filter paper for seconds to produce a thin aqueous film, which is subsequently vitrified by plunge freezing. Frozen grids were transferred at -178°C into a Gatan 626 cryoholder and imaged by Talos electron microscope (FEI, USA). Electron micrographs were recorded at an

accelerating voltage of 200 kV while keeping the sample at low temperatures. Resulting cryo-EM micrographs were recorded on a CETA camera (4096 × 4096 pixels; Thermo Fisher).

7.2.6 Nanoparticle Tracking Analysis

Nanoparticle tracking analysis (NTA) was performed using a NanoSight NS 300 instrument (NanoSight Ltd, Amesbury, UK) equipped with a 532-nm laser. NTA software calculates the size based on tracking the Brownian motion of the particles and using the velocity of the particle movement to apply into the 2D Stokes-Einstein equation. Self-assembled peptide nanoparticles were diluted 20-fold and delivered to the viewing chamber using a 1 mL syringe. For each measurement, three videos of 60 s were captured at room temperature. Particle movement was analysed by the NTA software (version 3.4, NanoSight) based on tracking each particle on a frame-by-frame basis in order to give the mean and median particle size together with the estimated concentration of nanoparticles in solution. To determine DNA loading efficiency, NTA data for each Atto550-DNA loaded peptide nanoparticles was recorded under scatter and fluorescence mode. The NTA acquisition settings were kept constant between measurements.

7.2.7 Fluorescence Correlation Spectroscopy

Fluorescence correlation spectroscopy (FCS) experiments were performed at 20°C on a Zeiss LSM 880 laser-scanning microscope equipped with a 40x water immersion objective (C-Apochromat 40x, NA 1.2) (Carl Zeiss, Jena, Germany). For each measurement, 10 µL of sample (Atto550-dye, Atto550-labeled DNA in solution and Atto550-DNA-loaded peptide nanoparticles) were placed on a 22 × 50 mm glass slide. Measurements were performed using a helium/neon laser for 561 nm excitation, set at 0.25% laser power, a 488/561/633 main beam splitter (MBS), and a pinhole size of 40 µm.

Fluorescence signals were measured in a real time (5s with 30 repetitions) and autocorrelation function was obtained by a QuickFit 3.0 software calculator. For determining the DNA entrapment in peptide MCM-NPs, experimental auto correlation curves were fitted to a two-component model including triplet state with a structural parameter of 5 (Eq. 1) ^{175,269,270}.

$$G(\tau) = 1 + \left(1 + \frac{T}{1-T} e^{-\tau/\tau_{trip}}\right) \frac{1}{N} \left(\frac{f_1}{1 + \frac{\tau}{\tau_{D1}} \sqrt{1 + R^2 \frac{\tau}{\tau_{D1}}}} + \frac{f_2}{1 + \frac{\tau}{\tau_{D2}} \sqrt{1 + R^2 \frac{\tau}{\tau_{D2}}}} \right) \quad (1)$$

Where, τ_{D1} and τ_{D2} are the diffusion time and f_1 and f_2 are the fraction of the corresponding component, Atto550-labeled free DNA and Atto550-labeled DNA entrapped inside the peptide MCM-NPs, respectively. T is the fraction of fluorophores in triplet state with triplet time τ_{trip} , N is the average number of particles in the confocal volume and R is the structural parameter (fixed to 5).

For the three-dimensional (3D) Gaussian-shaped observation volume (V_{obs}), identical fluorescent species with the volume much smaller than V_{obs} can move in and out of it. The autocorrelation function ($G(\tau)$) of the fluorescent specie is determined with Eq.2 ^{175,269,270}.

$$G(\tau) = \frac{1}{N} \left(1 + \frac{\tau}{\tau_D}\right)^{-1} \left(1 + \left(\frac{r}{l}\right)^2 \left(\frac{\tau}{\tau_D}\right)\right)^{-1/2} \quad (2)$$

where r and l are the radial and axial length of the observation volume, respectively. The diffusion time τ_D of the species can then be related to the diffusion coefficient D by Eq.3 ^{175,269,270}.

$$\tau_D = \frac{r^2}{4D} \quad (3)$$

With the diffusion coefficient of the fluorescent species and its concentration (N/ V_{obs}) in a diluted sample, finally the hydrodynamic radius (R_h) of the fluorescent species can be calculated using the Stokes-Einstein equation ^{175,269,270}.

$$R_h = \frac{kT}{6\pi\eta D} \quad (4)$$

where k is the Boltzmann constant, T temperature and η the viscosity of the solution.

7.2.8 SPR

Surface Plasmon Resonance (SPR) spectroscopy was used to evaluate Kap α .Kap β 1.NLS-MCMs interactions with FG Nups (Nup62, Nup214). All SPR binding assays were performed at 25°C in HEPES (0.025M) with 5mM MgCl₂, using a four flow cell BiacoreT200 instrument (GE Healthcare), as described previously^{267,271}. Briefly, HS-(CH₂)₁₁-(OCH₂-CH₂)₃-OH (abbreviated as PUT, Nanoscience) and cysteine-terminated FG Nups were conjugated to a gold sensor chip in cell 1 (as a non-specific reference) and in cell 2 (with the samples). 1% (wt/vol) BSA (Sigma-Aldrich) solution was prepared in HEPES (0.025M) with 5mM MgCl₂, pH 7.2 as a running buffer. All proteins and peptide nanoparticles were dialyzed against the same buffer before the experiment. Ten titrations at a ratio of 10 to 1 increasing by a factor 2 of Kap α to Kap β 1 to a maximum concentration of 400 nM Kap β 1 and 800 nM Kap α were prepared. The ratio of NLS and non-NLS peptides to Kap α .Kap β 1 was kept constant by mixing each Kap α .Kap β 1 solution with a factor 2 increase, terminating with a maximum concentration of 200 nM of NLS and non-NLS peptides (for 400 nM Kap β 1 and 800 nM Kap α). Before being injected, buffer solutions were filtered (0.22 μ m) and degassed and all samples, protein and reagent solutions were centrifuged for 15 min at 12000 rpm to remove particles and bubbles. The binding data were analyzed using Biacore T200 Control software.

7.2.9 Thermo-responsiveness of Peptide Nanoparticles

To analyze the temperature response of self-assembled peptide nanoparticles, 200 μ L of empty and DNA-loaded peptide nanoparticles were diluted two-fold and incubated at 37 °C for the times indicated. Nanoparticles size and morphology were examined by DLS and TEM before incubation and at the time points indicated.

7.2.10 Cell Culture

HeLa and Histone H2B-GFP expressing HeLa, and MCF-7 human breast carcinoma cell lines were routinely subcultured in DMEM with 1x Glutamax-I (4.5g/L glucose; Gibco) supplemented with 10% fetal calf serum (FCS; BioConcept). A549 human lung carcinoma and THP-1 human leukemia monocytic cell lines were cultured in RPMI-1640 (BioConcept) supplemented with 10% FBS and 1x GlutaMAX (Gibco). All cells were cultured at 37 °C in a humidified atmosphere with 5% CO₂ up to maximum 25 passages. For incubation with MCMs, media were supplemented with 1x Penicillin-Streptomycin (Gibco).

7.2.11 MTS Cell Viability Assay

Cytotoxicity of peptide nanoparticles was evaluated by cell proliferation assays using tetrazolium compound-based Cell Titer 96® AQueous One Solution Cell Proliferation (MTS) assay (Promega). MTS assays were performed according to the manufacturer's instructions after 24 hours of treatment with peptide nanoparticles. In brief, HeLa cells were seeded in a 96-well plate at 3×10^3 cells in 100 μ L DFCS/well on the day prior to nanoparticle treatment. Subsequently, DNA-loaded H3gT, (HR)3gT and (KR)2(HR)2gT peptide nanoparticles and nanoparticles without DNA-payload were added to each well to a final peptide concentration of 50, 300, 550, 800, 1050, 1300, 1550 μ g/ml. In the MTS assay for (KR)2(HR)2gT peptide nanoparticles, lipofectamine-DNA complex as the gold standard for transfection was included at the highest peptide concentration (corresponding to 1550 μ g peptide /ml and 96ng DNA) to compare the cytotoxicity. Untreated cells were used as a reference value for 100% viability. After 24 h of incubation at 37°C, 20 μ l of MTS solution were added to each well, and the plate incubated for 2 h at 37 °C. The absorbance of the plate was then read at $\lambda = 490$ nm using a Spectramax plate reader (Molecular Devices LLC, USA). Background absorbance of wells without cells was subtracted from all test

wells. The viability in treated wells was determined by normalizing the absorbance to that of untreated control cells. All experiments were performed in triplicate wells for each condition and repeated at least twice.

7.2.12 Cellular Uptake of Peptide Nanoparticles

For nanoparticle uptake experiments, 3×10^4 cells per well were seeded in an eight-well glass-bottom μ -slide (Ibidi, Germany) and cultured for 24 h before equal concentrations of H3gT, (HR)3gT and (KR)2(HR)2gT peptide nanoparticles (determined by NTA) were added to each well, except for THP-1 which were induced to differentiate into macrophages by adding $xy \text{ ng/ml}$ of phorbol 12-myristate 13-acetate (PMA) for 48 h. Cells were imaged on a confocal laser-scanning microscope (CLSM) (Zeiss LSM 880 880 IndiMo, Carl Zeiss Inc. Thornwood, NY) at 5, 24 and 48 h using the same image acquisition settings for treated and untreated cells. Furthermore, cells treated with 100bp dsDNA were imaged over 42 h under live cell conditions (37°C, 5% CO₂).

7.2.13 Protein Extraction

1.5×10^5 cells per well were seeded in a 6-well plate and incubated overnight before after addition of ASO-loaded MCMs or control MCMs for 48h. After rinsing cells three times with ice-cold PBS, 400 μ l of RIPA buffer (Merck) containing a protease inhibitor cocktail (ThermoFisher) were added to each well and cells gently scraped off the surface using a rubber cell scraper. Cell lysates were then transferred to 1.5 ml Eppendorf tubes and incubated for 30 minutes at 4 °C with constant agitation. The cell lysates were spun for 20 min at 12,000 rpm at 4 °C. The protein containing supernatant was gently transferred to a fresh tube. Protein concentrations were determined using Pierce™ bicinchoninic acid (BCA) Protein Assay Kit (ThermoFisher). The lysates were aliquoted and stored at -80 °C.

7.2.14 Evaluation of Bcl-2 Protein Expression by Western Blotting

Aliquots of protein extracts normalized for total protein concentration according to the BCA assay were denatured in Laemmli sample buffer (ThermoFisher) and loaded onto any kD™ mini-PROTEAN® TGX™ precast protein gels (Bio-Rad). Proteins were resolved by SDS-polyacrylamide gel electrophoresis and electrophoretically transferred onto trans-blot turbo mini prewetted PVDF membranes (Bio-Rad) according to the manufacturer's instructions. The membrane was blocked with 3% bovine serum albumin (BSA) in PBS/ 0.1% Tween 20 (PBST) for 2 h at room temperature with gentle agitation. The membrane was then incubated with either 1:500 dilution monoclonal mouse anti-human Bcl-2 (ThermoFisher; Cat. no. 13-880) or 1:500 dilution polyclonal rabbit anti-human Bcl-2 (Bio-Rad; Cat. no. VPA00775) together with 1:1000 dilution polyclonal rabbit anti-human GAPDH antibody (Bio-Rad; Cat. no. VPA00187) at 4°C overnight with gentle agitation. After washing the blot three times for 5 minutes with TBST, the membranes were probed with secondary horseradish peroxidase (HRP)-conjugated goat anti-rabbit IgG (Azure, Cat. no. AC2114) or goat anti-mouse IgG (Azure, Cat. no. AC2115) at 1:10,000 dilution for 1 h at room temperature. The membranes were then washed three times for 5 minutes with TBST and soaked in HRP chemiluminescence substrate (Radiance Plus solution, Azure) for 30 seconds to detect the secondary HRP conjugates. Western blotting images were acquired on an Azure Sapphire Biomolecular Imager. The bands were analyzed by Image Lab software from Bio-Rad.

7.2.15 Ultrastructural Analysis of Peptide Nanoparticles in Cells

HeLa cells (8×10^5 cells) were seeded in 100 mm × 15 mm round culture dishes (Thermo Fisher) and grown in DMEM supplemented with 10% FCS. After 24h, $1.28 \times 10^7 \pm 4.28 \times 10^6$ of DNA-loaded (KR)₂(HR)₂gT and (HR)₂gT peptide nanoparticles (determined by NTA) were added to each culture dishes. One plate was left untreated as control. Cells were incubated for 16

h at 37 °C in 5% CO₂ and then washed four times with PBS. Cells were fixed with 1:1 (v/v) medium-fixative (double strength) mixture (the single strength fixative solution consists of 2.5% glutaraldehyde + 2% paraformaldehyde in 0.1M PIPES buffer, pH 7) for 20min at room temperature, harvested with cell scraper and pelleted by centrifugation at 300 rpm for 5 min at room temperature. Cell pellets were then suspended in single strength fixative for 1h at 4 °C, then washed with 0.1M sodium cacodylate buffer three times and embedded in low melting 2% agarose. Once solidified agarose pellets were trimmed into 1-2 mm cubes, they were post-fixed in 1% buffered osmium tetroxide for 1h at 4 °C, rinsed in distilled water, and finally stained *en bloc* with aqueous 1% uranyl acetate for 1hr at 4 °C in the dark. Cubes were then dehydrated in an ethanol series (30, 50, 75, 95% and 100%). After three changes of absolute ethanol, samples were washed in acetone and finally embedded in a mixture of resin (EPON812)/acetone followed by pure Epon 812 resin. Ultra-thin sections (50-70nm thick) were cut and mounted on grids according to the regressive EDTA staining protocol²⁷². In brief, the ultrathin sections were floated in a 6% aqueous uranyl acetate solution for 5 min. Thereafter, sections were rinsed with double distilled water (H₂O_{dd}) and a second floating step in 0.2 M EDTA in H₂O_{dd}, pH 7.0 was performed. The sections were rinsed again with H₂O_{dd} and stained with lead citrate for 5 min. After the final rinsing step with H₂O_{dd}, sections were imaged on a FEI Tecnai T12 Transmission Electron Microscope operating at an accelerating voltage of 120 kV. Micrographs were recorded using a TVIPS F416 CMOS digital camera (bottom mounted).

7.2.16 Statistical Analysis of Localized MCMs under live cell conditions

Histone H2B-GFP expressing HeLa cells (3x10⁴ cells per well) were seeded in DMEM medium supplemented with 10% FCS on an eight-well glass-bottom μ -slide (Ibidi, Germany). After culturing for 24h, $3.22 \times 10^8 \pm 6.65 \times 10^7$ of NLS and non-NLS peptide nanoparticles

(determined by NTA) were added to each well. The 8-well slide was immediately mounted on a microscope stage equipped with CO₂ chamber and heating module (37°C, 5% CO₂) for live cell confocal imaging. Samples were excited with 488 nm (green) and 561 nm (red) laser lines. Images were obtained with a C-Apochromat 40x /1.2 NA Korr FCS M27 water-immersion objective at an image acquisition resolution of 2048 x 2048 pixels. Pinhole diameters were set to 1 airy unit and at each timepoint, Z-stacks were captured with z-resolution of 0.26 µm. To statistically evaluate the NLS-peptide nanoparticle translocation to the nucleus, treated cells were imaged at 5, 10, 36, and 48h. Image stacks were analyzed using IMARIS 9.2 software (Bitplane AG, Switzerland) on a per pixel basis. Accordingly, 3D Imaris reconstructions from multiple Z-stacks were created to identify and quantify peptide nanoparticles inside and on the membrane of the nucleus. Based upon the fluorescence of the objects, the Atto550-DNA-loaded peptide nanoparticles were identified as 'spots' and Histone H2B-GFP expressing nuclei as 'surfaces'. Quantification of peptide nanoparticles in each image stack was performed using the SPOTS option of the IMARIS software. SPOTS option allows the detection and visualization of spherical objects in each image stack defining their X, Y and Z axial positions, size and signal intensity²⁷³. Colocalization analysis of peptide nanoparticles and nuclei was performed on confocal image Z-stacks using the IMARIS distance to surface feature. Nanoparticles detected within ± 0.1 µm distance to the nuclear envelope were considered associated with the nuclear membrane. Nanoparticles with a distance below 0.1 µm to the nuclear membrane were considered to be inside the nucleus. Student's two-tailed t-test was used to demonstrate the significance of the statistical difference between NLS and non-NLS nanoparticles. A p value ≤ 0.05 was considered significant. The number of analyzed nuclei for 5, 10, 36 and 48 h timepoints were 38, 44, 78, 98 and 41, 41, 78, 116 for non-NLS and NLS nanoparticles, respectively. Particle counting was carried out with IMARIS 9.2 software.

References

- (1) Naldini, L. Gene Therapy Returns to Centre Stage. *Nature* **2015**, 526 (7573), 351–360. <https://doi.org/10.1038/nature15818>.
- (2) Thomas, C. E.; Ehrhardt, A.; Kay, M. A. Progress and Problems with the Use of Viral Vectors for Gene Therapy. *Nat. Rev. Genet.* **2003**, 4 (5), 346–358. <https://doi.org/10.1038/nrg1066>.
- (3) Ginn, S. L.; Alexander, I. E.; Edelstein, M. L.; Abedi, M. R.; Wixon, J. Gene Therapy Clinical Trials Worldwide to 2012 – an Update. *J. Gene Med.* **2013**, 15 (2), 65–77. <https://doi.org/10.1002/jgm.2698>.
- (4) Kang, Z.; Meng, Q.; Liu, K. Peptide-Based Gene Delivery Vectors. *J. Mater. Chem. B* **2019**, 7 (11), 1824–1841. <https://doi.org/10.1039/C8TB03124J>.
- (5) Tarvirdipour, S.; Huang, X.; Mihali, V.; Schoenenberger, C.-A.; Palivan, C. G. Peptide-Based Nanoassemblies in Gene Therapy and Diagnosis: Paving the Way for Clinical Application. *Molecules* **2020**, 25 (15), 3482. <https://doi.org/10.3390/molecules25153482>.
- (6) Lombardo, D.; Kiselev, M. A.; Magazù, S.; Calandra, P. Amphiphiles Self-Assembly: Basic Concepts and Future Perspectives of Supramolecular Approaches <https://www.hindawi.com/journals/acmp/2015/151683/> (accessed 2021 -01 -12). <https://doi.org/10.1155/2015/151683>.
- (7) Wang, L.; Gong, C.; Yuan, X.; Wei, G. Controlling the Self-Assembly of Biomolecules into Functional Nanomaterials through Internal Interactions and External Stimulations: A Review. *Nanomaterials* **2019**, 9 (2). <https://doi.org/10.3390/nano9020285>.
- (8) Rocha, B. C.; Paul, S.; Vashisth, H. Role of Entropy in Colloidal Self-Assembly. *Entropy* **2020**, 22 (8), 877. <https://doi.org/10.3390/e22080877>.
- (9) ISRAELACHVILI, J. N. Thermodynamic and Geometric Aspects of Amphiphile Aggregation into Micelles, Vesicles and Bilayers, and the Interactions between Therm. *Proc Int Sch. Phys Enrico Fermi Course XC* **1985**.
- (10) Yorulmaz Avsar, S.; Kyropoulou, M.; Di Leone, S.; Schoenenberger, C.-A.; Meier, W. P.; Palivan, C. G. Biomolecules Turn Self-Assembling Amphiphilic Block Co-Polymer Platforms Into Biomimetic Interfaces. *Front. Chem.* **2019**, 6, 645. <https://doi.org/10.3389/fchem.2018.00645>.
- (11) Ariga, K.; Nishikawa, M.; Mori, T.; Takeya, J.; Shrestha, L. K.; Hill, J. P. Self-Assembly as a Key Player for Materials Nanoarchitectonics. *Sci. Technol. Adv. Mater.* **2019**, 20 (1), 51–95. <https://doi.org/10.1080/14686996.2018.1553108>.
- (12) Mendes, A. C.; Baran, E. T.; Reis, R. L.; Azevedo, H. S. Self-Assembly in Nature: Using the Principles of Nature to Create Complex Nanobiomaterials. *WIREs Nanomedicine Nanobiotechnology* **2013**, 5 (6), 582–612. <https://doi.org/10.1002/wnan.1238>.
- (13) Ramanathan, M.; Shrestha, L. K.; Mori, T.; Ji, Q.; Hill, J. P.; Ariga, K. Amphiphile Nanoarchitectonics: From Basic Physical Chemistry to Advanced Applications. *Phys. Chem. Chem. Phys.* **2013**, 15 (26), 10580–10611. <https://doi.org/10.1039/C3CP50620G>.
- (14) Dehsorkhi, A.; Castelletto, V.; Hamley, I. W. Self-Assembling Amphiphilic Peptides. *J. Pept. Sci.* **2014**, 20 (7), 453–467. <https://doi.org/10.1002/psc.2633>.
- (15) Panda, J. J.; Chauhan, V. S. Short Peptide Based Self-Assembled Nanostructures: Implications in Drug Delivery and Tissue Engineering. *Polym. Chem.* **2014**, 5 (15), 4418–4436. <https://doi.org/10.1039/C4PY00173G>.

- (16) Santis, E. D.; Ryadnov, M. G. Peptide Self-Assembly for Nanomaterials: The Old New Kid on the Block. *Chem. Soc. Rev.* **2015**, *44* (22), 8288–8300. <https://doi.org/10.1039/C5CS00470E>.
- (17) Acar, H.; Srivastava, S.; Chung, E. J.; Schnorenberg, M. R.; Barrett, J. C.; LaBelle, J. L.; Tirrell, M. Self-Assembling Peptide-Based Building Blocks in Medical Applications. *Adv. Drug Deliv. Rev.* **2017**, *110–111*, 65–79. <https://doi.org/10.1016/j.addr.2016.08.006>.
- (18) Zhao, X.; Pan, F.; Xu, H.; Yaseen, M.; Shan, H.; Hauser, C. A. E.; Zhang, S.; Lu, J. R. Molecular Self-Assembly and Applications of Designer Peptide Amphiphiles. *Chem. Soc. Rev.* **2010**, *39* (9), 3480–3498. <https://doi.org/10.1039/B915923C>.
- (19) Löwik, D. W. P. M.; Hest, J. C. M. van. Peptide Based Amphiphiles. *Chem. Soc. Rev.* **2004**, *33* (4), 234–245. <https://doi.org/10.1039/B212638A>.
- (20) Chen, J.; Zou, X. Self-Assemble Peptide Biomaterials and Their Biomedical Applications. *Bioact. Mater.* **2019**, *4*, 120–131. <https://doi.org/10.1016/j.bioactmat.2019.01.002>.
- (21) Qi, G.-B.; Gao, Y.-J.; Wang, L.; Wang, H. Self-Assembled Peptide-Based Nanomaterials for Biomedical Imaging and Therapy. *Adv. Mater.* **2018**, *30* (22), 1703444. <https://doi.org/10.1002/adma.201703444>.
- (22) Saccardo, P.; Villaverde, A.; González-Montalbán, N. Peptide-Mediated DNA Condensation for Non-Viral Gene Therapy. *Biotechnol. Adv.* **2009**, *27* (4), 432–438. <https://doi.org/10.1016/j.biotechadv.2009.03.004>.
- (23) Yadav, S.; Sharma, A. K.; Kumar, P. Nanoscale Self-Assembly for Therapeutic Delivery. *Front. Bioeng. Biotechnol.* **2020**, *8*. <https://doi.org/10.3389/fbioe.2020.00127>.
- (24) Wang, J.; Liu, K.; Xing, R.; Yan, X. Peptide Self-Assembly: Thermodynamics and Kinetics. *Chem. Soc. Rev.* **2016**, *45* (20), 5589–5604. <https://doi.org/10.1039/C6CS00176A>.
- (25) Edwards-Gayle, C. J. C.; Hamley, I. W. Self-Assembly of Bioactive Peptides, Peptide Conjugates, and Peptide Mimetic Materials. *Org. Biomol. Chem.* **2017**, *15* (28), 5867–5876. <https://doi.org/10.1039/C7OB01092C>.
- (26) Song, Z.; Chen, X.; You, X.; Huang, K.; Dhinakar, A.; Gu, Z.; Wu, J. Self-Assembly of Peptide Amphiphiles for Drug Delivery: The Role of Peptide Primary and Secondary Structures. *Biomater. Sci.* **2017**, *5* (12), 2369–2380. <https://doi.org/10.1039/C7BM00730B>.
- (27) Yu, C.-Y.; Huang, W.; Li, Z.-P.; Lei, X.-Y.; He, D.-X.; Sun, L. Progress in Self-Assembling Peptide-Based Nanomaterials for Biomedical Applications. *Curr. Top. Med. Chem.* **2016**, *16* (3), 281–290. <https://doi.org/10.2174/1568026615666150701114527>.
- (28) Ulijn, R. V.; Smith, A. M. Designing Peptide Based Nanomaterials. *Chem. Soc. Rev.* **2008**, *37* (4), 664–675. <https://doi.org/10.1039/B609047H>.
- (29) Burkhart, B. M.; Gassman, R. M.; Langs, D. A.; Pangborn, W. A.; Duax, W. L. Heterodimer Formation and Crystal Nucleation of Gramicidin D. *Biophys. J.* **1998**, *75* (5), 2135–2146. [https://doi.org/10.1016/S0006-3495\(98\)77656-8](https://doi.org/10.1016/S0006-3495(98)77656-8).
- (30) Akaïke, N. Chapter 8 - Gramicidin Perforated Patch. In *Physiology and Pathology of Chloride Transporters and Channels in the Nervous System*; Alvarez-Leefmans, F. J., Delpire, E., Eds.; Academic Press: San Diego, 2010; pp 141–147. <https://doi.org/10.1016/B978-0-12-374373-2.00008-X>.
- (31) Mori, T.; Okamoto, Y. Folding Simulations of Gramicidin A into the β -Helix Conformations: Simulated Annealing Molecular Dynamics Study. *J. Chem. Phys.* **2009**, *131* (16), 165103. <https://doi.org/10.1063/1.3247578>.

- (32) Marshall, G. R.; Beusen, D. D.; Nikiforovich, G. V. 5 - Peptide Conformation: Stability and Dynamics. In *Peptides*; Gutte, B., Ed.; Academic Press: San Diego, 1995; pp 193–245. <https://doi.org/10.1016/B978-012310920-0/50006-1>.
- (33) Schuster, T. B.; Ouboter, D. de B.; Bruns, N.; Meier, W. Exploiting Dimerization of Purely Peptidic Amphiphiles to Form Vesicles. *Small* **2011**, *7* (15), 2158–2162. <https://doi.org/10.1002/smll.201100701>.
- (34) Schuster, T. B.; Ouboter, D. de B.; Palivan, C. G.; Meier, W. From Fibers to Micelles Using Point-Mutated Amphiphilic Peptides. *Langmuir ACS J. Surf. Colloids* **2011**, *27* (8), 4578–4584. <https://doi.org/10.1021/la200443p>.
- (35) Schuster, T. B.; Ouboter, D. de B.; Bordignon, E.; Jeschke, G.; Meier, W. Reversible Peptide Particle Formation Using a Mini Amino Acid Sequence. *Soft Matter* **2010**, *6* (21), 5596–5604. <https://doi.org/10.1039/C0SM00442A>.
- (36) de Bruyn Ouboter, D.; Schuster, T. B.; Manton, A.; Meier, W. Hierarchical Organization of Purely Peptidic Amphiphiles into Peptide Beads. *J. Phys. Chem. C* **2011**, *115* (30), 14583–14590.
- (37) Sigg, S. J.; Postupalenko, V.; Duskey, J. T.; Palivan, C. G.; Meier, W. Stimuli-Responsive Codelivery of Oligonucleotides and Drugs by Self-Assembled Peptide Nanoparticles. *Biomacromolecules* **2016**, *17* (3), 935–945. <https://doi.org/10.1021/acs.biomac.5b01614>.
- (38) Bruyn Ouboter, D. de. Rational Design of Purely Peptidic Amphiphiles for Drug Delivery Applications. Thesis, University_of_Basel, 2011. <https://doi.org/10.5451/unibas-005657419>.
- (39) Katyal, P.; Meleties, M.; Montclare, J. K. Self-Assembled Protein- and Peptide-Based Nanomaterials. *ACS Biomater. Sci. Eng.* **2019**, *5* (9), 4132–4147. <https://doi.org/10.1021/acsbiomaterials.9b00408>.
- (40) Habibi, N.; Kamaly, N.; Memic, A.; Shafiee, H. Self-Assembled Peptide-Based Nanostructures: Smart Nanomaterials toward Targeted Drug Delivery. *Nano Today* **2016**, *11* (1), 41–60. <https://doi.org/10.1016/j.nantod.2016.02.004>.
- (41) Wang, H.; Feng, Z.; Xu, B. Supramolecular Assemblies of Peptides or Nucleopeptides for Gene Delivery. *Theranostics* **2019**, *9* (11), 3213–3222. <https://doi.org/10.7150/thno.31854>.
- (42) Fan, T.; Yu, X.; Shen, B.; Sun, L. Peptide Self-Assembled Nanostructures for Drug Delivery Applications <https://www.hindawi.com/journals/jnm/2017/4562474/> (accessed 2021 -01 -13). <https://doi.org/10.1155/2017/4562474>.
- (43) Imai, S.; Hirai, Y.; Nagao, C.; Sawamoto, M.; Terashima, T. Programmed Self-Assembly Systems of Amphiphilic Random Copolymers into Size-Controlled and Thermoresponsive Micelles in Water. *Macromolecules* **2018**, *51* (2), 398–409. <https://doi.org/10.1021/acs.macromol.7b01918>.
- (44) Fetsch, C.; Gaitzsch, J.; Messenger, L.; Battaglia, G.; Luxenhofer, R. Self-Assembly of Amphiphilic Block Copolypeptoids – Micelles, Worms and Polymersomes. *Sci. Rep.* **2016**, *6* (1), 33491. <https://doi.org/10.1038/srep33491>.
- (45) Lefley, J.; Waldron, C.; Remzi Becer, C. Macromolecular Design and Preparation of Polymersomes. *Polym. Chem.* **2020**, *11* (45), 7124–7136. <https://doi.org/10.1039/D0PY01247E>.
- (46) Weitzhandler, I.; Dzuricky, M.; Hoffmann, I.; Quiroz, F. G.; Gradzielski, M.; Chilkoti, A. Micellar Self-Assembly of Perfectly Sequence-Defined Recombinant Resilin-like/Elastin-like Block Copolypeptides. *Biomacromolecules* **2017**, *18* (8), 2419–2426. <https://doi.org/10.1021/acs.biomac.7b00589>.

- (47) Torchilin, V. P. Micellar Nanocarriers: Pharmaceutical Perspectives. *Pharm. Res.* **2007**, *24* (1), 1–16. <https://doi.org/10.1007/s11095-006-9132-0>.
- (48) Tu, R. S.; Tirrell, M. Bottom-up Design of Biomimetic Assemblies. *Adv. Drug Deliv. Rev.* **2004**, *56* (11), 1537–1563. <https://doi.org/10.1016/j.addr.2003.10.047>.
- (49) Bai, S.; Ma, X.; Zhang, T.; Gao, Y.-E.; Wang, Y.; Gao, Y.; Xu, Z. 12 - Polymeric Micelles as Delivery Systems. In *Nanoengineered Biomaterials for Advanced Drug Delivery*; Mozafari, M., Ed.; Woodhead Publishing Series in Biomaterials; Elsevier, 2020; pp 261–278. <https://doi.org/10.1016/B978-0-08-102985-5.00012-7>.
- (50) Song, Z.; Chen, X.; You, X.; Huang, K.; Dhinakar, A.; Gu, Z.; Wu, J. Self-Assembly of Peptide Amphiphiles for Drug Delivery: The Role of Peptide Primary and Secondary Structures. *Biomater. Sci.* **2017**, *5* (12), 2369–2380. <https://doi.org/10.1039/C7BM00730B>.
- (51) Kita-Tokarczyk, K.; Grumelard, J.; Haefele, T.; Meier, W. Block Copolymer Vesicles—Using Concepts from Polymer Chemistry to Mimic Biomembranes. *Polymer* **2005**, *46* (11), 3540–3563. <https://doi.org/10.1016/j.polymer.2005.02.083>.
- (52) Jiang, L.; Vader, P.; Schifferers, R. M. Extracellular Vesicles for Nucleic Acid Delivery: Progress and Prospects for Safe RNA-Based Gene Therapy. *Gene Ther.* **2017**, *24* (3), 157–166. <https://doi.org/10.1038/gt.2017.8>.
- (53) Habibi, N.; Kamaly, N.; Memic, A.; Shafiee, H. Self-Assembled Peptide-Based Nanostructures: Smart Nanomaterials toward Targeted Drug Delivery. *Nano Today* **2016**, *11* (1), 41–60. <https://doi.org/10.1016/j.nantod.2016.02.004>.
- (54) Deming, T. J. Preparation and Development of Block Copolypeptide Vesicles and Hydrogels for Biological and Medical Applications. *WIREs Nanomedicine Nanobiotechnology* **2014**, *6* (3), 283–297. <https://doi.org/10.1002/wnan.1262>.
- (55) van Hell, A. J.; Costa, C. I. C. A.; Flesch, F. M.; Sutter, M.; Jiskoot, W.; Crommelin, D. J. A.; Hennink, W. E.; Mastrobattista, E. Self-Assembly of Recombinant Amphiphilic Oligopeptides into Vesicles. *Biomacromolecules* **2007**, *8* (9), 2753–2761. <https://doi.org/10.1021/bm0704267>.
- (56) Bellomo, E. G.; Wyrsta, M. D.; Pakstis, L.; Pochan, D. J.; Deming, T. J. Stimuli-Responsive Polypeptide Vesicles by Conformation-Specific Assembly. *Nat. Mater.* **2004**, *3* (4), 244–248. <https://doi.org/10.1038/nmat1093>.
- (57) Holowka, E. P.; Pochan, D. J.; Deming, T. J. Charged Polypeptide Vesicles with Controllable Diameter. *J. Am. Chem. Soc.* **2005**, *127* (35), 12423–12428. <https://doi.org/10.1021/ja053557t>.
- (58) Santoso, S.; Hwang, W.; Hartman, H.; Zhang, S. Self-Assembly of Surfactant-like Peptides with Variable Glycine Tails to Form Nanotubes and Nanovesicles. *Nano Lett.* **2002**, *2* (7), 687–691. <https://doi.org/10.1021/nl025563i>.
- (59) Gudlur, S.; Sukthankar, P.; Gao, J.; Avila, L. A.; Hiromasa, Y.; Chen, J.; Iwamoto, T.; Tomich, J. M. Peptide Nanovesicles Formed by the Self-Assembly of Branched Amphiphilic Peptides. *PLoS ONE* **2012**, *7* (9). <https://doi.org/10.1371/journal.pone.0045374>.
- (60) Sunna, A.; Care, A.; Bergquist, P. L. *Peptides and Peptide-Based Biomaterials and Their Biomedical Applications*; Springer, 2017.
- (61) Cui, H.; Webber, M. J.; Stupp, S. I. Self-Assembly of Peptide Amphiphiles: From Molecules to Nanostructures to Biomaterials. *Pept. Sci.* **2010**, *94* (1), 1–18. <https://doi.org/10.1002/bip.21328>.

- (62) Wang, H.; Feng, Z.; Xu, B. Supramolecular Assemblies of Peptides or Nucleopeptides for Gene Delivery. *Theranostics* **2019**, *9* (11), 3213–3222. <https://doi.org/10.7150/thno.31854>.
- (63) Fan, T.; Yu, X.; Shen, B.; Sun, L. Peptide Self-Assembled Nanostructures for Drug Delivery Applications. *J. Nanomater.* **2017**, *2017*, 1–16. <https://doi.org/10.1155/2017/4562474>.
- (64) Zhang, S.; Marini, D. M.; Hwang, W.; Santoso, S. Design of Nanostructured Biological Materials through Self-Assembly of Peptides and Proteins. *Curr. Opin. Chem. Biol.* **2002**, *6* (6), 865–871. [https://doi.org/10.1016/S1367-5931\(02\)00391-5](https://doi.org/10.1016/S1367-5931(02)00391-5).
- (65) Yadav, S.; Sharma, A. K.; Kumar, P. Nanoscale Self-Assembly for Therapeutic Delivery. *Front. Bioeng. Biotechnol.* **2020**, *8*. <https://doi.org/10.3389/fbioe.2020.00127>.
- (66) Han, S.; Cao, S.; Wang, Y.; Wang, J.; Xia, D.; Xu, H.; Zhao, X.; Lu, J. R. Self-Assembly of Short Peptide Amphiphiles: The Cooperative Effect of Hydrophobic Interaction and Hydrogen Bonding. *Chem. – Eur. J.* **2011**, *17* (46), 13095–13102. <https://doi.org/10.1002/chem.201101970>.
- (67) Zhang, H.; Park, J.; Jiang, Y.; Woodrow, K. A. Rational Design of Charged Peptides That Self-Assemble into Robust Nanofibers as Immune-Functional Scaffolds. *Acta Biomater.* **2017**, *55*, 183–193. <https://doi.org/10.1016/j.actbio.2017.03.041>.
- (68) Hartgerink, J. D.; Beniash, E.; Stupp, S. I. Peptide-Amphiphile Nanofibers: A Versatile Scaffold for the Preparation of Self-Assembling Materials. *Proc. Natl. Acad. Sci.* **2002**, *99* (8), 5133–5138. <https://doi.org/10.1073/pnas.0726999999>.
- (69) Dehsorkhi, A.; Castelletto, V.; Hamley, I. W. Self-Assembling Amphiphilic Peptides. *J. Pept. Sci.* **2014**, *20* (7), 453–467. <https://doi.org/10.1002/psc.2633>.
- (70) Seroski, D. T.; Hudalla, G. A. Chapter 19 - Self-Assembled Peptide and Protein Nanofibers for Biomedical Applications. In *Biomedical Applications of Functionalized Nanomaterials*; Sarmiento, B., das Neves, J., Eds.; Micro and Nano Technologies; Elsevier, 2018; pp 569–598. <https://doi.org/10.1016/B978-0-323-50878-0.00019-7>.
- (71) Valéry, C.; Artzner, F.; Paternostre, M. Peptide Nanotubes: Molecular Organisations, Self-Assembly Mechanisms and Applications. *Soft Matter* **2011**, *7* (20), 9583–9594. <https://doi.org/10.1039/C1SM05698K>.
- (72) Horne, W. S.; Stout, C. D.; Ghadiri, M. R. A Heterocyclic Peptide Nanotube. *J. Am. Chem. Soc.* **2003**, *125* (31), 9372–9376. <https://doi.org/10.1021/ja034358h>.
- (73) Gao, X.; Matsui, H. Peptide-Based Nanotubes and Their Applications in Bionanotechnology. *Adv. Mater. Deerfield Beach Fla* **2005**, *17* (17), 2037–2050. <https://doi.org/10.1002/adma.200401849>.
- (74) Yuan, C.; Ji, W.; Xing, R.; Li, J.; Gazit, E.; Yan, X. Hierarchically Oriented Organization in Supramolecular Peptide Crystals. *Nat. Rev. Chem.* **2019**, *3* (10), 567–588. <https://doi.org/10.1038/s41570-019-0129-8>.
- (75) Fuhrhop, J.-H.; Koning, J. *Membranes and Molecular Assemblies: The Synkinetic Approach*; Royal Society of Chemistry, 2007.
- (76) Mandal, D.; Shirazi, A. N.; Parang, K. Self-Assembly of Peptides to Nanostructures. *Org. Biomol. Chem.* **2014**, *12* (22), 3544–3561. <https://doi.org/10.1039/C4OB00447G>.
- (77) Lee, D.; Rejinold, N. S.; Jeong, S. D.; Kim, Y.-C. Stimuli-Responsive Polypeptides for Biomedical Applications. *Polymers* **2018**, *10* (8). <https://doi.org/10.3390/polym10080830>.
- (78) Shah, A.; Malik, M. S.; Khan, G. S.; Nosheen, E.; Ifikhar, F. J.; Khan, F. A.; Shukla, S. S.; Akhter, M. S.; Kraatz, H.-B.; Aminabhavi, T. M. Stimuli-Responsive Peptide-Based Biomaterials as Drug Delivery Systems. *Chem. Eng. J.* **2018**, *353*, 559–583. <https://doi.org/10.1016/j.cej.2018.07.126>.

- (79) Löwik, D. W. P. M.; Leunissen, E. H. P.; Heuvel, M. van den; Hansen, M. B.; Hest, J. C. M. van. Stimulus Responsive Peptide Based Materials. *Chem. Soc. Rev.* **2010**, *39* (9), 3394–3412. <https://doi.org/10.1039/B914342B>.
- (80) Mura, S.; Nicolas, J.; Couvreur, P. Stimuli-Responsive Nanocarriers for Drug Delivery. *Nat. Mater.* **2013**, *12* (11), 991–1003. <https://doi.org/10.1038/nmat3776>.
- (81) Liu, D.; Sun, J. Thermoresponsive Polypeptoids. *Polymers* **2020**, *12* (12), 2973. <https://doi.org/10.3390/polym12122973>.
- (82) Jeong, W.; Kwon, S. hyun; Lim, Y. Modular Self-Assembling Peptide Platform with a Tunable Thermoresponsiveness via a Single Amino Acid Substitution. *Adv. Funct. Mater.* **2018**, *28* (35), 1803114. <https://doi.org/10.1002/adfm.201803114>.
- (83) Chockalingam, K.; Blenner, M.; Banta, S. Design and Application of Stimulus-Responsive Peptide Systems. *Protein Eng. Des. Sel.* **2007**, *20* (4), 155–161. <https://doi.org/10.1093/protein/gzm008>.
- (84) Ward, M. A.; Georgiou, T. K. Thermoresponsive Polymers for Biomedical Applications. *Polymers* **2011**, *3* (3), 1215–1242. <https://doi.org/10.3390/polym3031215>.
- (85) Dunshee, L. C.; Sullivan, M. O.; Kiick, K. L. Manipulation of the Dually Thermoresponsive Behavior of Peptide-Based Vesicles through Modification of Collagen-like Peptide Domains. *Bioeng. Transl. Med.* **2020**, *5* (1), e10145. <https://doi.org/10.1002/btm2.10145>.
- (86) Mulligan, R. C. The Basic Science of Gene Therapy. *Science* **1993**, *260* (5110), 926–932. <https://doi.org/10.1126/science.8493530>.
- (87) Jayant, R. D.; Sosa, D.; Kaushik, A.; Atluri, V.; Vashist, A.; Tomitaka, A.; Nair, M. Current Status of Non-Viral Gene Therapy for CNS Disorders. *Expert Opin. Drug Deliv.* **2016**, *13* (10), 1433–1445. <https://doi.org/10.1080/17425247.2016.1188802>.
- (88) Maeder, M. L.; Gersbach, C. A. Genome-Editing Technologies for Gene and Cell Therapy. *Mol. Ther.* **2016**, *24* (3), 430–446. <https://doi.org/10.1038/mt.2016.10>.
- (89) Seymour, L. W.; Thrasher, A. J. Gene Therapy Matures in the Clinic. *Nat. Biotechnol.* **2012**, *30* (7), 588–593. <https://doi.org/10.1038/nbt.2290>.
- (90) Foldvari, M.; Chen, D. W.; Nafissi, N.; Calderon, D.; Narsineni, L.; Rafiee, A. Non-Viral Gene Therapy: Gains and Challenges of Non-Invasive Administration Methods. *J. Controlled Release* **2016**, *240*, 165–190. <https://doi.org/10.1016/j.jconrel.2015.12.012>.
- (91) Slivac, I.; Guay, D.; Mangion, M.; Champeil, J.; Gaillet, B. Non-Viral Nucleic Acid Delivery Methods. *Expert Opin. Biol. Ther.* **2017**, *17* (1), 105–118. <https://doi.org/10.1080/14712598.2017.1248941>.
- (92) Liang, X.; Liu, L.; Wei, Y.-Q.; Gao, G.-P.; Wei, X.-W. Clinical Evaluations of Toxicity and Efficacy of Nanoparticle-Mediated Gene Therapy. *Hum. Gene Ther.* **2018**, *29* (11), 1227–1234. <https://doi.org/10.1089/hum.2018.069>.
- (93) Naldini, L. Gene Therapy Returns to Centre Stage. *Nature* **2015**, *526* (7573), 351–360. <https://doi.org/10.1038/nature15818>.
- (94) Martin, M. E.; Rice, K. G. Peptide-Guided Gene Delivery. *AAPS J.* **2007**, *9* (1), E18–E29. <https://doi.org/10.1208/aapsj0901003>.
- (95) Yin, H.; Kanasty, R. L.; Eltoukhy, A. A.; Vegas, A. J.; Dorkin, J. R.; Anderson, D. G. Non-Viral Vectors for Gene-Based Therapy. *Nat. Rev. Genet.* **2014**, *15* (8), 541–555. <https://doi.org/10.1038/nrg3763>.
- (96) Hagel, L.; Jagschies, G.; Sofer, G. 9 - Basic Properties of Peptides, Proteins, Nucleic Acids and Virus Particles. In *Handbook of Process Chromatography (Second Edition)*; Hagel, L.,

- Jagschies, G., Sofer, G., Eds.; Academic Press: Amsterdam, 2008; pp 219–235. <https://doi.org/10.1016/B978-012374023-6.50011-7>.
- (97) Chuah, J.-A.; Matsugami, A.; Hayashi, F.; Numata, K. Self-Assembled Peptide-Based System for Mitochondrial-Targeted Gene Delivery: Functional and Structural Insights. *Biomacromolecules* **2016**, *17* (11), 3547–3557. <https://doi.org/10.1021/acs.biomac.6b01056>.
- (98) Yan, X.; He, Q.; Wang, K.; Duan, L.; Cui, Y.; Li, J. Transition of Cationic Dipeptide Nanotubes into Vesicles and Oligonucleotide Delivery. *Angew. Chem. Int. Ed.* **2007**, *46* (14), 2431–2434. <https://doi.org/10.1002/anie.200603387>.
- (99) Avila, L. A.; Aps, L. R. M. M.; Ploscariu, N.; Sukthankar, P.; Guo, R.; Wilkinson, K. E.; Games, P.; Szoszkiewicz, R.; Alves, R. P. S.; Diniz, M. O.; Fang, Y.; Ferreira, L. C. S.; Tomich, J. M. Gene Delivery and Immunomodulatory Effects of Plasmid DNA Associated with Branched Amphiphilic Peptide Capsules. *J. Controlled Release* **2016**, *241*, 15–24. <https://doi.org/10.1016/j.jconrel.2016.08.042>.
- (100) Mann, A.; Richa, R.; Ganguli, M. DNA Condensation by Poly-L-Lysine at the Single Molecule Level: Role of DNA Concentration and Polymer Length. *J. Controlled Release* **2008**, *125* (3), 252–262. <https://doi.org/10.1016/j.jconrel.2007.10.019>.
- (101) Ferrer-Miralles, N.; Vázquez, E.; Villaverde, A. Membrane-Active Peptides for Non-Viral Gene Therapy: Making the Safest Easier. *Trends Biotechnol.* **2008**, *26* (5), 267–275. <https://doi.org/10.1016/j.tibtech.2008.02.003>.
- (102) Durymanov, M.; Reineke, J. Non-Viral Delivery of Nucleic Acids: Insight Into Mechanisms of Overcoming Intracellular Barriers. *Front. Pharmacol.* **2018**, *9*. <https://doi.org/10.3389/fphar.2018.00971>.
- (103) Lin, G.; Li, L.; Panwar, N.; Wang, J.; Tjin, S. C.; Wang, X.; Yong, K.-T. Non-Viral Gene Therapy Using Multifunctional Nanoparticles: Status, Challenges, and Opportunities. *Coord. Chem. Rev.* **2018**, *374*, 133–152. <https://doi.org/10.1016/j.ccr.2018.07.001>.
- (104) Ahmed, M. Peptides, Polypeptides and Peptide-Polymer Hybrids as Nucleic Acid Carriers. *Biomater. Sci.* **2017**, *5* (11), 2188–2211. <https://doi.org/10.1039/c7bm00584a>.
- (105) Marelli, U. K.; Rechenmacher, F.; Sobahi, T. R. A.; Mas-Moruno, C.; Kessler, H. Tumor Targeting via Integrin Ligands. *Front. Oncol.* **2013**, *3*. <https://doi.org/10.3389/fonc.2013.00222>.
- (106) Koren, E.; Torchilin, V. P. Cell-Penetrating Peptides: Breaking through to the Other Side. *Trends Mol. Med.* **2012**, *18* (7), 385–393. <https://doi.org/10.1016/j.molmed.2012.04.012>.
- (107) Pan, L.; He, Q.; Liu, J.; Chen, Y.; Ma, M.; Zhang, L.; Shi, J. Nuclear-Targeted Drug Delivery of TAT Peptide-Conjugated Monodisperse Mesoporous Silica Nanoparticles. *J. Am. Chem. Soc.* **2012**, *134* (13), 5722–5725. <https://doi.org/10.1021/ja211035w>.
- (108) Sudo, K.; Niikura, K.; Iwaki, K.; Kohyama, S.; Fujiwara, K.; Doi, N. Human-Derived Fusogenic Peptides for the Intracellular Delivery of Proteins. *J. Controlled Release* **2017**, *255*, 1–11. <https://doi.org/10.1016/j.jconrel.2017.03.398>.
- (109) Azevedo, C.; Macedo, M. H.; Sarmiento, B. Strategies for the Enhanced Intracellular Delivery of Nanomaterials. *Drug Discov. Today* **2018**, *23* (5), 944–959. <https://doi.org/10.1016/j.drudis.2017.08.011>.
- (110) Ruoslahti, E. Specialization of Tumour Vasculature. *Nat. Rev. Cancer* **2002**, *2* (2), 83–90. <https://doi.org/10.1038/nrc724>.
- (111) Brown, K. C. Peptidic Tumor Targeting Agents: The Road from Phage Display Peptide Selections to Clinical Applications. *Curr. Pharm. Des.* **2010**, *16* (9), 1040–1054.

- (112) Zhao, N.; Qin, Y.; Liu, H.; Cheng, Z. Tumor-Targeting Peptides: Ligands for Molecular Imaging and Therapy. *Anticancer Agents Med. Chem.* **2018**, *18* (1), 74–86. <https://doi.org/10.2174/1871520617666170419143459>.
- (113) Jeong, W.; Bu, J.; Kubiawicz, L. J.; Chen, S. S.; Kim, Y.; Hong, S. Peptide–Nanoparticle Conjugates: A next Generation of Diagnostic and Therapeutic Platforms? *Nano Converg.* **2018**, *5* (1), 38. <https://doi.org/10.1186/s40580-018-0170-1>.
- (114) Torchilin, V. P. Cell Penetrating Peptide-Modified Pharmaceutical Nanocarriers for Intracellular Drug and Gene Delivery. *Pept. Sci.* **2008**, *90* (5), 604–610. <https://doi.org/10.1002/bip.20989>.
- (115) Wang, F.; Wang, Y.; Zhang, X.; Zhang, W.; Guo, S.; Jin, F. Recent Progress of Cell-Penetrating Peptides as New Carriers for Intracellular Cargo Delivery. *J. Controlled Release* **2014**, *174*, 126–136. <https://doi.org/10.1016/j.jconrel.2013.11.020>.
- (116) Munyendo, W. L.; Lv, H.; Benza-Ingoula, H.; Baraza, L. D.; Zhou, J. Cell Penetrating Peptides in the Delivery of Biopharmaceuticals. *Biomolecules* **2012**, *2* (2), 187–202. <https://doi.org/10.3390/biom2020187>.
- (117) Kang, Z.; Meng, Q.; Liu, K. Peptide-Based Gene Delivery Vectors. *J. Mater. Chem. B* **2019**, *7* (11), 1824–1841. <https://doi.org/10.1039/C8TB03124J>.
- (118) Tripathi, P. P.; Arami, H.; Banga, I.; Gupta, J.; Gandhi, S. Cell Penetrating Peptides in Preclinical and Clinical Cancer Diagnosis and Therapy. *Oncotarget* **2018**, *9* (98), 37252–37267. <https://doi.org/10.18632/oncotarget.26442>.
- (119) Kersemans, V.; Kersemans, K.; Cornelissen, B. Cell Penetrating Peptides for in Vivo Molecular Imaging Applications. *Curr. Pharm. Des.* **2008**. <https://doi.org/10.2174/138161208785777432>.
- (120) Alhakamy, N. A.; Nigatu, A. S.; Berkland, C. J.; Ramsey, J. D. Noncovalently Associated - Penetrating Peptides for Gene Delivery Applications. *Ther. Deliv.* **2013**, *4* (6), 741–757. <https://doi.org/10.4155/tde.13.44>.
- (121) Thapa, R. K.; Sullivan, M. O. Gene Delivery by Peptide-Assisted Transport. *Curr. Opin. Biomed. Eng.* **2018**, *7*, 71–82. <https://doi.org/10.1016/j.cobme.2018.10.002>.
- (122) Lindgren, M.; Langel, Ü. Classes and Prediction of Cell-Penetrating Peptides. In *Cell-Penetrating Peptides: Methods and Protocols*; Langel, Ü., Ed.; Methods in Molecular Biology; Humana Press: Totowa, NJ, 2011; pp 3–19. https://doi.org/10.1007/978-1-60761-919-2_1.
- (123) Madani, F.; Lindberg, S.; Langel, Ü.; Futaki, S.; Gräslund, A. Mechanisms of Cellular Uptake of Cell-Penetrating Peptides. *J. Biophys.* **2011**, *2011*, 1–10. <https://doi.org/10.1155/2011/414729>.
- (124) Durymanov, M.; Reineke, J. Non-Viral Delivery of Nucleic Acids: Insight Into Mechanisms of Overcoming Intracellular Barriers. *Front. Pharmacol.* **2018**, *9*. <https://doi.org/10.3389/fphar.2018.00971>.
- (125) Uludag, H.; Ubeda, A.; Ansari, A. At the Intersection of Biomaterials and Gene Therapy: Progress in Non-Viral Delivery of Nucleic Acids. *Front. Bioeng. Biotechnol.* **2019**, *7*. <https://doi.org/10.3389/fbioe.2019.00131>.
- (126) Vermeulen, L. M. P.; Brans, T.; De Smedt, S. C.; Remaut, K.; Braeckmans, K. Methodologies to Investigate Intracellular Barriers for Nucleic Acid Delivery in Non-Viral Gene Therapy. *Nano Today* **2018**, *21*, 74–90. <https://doi.org/10.1016/j.nantod.2018.06.007>.
- (127) Shi, B.; Zheng, M.; Tao, W.; Chung, R.; Jin, D.; Ghaffari, D.; Farokhzad, O. C. Challenges in DNA Delivery and Recent Advances in Multifunctional Polymeric DNA Delivery

- Systems. *Biomacromolecules* **2017**, *18* (8), 2231–2246. <https://doi.org/10.1021/acs.biomac.7b00803>.
- (128) Yao, J.; Fan, Y.; Li, Y.; Huang, L. Strategies on the Nuclear-Targeted Delivery of Genes. *J. Drug Target.* **2013**, *21* (10), 926–939. <https://doi.org/10.3109/1061186X.2013.830310>.
- (129) Kosugi, S.; Hasebe, M.; Matsumura, N.; Takashima, H.; Miyamoto-Sato, E.; Tomita, M.; Yanagawa, H. Six Classes of Nuclear Localization Signals Specific to Different Binding Grooves of Importin α . *J. Biol. Chem.* **2009**, *284* (1), 478–485. <https://doi.org/10.1074/jbc.M807017200>.
- (130) Lange, A.; Mills, R. E.; Lange, C. J.; Stewart, M.; Devine, S. E.; Corbett, A. H. Classical Nuclear Localization Signals: Definition, Function, and Interaction with Importin α . *J. Biol. Chem.* **2007**, *282* (8), 5101–5105. <https://doi.org/10.1074/jbc.R600026200>.
- (131) van der Aa, M. A. E. M.; Mastrobattista, E.; Oosting, R. S.; Hennink, W. E.; Koning, G. A.; Crommelin, D. J. A. The Nuclear Pore Complex: The Gateway to Successful Nonviral Gene Delivery. *Pharm. Res.* **2006**, *23* (3), 447–459. <https://doi.org/10.1007/s11095-005-9445-4>.
- (132) Cartier, R.; Reszka, R. Utilization of Synthetic Peptides Containing Nuclear Localization Signals for Nonviral Gene Transfer Systems. *Gene Ther.* **2002**, *9* (3), 157–167. <https://doi.org/10.1038/sj.gt.3301635>.
- (133) Loughran, S. P.; McCrudden, C. M.; McCarthy, H. O. Designer Peptide Delivery Systems for Gene Therapy. *Eur. J. Nanomedicine* **2015**, *7* (2), 85–96. <https://doi.org/10.1515/ejnm-2014-0037>.
- (134) Pelley, J. W. 3 - Protein Structure and Function. In *Elsevier's Integrated Biochemistry*; Pelley, J. W., Ed.; Mosby: Philadelphia, 2007; pp 19–28. <https://doi.org/10.1016/B978-0-323-03410-4.50009-2>.
- (135) Merrifield, R. B. **Solid Phase Peptide Synthesis. I. The Synthesis of a Tetrapeptide.** *J. Am. Chem. Soc.* **1963**, *85* (14), 2149–2154. <https://doi.org/10.1021/ja00897a025>.
- (136) Verlander, M. Industrial Applications of Solid-Phase Peptide Synthesis – A Status Report. *Int. J. Pept. Res. Ther.* **2007**, *13* (1), 75–82. <https://doi.org/10.1007/s10989-006-9075-7>.
- (137) Kimmerlin, T.; Seebach, D. ‘100 Years of Peptide Synthesis’: Ligation Methods for Peptide and Protein Synthesis with Applications to β -Peptide Assemblies*: 100 Years of Peptide Synthesis. *J. Pept. Res.* **2008**, *65* (2), 229–260. <https://doi.org/10.1111/j.1399-3011.2005.00214.x>.
- (138) Palomo, J. M. Solid-Phase Peptide Synthesis: An Overview Focused on the Preparation of Biologically Relevant Peptides. *RSC Adv.* **2014**, *4* (62), 32658–32672. <https://doi.org/10.1039/C4RA02458C>.
- (139) Stawikowski, M.; Fields, G. B. Introduction to Peptide Synthesis. *Curr. Protoc. Protein Sci. Editor. Board John E Coligan Al* **2002**, *CHAPTER*, Unit-18.1. <https://doi.org/10.1002/0471140864.ps1801s26>.
- (140) Behrendt, R.; White, P.; Offer, J. Advances in Fmoc Solid-phase Peptide Synthesis. *J. Pept. Sci.* **2016**, *22* (1), 4–27. <https://doi.org/10.1002/psc.2836>.
- (141) Tarvirdipour, S.; Schoenenberger, C.-A.; Benenson, Y.; G. Palivan, C. A Self-Assembling Amphiphilic Peptide Nanoparticle for the Efficient Entrapment of DNA Cargoes up to 100 Nucleotides in Length. *Soft Matter* **2020**, *16* (6), 1678–1691. <https://doi.org/10.1039/C9SM01990A>.
- (142) Tomich, J. M.; Wessel, E.; Choi, J.; Avila, L. A. Chapter 8 - Nonviral Gene Therapy: Peptiplexes. In *Nucleic Acid Nanotheranostics*; Filice, M., Ruiz-Cabello, J., Eds.; Micro and

- Nano Technologies; Elsevier, 2019; pp 247–276. <https://doi.org/10.1016/B978-0-12-814470-1.00008-3>.
- (143) Halperin-Sternfeld, M.; Ghosh, M.; Adler-Abramovich, L. Advantages of Self-Assembled Supramolecular Polymers Toward Biological Applications. In *Supramolecular Chemistry of Biomimetic Systems*; Li, J., Ed.; Springer: Singapore, 2017; pp 9–35. https://doi.org/10.1007/978-981-10-6059-5_2.
- (144) Wong, L.-Y.; Xia, B.; Wolvetang, E.; Cooper-White, J. Targeted, Stimuli-Responsive Delivery of Plasmid DNA and MiRNAs Using a Facile Self-Assembled Supramolecular Nanoparticle System. *Biomacromolecules* **2018**, *19* (2), 353–363. <https://doi.org/10.1021/acs.biomac.7b01462>.
- (145) Gabrielson, N. P.; Cheng, J. Multiplexed Supramolecular Self-Assembly for Non-Viral Gene Delivery. *Biomaterials* **2010**, *31* (34), 9117–9127. <https://doi.org/10.1016/j.biomaterials.2010.08.024>.
- (146) Busseron, E.; Ruff, Y.; Moulin, E.; Giuseppone, N. Supramolecular Self-Assemblies as Functional Nanomaterials. *Nanoscale* **2013**, *5* (16), 7098–7140. <https://doi.org/10.1039/C3NR02176A>.
- (147) Guler, M. O.; Hsu, L.; Soukasene, S.; Harrington, D. A.; Hulvat, J. F.; Stupp, S. I. Presentation of RGDS Epitopes on Self-Assembled Nanofibers of Branched Peptide Amphiphiles. *Biomacromolecules* **2006**, *7* (6), 1855–1863. <https://doi.org/10.1021/bm060161g>.
- (148) He, Z.-Y.; Deng, F.; Wei, X.-W.; Ma, C.-C.; Luo, M.; Zhang, P.; Sang, Y.-X.; Liang, X.; Liu, L.; Qin, H.-X.; Shen, Y.-L.; Liu, T.; Liu, Y.-T.; Wang, W.; Wen, Y.-J.; Zhao, X.; Zhang, X.-N.; Qian, Z.-Y.; Wei, Y.-Q. Ovarian Cancer Treatment with a Tumor-Targeting and Gene Expression-Controllable Lipoplex. *Sci. Rep.* **2016**, *6* (1), 23764. <https://doi.org/10.1038/srep23764>.
- (149) Boulikas, T. Encapsulation of Plasmid DNA (Lipogenes™) and Therapeutic Agents with Nuclear Localization Signal/Fusogenic Peptide Conjugates into Targeted Liposome Complexes. US9278067B2, March 8, 2016.
- (150) Dinari, A.; Moghadam, T. T.; Abdollahi, M.; Sadeghizadeh, M. Synthesis and Characterization of a Nano-Polyplex System of GNRs-PDMAEA-PDNA: An Inert Self-Catalyzed Degradable Carrier for Facile Gene Delivery. *Sci. Rep.* **2018**, *8* (1), 8112. <https://doi.org/10.1038/s41598-018-26260-4>.
- (151) Kim, H. A.; Nam, K.; Kim, S. W. Tumor Targeting RGD Conjugated Bio-Reducible Polymer for VEGF SiRNA Expressing Plasmid Delivery. *Biomaterials* **2014**, *35* (26), 7543–7552. <https://doi.org/10.1016/j.biomaterials.2014.05.021>.
- (152) McCarthy, H. O.; McCaffrey, J.; McCrudden, C. M.; Zholobenko, A.; Ali, A. A.; McBride, J. W.; Massey, A. S.; Pentlavalli, S.; Chen, K.-H.; Cole, G.; Loughran, S. P.; Dunne, N. J.; Donnelly, R. F.; Kett, V. L.; Robson, T. Development and Characterization of Self-Assembling Nanoparticles Using a Bio-Inspired Amphipathic Peptide for Gene Delivery. *J. Controlled Release* **2014**, *189*, 141–149. <https://doi.org/10.1016/j.jconrel.2014.06.048>.
- (153) Massey, A. S.; Pentlavalli, S.; Cunningham, R.; McCrudden, C. M.; McErlean, E. M.; Redpath, P.; Ali, A. A.; Annett, S.; McBride, J. W.; McCaffrey, J.; Robson, T.; Migaud, M. E.; McCarthy, H. O. Potentiating the Anticancer Properties of Bisphosphonates by Nanocomplexation with the Cationic Amphipathic Peptide, RALA. *Mol. Pharm.* **2016**, *13* (4), 1217–1228. <https://doi.org/10.1021/acs.molpharmaceut.5b00670>.

- (154) Hendricks, M. P.; Sato, K.; Palmer, L. C.; Stupp, S. I. Supramolecular Assembly of Peptide Amphiphiles. *Acc. Chem. Res.* **2017**, *50* (10), 2440–2448. <https://doi.org/10.1021/acs.accounts.7b00297>.
- (155) Mohammadinejad, R.; Dehshahri, A.; Sagar Madamsetty, V.; Zahmatkeshan, M.; Tavakol, S.; Makvandi, P.; Khorsandi, D.; Pardakhty, A.; Ashrafizadeh, M.; Ghasemipour Afshar, E.; Zarrabi, A. In Vivo Gene Delivery Mediated by Non-Viral Vectors for Cancer Therapy. *J. Controlled Release* **2020**, *325*, 249–275. <https://doi.org/10.1016/j.jconrel.2020.06.038>.
- (156) Buck, J.; Grossen, P.; Cullis, P. R.; Huwyler, J.; Witzigmann, D. Lipid-Based DNA Therapeutics: Hallmarks of Non-Viral Gene Delivery. *ACS Nano* **2019**, *13* (4), 3754–3782. <https://doi.org/10.1021/acsnano.8b07858>.
- (157) Patil, S.; Gao, Y.-G.; Lin, X.; Li, Y.; Dang, K.; Tian, Y.; Zhang, W.-J.; Jiang, S.-F.; Qadir, A.; Qian, A.-R. The Development of Functional Non-Viral Vectors for Gene Delivery. *Int. J. Mol. Sci.* **2019**, *20* (21), 5491. <https://doi.org/10.3390/ijms20215491>.
- (158) Lambert, G.; Fattal, E.; Couvreur, P. Nanoparticulate Systems for the Delivery of Antisense Oligonucleotides. *Adv. Drug Deliv. Rev.* **2001**, *47* (1), 99–112. [https://doi.org/10.1016/S0169-409X\(00\)00116-2](https://doi.org/10.1016/S0169-409X(00)00116-2).
- (159) Scoles, D. R.; Pulst, S. M. Oligonucleotide Therapeutics in Neurodegenerative Diseases. *RNA Biol.* **2018**, *15* (6), 707–714. <https://doi.org/10.1080/15476286.2018.1454812>.
- (160) Di Fusco, D.; Dinallo, V.; Marafini, I.; Figliuzzi, M. M.; Romano, B.; Monteleone, G. Antisense Oligonucleotide: Basic Concepts and Therapeutic Application in Inflammatory Bowel Disease. *Front. Pharmacol.* **2019**, *10*. <https://doi.org/10.3389/fphar.2019.00305>.
- (161) Rossor, A. M.; Reilly, M. M.; Sleight, J. N. Antisense Oligonucleotides and Other Genetic Therapies Made Simple. *Pract. Neurol.* **2018**, *18* (2), 126–131. <https://doi.org/10.1136/practneurol-2017-001764>.
- (162) Frazier, K. S. Antisense Oligonucleotide Therapies: The Promise and the Challenges from a Toxicologic Pathologist’s Perspective. *Toxicol. Pathol.* **2015**, *43* (1), 78–89. <https://doi.org/10.1177/0192623314551840>.
- (163) El-Sayed, N. S.; Miyake, T.; Shirazi, A. N.; Park, S. E.; Clark, J.; Buchholz, S.; Parang, K.; Tiwari, R. Design, Synthesis, and Evaluation of Homochiral Peptides Containing Arginine and Histidine as Molecular Transporters. *Mol. J. Synth. Chem. Nat. Prod. Chem.* **2018**, *23* (7). <https://doi.org/10.3390/molecules23071590>.
- (164) van Rossenberg, S.; van Keulen, A.; Drijfhout, J.-W.; Vasto, S.; Koerten, H. K.; Spies, F.; van ’t Noordende, J.; van Berkel, T.; Biessen, E. a. L. Stable Polyplexes Based on Arginine-Containing Oligopeptides for in Vivo Gene Delivery. *Gene Ther.* **2004**, *11* (5), 457–464. <https://doi.org/10.1038/sj.gt.3302183>.
- (165) Harada, A.; Kataoka, K. Supramolecular Assemblies of Block Copolymers in Aqueous Media as Nanocontainers Relevant to Biological Applications. *Prog. Polym. Sci.* **2006**, *31* (11), 949–982. <https://doi.org/10.1016/j.progpolymsci.2006.09.004>.
- (166) Gunkel-Grabole, G.; Sigg, S.; Lomora, M.; Lörcher, S.; Palivan, C. G.; Meier, W. P. Polymeric 3D Nano-Architectures for Transport and Delivery of Therapeutically Relevant Biomacromolecules. *Biomater. Sci.* **2015**, *3* (1), 25–40. <https://doi.org/10.1039/C4BM00230J>.
- (167) Euliss, L. E.; DuPont, J. A.; Gratton, S.; DeSimone, J. Imparting Size, Shape, and Composition Control of Materials for Nanomedicine. *Chem. Soc. Rev.* **2006**, *35* (11), 1095–1104. <https://doi.org/10.1039/B600913C>.

- (168) Win, K. Y.; Feng, S.-S. Effects of Particle Size and Surface Coating on Cellular Uptake of Polymeric Nanoparticles for Oral Delivery of Anticancer Drugs. *Biomaterials* **2005**, *26* (15), 2713–2722. <https://doi.org/10.1016/j.biomaterials.2004.07.050>.
- (169) McAllister, K.; Sazani, P.; Adam, M.; Cho, M. J.; Rubinstein, M.; Samulski, R. J.; DeSimone, J. M. Polymeric Nanogels Produced via Inverse Microemulsion Polymerization as Potential Gene and Antisense Delivery Agents. *J. Am. Chem. Soc.* **2002**, *124* (51), 15198–15207. <https://doi.org/10.1021/ja027759q>.
- (170) Rejman, J.; Oberle, V.; Zuhorn, I. S.; Hoekstra, D. Size-Dependent Internalization of Particles via the Pathways of Clathrin-and Caveolae-Mediated Endocytosis. *Biochem. J.* **2004**, *377* (1), 159–169. <https://doi.org/10.1042/BJ20031253>.
- (171) Prabu, P.; Chaudhari, A. A.; Dharmaraj, N.; Khil, M. S.; Park, S. Y.; Kim, H. Y. Preparation, Characterization, In-vitro Drug Release and Cellular Uptake of Poly (Caprolactone) Grafted Dextran Copolymeric Nanoparticles Loaded with Anticancer Drug. *J. Biomed. Mater. Res. Part Off. J. Soc. Biomater. Jpn. Soc. Biomater. Aust. Soc. Biomater. Korean Soc. Biomater.* **2009**, *90* (4), 1128–1136. <https://doi.org/10.1002/jbm.a.32163>.
- (172) Nkodo, A. E.; Garnier, J. M.; Tinland, B.; Ren, H.; Desruisseaux, C.; McCormick, L. C.; Drouin, G.; Slater, G. W. Diffusion Coefficient of DNA Molecules during Free Solution Electrophoresis. *Electrophoresis* **2001**, *22* (12), 2424–2432. [https://doi.org/10.1002/1522-2683\(200107\)22:12<2424::AID-ELPS2424>3.0.CO;2-1](https://doi.org/10.1002/1522-2683(200107)22:12<2424::AID-ELPS2424>3.0.CO;2-1).
- (173) Danaei, M.; Dehghankhold, M.; Ataei, S.; Hasanzadeh Davarani, F.; Javanmard, R.; Dokhani, A.; Khorasani, S.; Mozafari, M. Impact of Particle Size and Polydispersity Index on the Clinical Applications of Lipidic Nanocarrier Systems. *Pharmaceutics* **2018**, *10* (2), 57. <https://doi.org/10.3390/pharmaceutics10020057>.
- (174) Mohsen, A. M.; Asfour, M. H.; Salama, A. A. A. Improved Hepatoprotective Activity of Silymarin via Encapsulation in the Novel Vesicular Nanosystem Bilosomes. *Drug Dev. Ind. Pharm.* **2017**, *43* (12), 2043–2054. <https://doi.org/10.1080/03639045.2017.1361968>.
- (175) Koynov, K.; Butt, H.-J. Fluorescence Correlation Spectroscopy in Colloid and Interface Science. *Curr. Opin. Colloid Interface Sci.* **2012**, *17* (6), 377–387. <https://doi.org/10.1016/j.cocis.2012.09.003>.
- (176) Bishop, N. E. An Update on Non-clathrin-coated Endocytosis. *Rev. Med. Virol.* **1997**, *7* (4), 199–209. [https://doi.org/10.1002/\(sici\)1099-1654\(199712\)7:4<199::aid-rmv203>3.0.co;2-f](https://doi.org/10.1002/(sici)1099-1654(199712)7:4<199::aid-rmv203>3.0.co;2-f).
- (177) Oupický, D.; Carlisle, R. C.; Seymour, L. W. Triggered Intracellular Activation of Disulfide Crosslinked Polyelectrolyte Gene Delivery Complexes with Extended Systemic Circulation in Vivo. *Gene Ther.* **2001**, *8* (9), 713. <https://doi.org/10.1038/sj.gt.3301446>.
- (178) Verma, A.; Stellacci, F. Effect of Surface Properties on Nanoparticle–Cell Interactions. *Small* **2010**, *6* (1), 12–21. <https://doi.org/10.1002/sml.200901158>.
- (179) Convertine, A. J.; Benoit, D. S.; Duvall, C. L.; Hoffman, A. S.; Stayton, P. S. Development of a Novel Endosomolytic Diblock Copolymer for siRNA Delivery. *J. Controlled Release* **2009**, *133* (3), 221–229. <https://doi.org/10.1016/j.jconrel.2008.10.004>.
- (180) Thomas, M.; Klibanov, A. M. Non-Viral Gene Therapy: Polycation-Mediated DNA Delivery. *Appl. Microbiol. Biotechnol.* **2003**, *62* (1), 27–34. <https://doi.org/10.1007/s00253-003-1321-8>.
- (181) Ogris, M.; Brunner, S.; Schüller, S.; Kircheis, R.; Wagner, E. PEGylated DNA/Transferrin–PEI Complexes: Reduced Interaction with Blood Components, Extended Circulation in

- Blood and Potential for Systemic Gene Delivery. *Gene Ther.* **1999**, *6* (4), 595. <https://doi.org/10.1038/sj.gt.3300900>.
- (182) Akinc, A.; Lynn, D. M.; Anderson, D. G.; Langer, R. Parallel Synthesis and Biophysical Characterization of a Degradable Polymer Library for Gene Delivery. *J. Am. Chem. Soc.* **2003**, *125* (18), 5316–5323. <https://doi.org/10.1021/ja034429c>.
- (183) Lee, H.; Lytton-Jean, A. K.; Chen, Y.; Love, K. T.; Park, A. I.; Karagiannis, E. D.; Sehgal, A.; Querbes, W.; Zurenko, C. S.; Jayaraman, M. Molecularly Self-Assembled Nucleic Acid Nanoparticles for Targeted in Vivo SiRNA Delivery. *Nat. Nanotechnol.* **2012**, *7* (6), 389. <https://doi.org/10.1038/NNANO.2012.73>.
- (184) Gaumet, M.; Vargas, A.; Gurny, R.; Delie, F. Nanoparticles for Drug Delivery: The Need for Precision in Reporting Particle Size Parameters. *Eur. J. Pharm. Biopharm.* **2008**, *69* (1), 1–9. <https://doi.org/10.1016/j.ejpb.2007.08.001>.
- (185) Huang, L.; Wagner, E. Non-Viral Vectors for Gene Therapy. San Diego: Academic Press, A Division of Harcourt 1999.
- (186) Yamano, S.; Dai, J.; Hanatani, S.; Haku, K.; Yamanaka, T.; Ishioka, M.; Takayama, T.; Yuvienco, C.; Khapli, S.; Moursi, A. M. Long-Term Efficient Gene Delivery Using Polyethylenimine with Modified Tat Peptide. *Biomaterials* **2014**, *35* (5), 1705–1715. <https://doi.org/10.1016/j.biomaterials.2013.11.012>.
- (187) Kircheis, R.; Wightman, L.; Wagner, E. Design and Gene Delivery Activity of Modified Polyethylenimines. *Adv. Drug Deliv. Rev.* **2001**, *53* (3), 341–358. [https://doi.org/10.1016/S0169-409X\(01\)00202-2](https://doi.org/10.1016/S0169-409X(01)00202-2).
- (188) Zhao, F.; Zhao, Y.; Liu, Y.; Chang, X.; Chen, C.; Zhao, Y. Cellular Uptake, Intracellular Trafficking, and Cytotoxicity of Nanomaterials. *Small* **2011**, *7* (10), 1322–1337. <https://doi.org/10.1002/sml.201100001>.
- (189) Rothbard, J. B.; Kreider, E.; VanDeusen, C. L.; Wright, L.; Wylie, B. L.; Wender, P. A. Arginine-Rich Molecular Transporters for Drug Delivery: Role of Backbone Spacing in Cellular Uptake. *J. Med. Chem.* **2002**, *45* (17), 3612–3618. <https://doi.org/10.1021/jm0105676>.
- (190) Tung, C.-H.; Weissleder, R. Arginine Containing Peptides as Delivery Vectors. *Adv. Drug Deliv. Rev.* **2003**, *55* (2), 281–294. [https://doi.org/10.1016/S0169-409X\(02\)00183-7](https://doi.org/10.1016/S0169-409X(02)00183-7).
- (191) El-Sayed, A.; Futaki, S.; Harashima, H. Delivery of Macromolecules Using Arginine-Rich Cell-Penetrating Peptides: Ways to Overcome Endosomal Entrapment. *AAPS J.* **2009**, *11* (1), 13–22. <https://doi.org/10.1208/s12248-008-9071-2>.
- (192) Gao, Y.; Xu, Z.; Chen, S.; Gu, W.; Chen, L.; Li, Y. Arginine-Chitosan/DNA Self-Assemble Nanoparticles for Gene Delivery: In Vitro Characteristics and Transfection Efficiency. *Int. J. Pharm.* **2008**, *359* (1–2), 241–246. <https://doi.org/10.1016/j.ijpharm.2008.03.037>.
- (193) Liu, X.; Liu, C.; Zhou, J.; Chen, C.; Qu, F.; Rossi, J. J.; Rocchi, P.; Peng, L. Promoting SiRNA Delivery via Enhanced Cellular Uptake Using an Arginine-Decorated Amphiphilic Dendrimer. *Nanoscale* **2015**, *7* (9), 3867–3875. <https://doi.org/10.1039/c4nr04759a>.
- (194) Bagnacani, V.; Franceschi, V.; Bassi, M.; Lomazzi, M.; Donofrio, G.; Sansone, F.; Casnati, A.; Ungaro, R. Arginine Clustering on Calix [4] Arene Macrocycles for Improved Cell Penetration and DNA Delivery. *Nat. Commun.* **2013**, *4*, 1721. <https://doi.org/10.1038/ncomms2721>.
- (195) Qin, H.; Jiang, Y.; Zhang, J.; Deng, C.; Zhong, Z. Oncoprotein Inhibitor Rigosertib Loaded in ApoE-Targeted Smart Polymersomes Reveals High Safety and Potency against Human

- Glioblastoma in Mice. *Mol. Pharm.* **2019**, *16* (8), 3711–3719. <https://doi.org/10.1021/acs.molpharmaceut.9b00691>.
- (196) Silva, E. R.; Cooney, G.; Hamley, I. W.; Alves, W. A.; Lee, S.; O'Connor, B. F.; Reza, M.; Ruokolainen, J.; Walls, D. Structural Behaviour and Gene Delivery in Complexes Formed between DNA and Arginine-Containing Peptide Amphiphiles. *Soft Matter* **2016**, *12* (45), 9158–9169. <https://doi.org/10.1039/C6SM01618A>.
- (197) El-Sayed, A.; Khalil, I. A.; Kogure, K.; Futaki, S.; Harashima, H. Octaarginine-and Octalysine-Modified Nanoparticles Have Different Modes of Endosomal Escape. *J. Biol. Chem.* **2008**, *283* (34), 23450–23461. <https://doi.org/10.1074/jbc.M709387200>.
- (198) Parodi, A.; Corbo, C.; Cevenini, A.; Molinaro, R.; Palomba, R.; Pandolfi, L.; Agostini, M.; Salvatore, F.; Tasciotti, E. Enabling Cytoplasmic Delivery and Organelle Targeting by Surface Modification of Nanocarriers. *Nanomed.* **2015**, *10* (12), 1923–1940. <https://doi.org/10.2217/nnm.15.39>.
- (199) Wagstaff, K. M.; Jans, D. A. Nucleocytoplasmic Transport of DNA: Enhancing Non-Viral Gene Transfer. *Biochem. J.* **2007**, *406* (2), 185–202. <https://doi.org/10.1042/BJ20070505>.
- (200) Dean, D.; Strong, D.; Zimmer, W. Nuclear Entry of Nonviral Vectors. *Gene Ther.* **2005**, *12* (11), 881–890. <https://doi.org/10.1038/sj.gt.3302534>.
- (201) Jones, C. H.; Chen, C.-K.; Ravikrishnan, A.; Rane, S.; Pfeifer, B. A. Overcoming Nonviral Gene Delivery Barriers: Perspective and Future. *Mol. Pharm.* **2013**, *10* (11), 4082–4098. <https://doi.org/10.1021/mp400467x>.
- (202) Rad-Malekshahi, M.; Lempsink, L.; Amidi, M.; Hennink, W. E.; Mastrobattista, E. Biomedical Applications of Self-Assembling Peptides. *Bioconjug. Chem.* **2016**, *27* (1), 3–18. <https://doi.org/10.1021/acs.bioconjchem.5b00487>.
- (203) Chen, J.; Zou, X. Self-Assemble Peptide Biomaterials and Their Biomedical Applications. *Bioact. Mater.* **2019**, *4*, 120–131. <https://doi.org/10.1016/j.bioactmat.2019.01.002>.
- (204) Mudhakir, D.; Harashima, H. Learning from the Viral Journey: How to Enter Cells and How to Overcome Intracellular Barriers to Reach the Nucleus. *AAPS J.* **2009**, *11* (1). <https://doi.org/10.1208/s12248-009-9080-9>.
- (205) Sun, Y.; Xian, L.; Xing, H.; Yu, J.; Yang, Z.; Yang, T.; Yang, L.; Ding, P. Factors Influencing the Nuclear Targeting Ability of Nuclear Localization Signals. *J. Drug Target.* **2016**, *24* (10), 927–933. <https://doi.org/10.1080/1061186X.2016.1184273>.
- (206) Anna, A.; Monika, G. Splicing Mutations in Human Genetic Disorders: Examples, Detection, and Confirmation. *J. Appl. Genet.* **2018**, *59* (3), 253–268. <https://doi.org/10.1007/s13353-018-0444-7>.
- (207) Geyer, P. K.; Vitalini, M. W.; Wallrath, L. L. Nuclear Organization: Taking a Position on Gene Expression. *Curr. Opin. Cell Biol.* **2011**, *23* (3), 354–359. <https://doi.org/10.1016/j.ceb.2011.03.002>.
- (208) Zwerger, M.; Ho, C. Y.; Lammerding, J. Nuclear Mechanics in Disease. *Annu. Rev. Biomed. Eng.* **2011**, *13*, 397–428. <https://doi.org/10.1146/annurev-bioeng-071910-124736>.
- (209) Lam, A. P.; Dean, D. A. Progress and Prospects: Nuclear Import of Nonviral Vectors. *Gene Ther.* **2010**, *17* (4), 439–447. <https://doi.org/10.1038/gt.2010.31>.
- (210) Lai, W.-F.; Wong, W.-T. Design of Polymeric Gene Carriers for Effective Intracellular Delivery. *Trends Biotechnol.* **2018**, *36* (7), 713–728. <https://doi.org/10.1016/j.tibtech.2018.02.006>.

- (211) Hill, A. B.; Chen, M.; Chen, C.-K.; Pfeifer, B. A.; Jones, C. H. Overcoming Gene-Delivery Hurdles: Physiological Considerations for Nonviral Vectors. *Trends Biotechnol.* **2016**, *34* (2), 91–105. <https://doi.org/10.1016/j.tibtech.2015.11.004>.
- (212) Thapa, R. K.; Sullivan, M. O. Gene Delivery by Peptide-Assisted Transport. *Curr. Opin. Biomed. Eng.* **2018**, *7*, 71–82. <https://doi.org/10.1016/j.cobme.2018.10.002>.
- (213) Thapa, B.; Narain, R. 1 - Mechanism, Current Challenges and New Approaches for Non Viral Gene Delivery. In *Polymers and Nanomaterials for Gene Therapy*; Narain, R., Ed.; Woodhead Publishing, 2016; pp 1–27. <https://doi.org/10.1016/B978-0-08-100520-0.00001-1>.
- (214) Xu, D.; Farmer, A.; Chook, Y. M. Recognition of Nuclear Targeting Signals by Karyopherin- β Proteins. *Curr. Opin. Struct. Biol.* **2010**, *20* (6), 782–790. <https://doi.org/10.1016/j.sbi.2010.09.008>.
- (215) Sakiyama, Y.; Mazur, A.; Kapinos, L. E.; Lim, R. Y. H. Spatiotemporal Dynamics of the Nuclear Pore Complex Transport Barrier Resolved by High-Speed Atomic Force Microscopy. *Nat. Nanotechnol.* **2016**, *11* (8), 719–723. <https://doi.org/10.1038/nnano.2016.62>.
- (216) Conti, E.; Kuriyan, J. Crystallographic Analysis of the Specific yet Versatile Recognition of Distinct Nuclear Localization Signals by Karyopherin α . *Structure* **2000**, *8* (3), 329–338. [https://doi.org/10.1016/S0969-2126\(00\)00107-6](https://doi.org/10.1016/S0969-2126(00)00107-6).
- (217) Marfori, M.; Mynott, A.; Ellis, J. J.; Mehdi, A. M.; Saunders, N. F. W.; Curmi, P. M.; Forwood, J. K.; Bodén, M.; Kobe, B. Molecular Basis for Specificity of Nuclear Import and Prediction of Nuclear Localization. *Biochim. Biophys. Acta BBA - Mol. Cell Res.* **2011**, *1813* (9), 1562–1577. <https://doi.org/10.1016/j.bbamcr.2010.10.013>.
- (218) Tarvirdipour, S.; Huang, X.; Mihali, V.; Schoenenberger, C.-A.; Palivan, C. G. Peptide-Based Nanoassemblies in Gene Therapy and Diagnosis: Paving the Way for Clinical Application. *Molecules* **2020**, *25* (15), 3482. <https://doi.org/10.3390/molecules25153482>.
- (219) Gigante, A.; Li, M.; Junghänel, S.; Hirschhäuser, C.; Knauer, S.; Schmuck, C. Non-Viral Transfection Vectors: Are Hybrid Materials the Way Forward? *MedChemComm* **2019**, *10* (10), 1692–1718. <https://doi.org/10.1039/C9MD00275H>.
- (220) Do, H.-J.; Song, H.; Yang, H.-M.; Kim, D.-K.; Kim, N.-H.; Kim, J.-H.; Cha, K.-Y.; Chung, H.-M.; Kim, J.-H. Identification of Multiple Nuclear Localization Signals in Murine Elf3, an ETS Transcription Factor. *FEBS Lett.* **2006**, *580* (7), 1865–1871. <https://doi.org/10.1016/j.febslet.2006.02.049>.
- (221) Beg, A. A.; Ruben, S. M.; Scheinman, R. I.; Haskill, S.; Rosen, C. A.; Baldwin, A. S. I Kappa B Interacts with the Nuclear Localization Sequences of the Subunits of NF-Kappa B: A Mechanism for Cytoplasmic Retention. *Genes Dev.* **1992**, *6* (10), 1899–1913. <https://doi.org/10.1101/gad.6.10.1899>.
- (222) Lokareddy, R. K.; Hapsari, R. A.; van Rheenen, M.; Pumroy, R. A.; Bhardwaj, A.; Steen, A.; Veenhoff, L. M.; Cingolani, G. Distinctive Properties of the Nuclear Localization Signals of Inner Nuclear Membrane Proteins Heh1 and Heh2. *Structure* **2015**, *23* (7), 1305–1316. <https://doi.org/10.1016/j.str.2015.04.017>.
- (223) O'Day, D. H. Proteins of the Nucleolus of Dictyostelium Discoideum: Nucleolar Compartmentalization, Targeting Sequences, Protein Translocations and Binding Partners. *Cells* **2019**, *8* (2), 167. <https://doi.org/10.3390/cells8020167>.

- (224) Li, X.; Zhu, F. Identification of the Nuclear Export and Adjacent Nuclear Localization Signals for ORF45 of Kaposi's Sarcoma-Associated Herpesvirus. *J. Virol.* **2009**, *83* (6), 2531–2539. <https://doi.org/10.1128/JVI.02209-08>.
- (225) Catalano, A.; O'Day, D. H. Nucleoplasmic/Nucleolar Translocation and Identification of a Nuclear Localization Signal (NLS) in Dictyostelium BAF60a/SMARCD1 Homologue Snf12. *Histochem. Cell Biol.* **2012**, *138* (3), 515–530. <https://doi.org/10.1007/s00418-012-0973-9>.
- (226) Brendel, J. C.; Catrouillet, S.; Sanchis, J.; Jolliffe, K. A.; Perrier, S. Shaping Block Copolymer Micelles by Supramolecular Polymerization: Making 'Tubisomes.' *Polym. Chem.* **2019**, *10* (20), 2616–2625. <https://doi.org/10.1039/C9PY00179D>.
- (227) Tarvirdipour, S.; Schoenenberger, C.-A.; Benenson, Y.; Palivan, C. G. A Self-Assembling Amphiphilic Peptide Nanoparticle for the Efficient Entrapment of DNA Cargoes up to 100 Nucleotides in Length. *Soft Matter* **2020**, *16* (6), 1678–1691. <https://doi.org/10.1039/C9SM01990A>.
- (228) Honary, S.; Zahir, F. Effect of Zeta Potential on the Properties of Nano-Drug Delivery Systems - A Review (Part 2). *Trop. J. Pharm. Res.* **2013**, *12* (2), 265–273. <https://doi.org/10.4314/tjpr.v12i2.20>.
- (229) Aramburu, I. V.; Lemke, E. A. Floppy but Not Sloppy: Interaction Mechanism of FG-Nucleoporins and Nuclear Transport Receptors. *Semin. Cell Dev. Biol.* **2017**, *68*, 34–41. <https://doi.org/10.1016/j.semdb.2017.06.026>.
- (230) Hülsmann, B. B.; Labokha, A. A.; Görlich, D. The Permeability of Reconstituted Nuclear Pores Provides Direct Evidence for the Selective Phase Model. *Cell* **2012**, *150* (4), 738–751. <https://doi.org/10.1016/j.cell.2012.07.019>.
- (231) Zelmer, C.; Zweifel, L. P.; Kapinos, L. E.; Craciun, I.; Güven, Z. P.; Palivan, C. G.; Lim, R. Y. H. Organelle-Specific Targeting of Polymersomes into the Cell Nucleus. *Proc. Natl. Acad. Sci.* **2020**, *117* (6), 2770–2778. <https://doi.org/10.1073/pnas.1916395117>.
- (232) Chook, Y.; Blobel, G. Karyopherins and Nuclear Import. *Curr. Opin. Struct. Biol.* **2001**, *11* (6), 703–715. [https://doi.org/10.1016/S0959-440X\(01\)00264-0](https://doi.org/10.1016/S0959-440X(01)00264-0).
- (233) Paci, G.; Zheng, T.; Caria, J.; Zilman, A.; Lemke, E. A. Molecular Determinants of Large Cargo Transport into the Nucleus. *eLife* **9**. <https://doi.org/10.7554/eLife.55963>.
- (234) Davis, L. K.; Šarić, A.; Hoogenboom, B. W.; Zilman, A. Physical Modelling of Multivalent Interactions in the Nuclear Pore Complex. *bioRxiv* **2020**, 2020.10.01.322156. <https://doi.org/10.1101/2020.10.01.322156>.
- (235) Bourgeois, B.; Hutten, S.; Gottschalk, B.; Hofweber, M.; Richter, G.; Sternat, J.; Abou-Ajram, C.; Göbl, C.; Leitinger, G.; Graier, W. F.; Dormann, D.; Madl, T. Nonclassical Nuclear Localization Signals Mediate Nuclear Import of CIRBP. *Proc. Natl. Acad. Sci.* **2020**, *117* (15), 8503–8514. <https://doi.org/10.1073/pnas.1918944117>.
- (236) Fagerlund, R.; Melén, K.; Kinnunen, L.; Julkunen, I. Arginine/Lysine-Rich Nuclear Localization Signals Mediate Interactions between Dimeric STATs and Importin A5. *J. Biol. Chem.* **2002**, *277* (33), 30072–30078. <https://doi.org/10.1074/jbc.M202943200>.
- (237) Auría-Soro, C.; Nesma, T.; Juanes-Velasco, P.; Landeira-Viñuela, A.; Fidalgo-Gomez, H.; Acebes-Fernandez, V.; Gongora, R.; Almendral Parra, M. J.; Manzano-Roman, R.; Fuentes, M. Interactions of Nanoparticles and Biosystems: Microenvironment of Nanoparticles and Biomolecules in Nanomedicine. *Nanomaterials* **2019**, *9* (10). <https://doi.org/10.3390/nano9101365>.

- (238) Huang, C.; Chen, X.; Xue, Z.; Wang, T. Effect of Structure: A New Insight into Nanoparticle Assemblies from Inanimate to Animate. *Sci. Adv.* **2020**, *6* (20), eaba1321. <https://doi.org/10.1126/sciadv.aba1321>.
- (239) Anderson, E. M.; Miller, P.; Ilsley, D.; Marshall, W.; Khvorova, A.; Stein, C. A.; Benimetskaya, L. Gene Profiling Study of G3139- and Bcl-2-Targeting SiRNAs Identifies a Unique G3139 Molecular Signature. *Cancer Gene Ther.* **2006**, *13* (4), 406–414. <https://doi.org/10.1038/sj.cgt.7700901>.
- (240) Marshall, J.; Chen, H.; Yang, D.; Figueira, M.; Bouker, K. B.; Ling, Y.; Lippman, M.; Frankel, S. R.; Hayes, D. F. A Phase I Trial of a Bcl-2 Antisense (G3139) and Weekly Docetaxel in Patients with Advanced Breast Cancer and Other Solid Tumors. *Ann. Oncol.* **2004**, *15* (8), 1274–1283. <https://doi.org/10.1093/annonc/mdh317>.
- (241) Xu, H.; Liao, C.; Liang, S.; Ye, B.-C. A Novel Peptide-Equipped Exosomes Platform for Delivery of Antisense Oligonucleotides. *ACS Appl. Mater. Interfaces* **2021**, *13* (9), 10760–10767. <https://doi.org/10.1021/acsami.1c00016>.
- (242) Bulut, S.; Erkal, T. S.; Toksoz, S.; Tekinay, A. B.; Tekinay, T.; Guler, M. O. Slow Release and Delivery of Antisense Oligonucleotide Drug by Self-Assembled Peptide Amphiphile Nanofibers. *Biomacromolecules* **2011**, *12* (8), 3007–3014. <https://doi.org/10.1021/bm200641e>.
- (243) Zhou, Y.; Han, S.; Liang, Z.; Zhao, M.; Liu, G.; Wu, J. Progress in Arginine-Based Gene Delivery Systems. *J. Mater. Chem. B* **2020**, *8* (26), 5564–5577. <https://doi.org/10.1039/D0TB00498G>.
- (244) Gessner, I.; Neundorf, I. Nanoparticles Modified with Cell-Penetrating Peptides: Conjugation Mechanisms, Physicochemical Properties, and Application in Cancer Diagnosis and Therapy. *Int. J. Mol. Sci.* **2020**, *21* (7). <https://doi.org/10.3390/ijms21072536>.
- (245) Silva, S.; Almeida, A. J.; Vale, N. Combination of Cell-Penetrating Peptides with Nanoparticles for Therapeutic Application: A Review. *Biomolecules* **2019**, *9* (1). <https://doi.org/10.3390/biom9010022>.
- (246) Foroozandeh, P.; Aziz, A. A. Insight into Cellular Uptake and Intracellular Trafficking of Nanoparticles. *Nanoscale Res. Lett.* **2018**, *13* (1), 339. <https://doi.org/10.1186/s11671-018-2728-6>.
- (247) Sharad, S. *Antisense Therapy: An Overview*; IntechOpen, 2019. <https://doi.org/10.5772/intechopen.86867>.
- (248) Doxakis, E. Therapeutic Antisense Oligonucleotides for Movement Disorders. *Med. Res. Rev.* *n/a* (n/a). <https://doi.org/10.1002/med.21706>.
- (249) Walder, R. Y.; Walder, J. A. Role of RNase H in Hybrid-Arrested Translation by Antisense Oligonucleotides. *Proc. Natl. Acad. Sci.* **1988**, *85* (14), 5011–5015. <https://doi.org/10.1073/pnas.85.14.5011>.
- (250) Liang, X.-H.; Sun, H.; Nichols, J. G.; Croke, S. T. RNase H1-Dependent Antisense Oligonucleotides Are Robustly Active in Directing RNA Cleavage in Both the Cytoplasm and the Nucleus. *Mol. Ther.* **2017**, *25* (9), 2075–2092. <https://doi.org/10.1016/j.ymthe.2017.06.002>.
- (251) Batista-Duharte, A.; Sendra, L.; Herrero, M. J.; Téllez-Martínez, D.; Carlos, I. Z.; Aliño, S. F. Progress in the Use of Antisense Oligonucleotides for Vaccine Improvement. *Biomolecules* **2020**, *10* (2), 316. <https://doi.org/10.3390/biom10020316>.

- (252) Cazenave, C.; Frank, P.; Toulme, J. J.; Büsen, W. Characterization and Subcellular Localization of Ribonuclease H Activities from *Xenopus Laevis* Oocytes. *J. Biol. Chem.* **1994**, *269* (40), 25185–25192.
- (253) Kher, G.; Trehan, S.; Misra, A. 7 - Antisense Oligonucleotides and RNA Interference. In *Challenges in Delivery of Therapeutic Genomics and Proteomics*; Misra, A., Ed.; Elsevier: London, 2011; pp 325–386. <https://doi.org/10.1016/B978-0-12-384964-9.00007-4>.
- (254) Badros, A. Z.; Goloubeva, O.; Rapoport, A. P.; Ratterree, B.; Gahres, N.; Meisenberg, B.; Takebe, N.; Heyman, M.; Zwiebel, J.; Streicher, H.; Gocke, C. D.; Tomic, D.; Flaws, J. A.; Zhang, B.; Fenton, R. G. Phase II Study of G3139, a Bcl-2 Antisense Oligonucleotide, in Combination With Dexamethasone and Thalidomide in Relapsed Multiple Myeloma Patients. *J. Clin. Oncol.* **2005**, *23* (18), 4089–4099. <https://doi.org/10.1200/JCO.2005.14.381>.
- (255) Morris, M. J.; Tong, W. P.; Cordon-Cardo, C.; Drobnjak, M.; Kelly, W. K.; Slovin, S. F.; Terry, K. L.; Siedlecki, K.; Swanson, P.; Rafi, M.; DiPaola, R. S.; Rosen, N.; Scher, H. I. Phase I Trial of BCL-2 Antisense Oligonucleotide (G3139) Administered by Continuous Intravenous Infusion in Patients with Advanced Cancer. *Clin. Cancer Res.* **2002**, *8* (3), 679–683.
- (256) Xiong, H.; Veedu, R. N.; Diermeier, S. D. Recent Advances in Oligonucleotide Therapeutics in Oncology. *Int. J. Mol. Sci.* **2021**, *22* (7), 3295. <https://doi.org/10.3390/ijms22073295>.
- (257) Crooke, S. T.; Wang, S.; Vickers, T. A.; Shen, W.; Liang, X. Cellular Uptake and Trafficking of Antisense Oligonucleotides. *Nat. Biotechnol.* **2017**, *35* (3), 230–237. <https://doi.org/10.1038/nbt.3779>.
- (258) Benimetskaya, L.; Guzzo-Pernell, N.; Liu, S.-T.; Lai, J. C. H.; Miller, P.; Stein, C. A. Protamine-Fragment Peptides Fused to an SV40 Nuclear Localization Signal Deliver Oligonucleotides That Produce Antisense Effects in Prostate and Bladder Carcinoma Cells. *Bioconjug. Chem.* **2002**, *13* (2), 177–187. <https://doi.org/10.1021/bc010068j>.
- (259) Dai, G.; Chan, K. K.; Liu, S.; Hoyt, D.; Whitman, S.; Klisovic, M.; Shen, T.; Caligiuri, M. A.; Byrd, J.; Grever, M.; Marcucci, G. Cellular Uptake and Intracellular Levels of the Bcl-2 Antisense G3139 in Cultured Cells and Treated Patients with Acute Myeloid Leukemia. *Clin. Cancer Res.* **2005**, *11* (8), 2998–3008. <https://doi.org/10.1158/1078-0432.CCR-04-1505>.
- (260) Järver, P.; Coursindel, T.; Andaloussi, S. E.; Godfrey, C.; Wood, M. J.; Gait, M. J. Peptide-Mediated Cell and In Vivo Delivery of Antisense Oligonucleotides and siRNA. *Mol. Ther. Nucleic Acids* **2012**, *1*, e27. <https://doi.org/10.1038/mtna.2012.18>.
- (261) Cheng, X.; Liu, Q.; Li, H.; Kang, C.; Liu, Y.; Guo, T.; Shang, K.; Yan, C.; Cheng, G.; Lee, R. J. Lipid Nanoparticles Loaded with an Antisense Oligonucleotide Gapmer Against Bcl-2 for Treatment of Lung Cancer. *Pharm. Res.* **2017**, *34* (2), 310–320. <https://doi.org/10.1007/s11095-016-2063-5>.
- (262) Bono, N.; Ponti, F.; Mantovani, D.; Candiani, G. Non-Viral in Vitro Gene Delivery: It Is Now Time to Set the Bar! *Pharmaceutics* **2020**, *12* (2), 183. <https://doi.org/10.3390/pharmaceutics12020183>.
- (263) Hoshyar, N.; Gray, S.; Han, H.; Bao, G. The Effect of Nanoparticle Size on in Vivo Pharmacokinetics and Cellular Interaction. *Nanomed.* **2016**, *11* (6), 673–692. <https://doi.org/10.2217/nnm.16.5>.

- (264) Fan, M.; Du, L.; Stone, A. A.; Gilbert, K. M.; Chambers, T. C. Modulation of Mitogen-Activated Protein Kinases and Phosphorylation of Bcl-2 by Vinblastine Represent Persistent Forms of Normal Fluctuations at G2-M. *Cancer Res.* **2000**, *60* (22), 6403–6407.
- (265) Scatena, C. D.; Stewart, Z. A.; Mays, D.; Tang, L. J.; Keefer, C. J.; Leach, S. D.; Pietenpol, J. A. Mitotic Phosphorylation of Bcl-2 during Normal Cell Cycle Progression and Taxol-Induced Growth Arrest *. *J. Biol. Chem.* **1998**, *273* (46), 30777–30784. <https://doi.org/10.1074/jbc.273.46.30777>.
- (266) Yamamoto, K.; Ichijo, H.; Korsmeyer, S. J. BCL-2 Is Phosphorylated and Inactivated by an ASK1/Jun N-Terminal Protein Kinase Pathway Normally Activated at G2/M. *Mol. Cell. Biol.* **1999**, *19* (12), 8469–8478. <https://doi.org/10.1128/MCB.19.12.8469>.
- (267) Kapinos, L. E.; Schoch, R. L.; Wagner, R. S.; Schleicher, K. D.; Lim, R. Y. H. Karyopherin-Centric Control of Nuclear Pores Based on Molecular Occupancy and Kinetic Analysis of Multivalent Binding with FG Nucleoporins. *Biophys. J.* **2014**, *106* (8), 1751–1762. <https://doi.org/10.1016/j.bpj.2014.02.021>.
- (268) Kapinos, L. E.; Huang, B.; Rencurel, C.; Lim, R. Y. H. Karyopherins Regulate Nuclear Pore Complex Barrier and Transport Function. *J. Cell Biol.* **2017**, *216* (11), 3609–3624. <https://doi.org/10.1083/jcb.201702092>.
- (269) Haustein, E.; Schwille, P. Fluorescence Correlation Spectroscopy: Novel Variations of an Established Technique. *Annu Rev Biophys Biomol Struct* **2007**, *36*, 151–169. <https://doi.org/10.1146/annurev.biophys.36.040306.132612>.
- (270) Pal, N.; Verma, S. D.; Singh, M. K.; Sen, S. Fluorescence Correlation Spectroscopy: An Efficient Tool for Measuring Size, Size-Distribution and Polydispersity of Microemulsion Droplets in Solution. *Anal. Chem.* **2011**, *83* (20), 7736–7744. <https://doi.org/10.1021/ac2012637>.
- (271) Schoch, R. L.; Kapinos, L. E.; Lim, R. Y. H. Nuclear Transport Receptor Binding Avidity Triggers a Self-Healing Collapse Transition in FG-Nucleoporin Molecular Brushes. *Proc. Natl. Acad. Sci.* **2012**, *109* (42), 16911–16916. <https://doi.org/10.1073/pnas.1208440109>.
- (272) Bernhard, W. A New Staining Procedure for Electron Microscopical Cytology. *J. Ultrastruct. Res.* **1969**, *27* (3), 250–265. [https://doi.org/10.1016/s0022-5320\(69\)80016-x](https://doi.org/10.1016/s0022-5320(69)80016-x).
- (273) Mullan, A. Imaris Reference Manual. 546.